

August 1, 1977

ANL/FPP/TM-91

IMPURITY CONTROL IN TOKAMAK REACTORS

W. M. Stacey, Jr., D. L. Smith, J. N. Brooks
P. J. Bertoncini and D. A. Ehst

*Fusion Power Program
Argonne National Laboratory
Argonne, Illinois 60439*

ANL/FPP Technical Memorandum No. 91

Results reported in the FPP series of memoranda frequently are preliminary and subject to revision. They should not be quoted nor referenced without the author's permission.

Work supported by the U. S. Energy Research and Development Administration.

The facilities of Argonne National Laboratory are owned by the United States Government. Under the terms of a contract (W-31-109-Eng-38) between the U. S. Energy Research and Development Administration, Argonne Universities Association and The University of Chicago, the University employs the staff and operates the Laboratory in accordance with policies and programs formulated, approved and reviewed by the Association.

MEMBERS OF ARGONNE UNIVERSITIES ASSOCIATION

The University of Arizona	Kansas State University	The Ohio State University
Carnegie-Mellon University	The University of Kansas	Ohio University
Case Western Reserve University	Loyola University	The Pennsylvania State University
The University of Chicago	Marquette University	Purdue University
University of Cincinnati	Michigan State University	Saint Louis University
Illinois Institute of Technology	The University of Michigan	Southern Illinois University
University of Illinois	University of Minnesota	The University of Texas at Austin
Indiana University	University of Missouri	Washington University
Iowa State University	Northwestern University	Wayne State University
The University of Iowa	University of Notre Dame	The University of Wisconsin

NOTICE

This report was prepared as an account of work sponsored by the United States Government. Neither the United States nor the United States Energy Research and Development Administration, nor any of their employees, nor any of their contractors, subcontractors, or their employees, makes any warranty, express or implied, or assumes any legal liability or responsibility for the accuracy, completeness or usefulness of any information, apparatus, product or process disclosed, or represents that its use would not infringe privately-owned rights. Mention of commercial products, their manufacturers, or their suppliers in this publication does not imply or connote approval or disapproval of the product by Argonne National Laboratory or the U. S. Energy Research and Development Administration.

August 1, 1977

ANL/FPP/TM-91

IMPURITY CONTROL IN TOKAMAK REACTORS

W. M. Stacey, Jr., D. L. Smith, J. N. Brooks
P. J. Bertoncini and D. A. Ehst

*Fusion Power Program
Argonne National Laboratory
Argonne, Illinois 60439*

ANL/FPP Technical Memorandum No. 91

Results reported in the FPP series of memoranda frequently are preliminary and subject to revision. They should not be quoted nor referenced without the author's permission.

Work supported by the U. S. Energy Research and Development Administration.

TABLE OF CONTENTS

	<u>Page</u>
ABSTRACT	1
INTRODUCTION	2
I. PLASMA-WALL-DIVERTOR INTERACTION MODEL	4
A. Deuterium-Tritium	4
B. Alpha Particles	9
C. Impurities	11
D. Steady-State Solutions	16
II. SURFACE PHENOMENA	26
A. Physical Sputtering	27
B. Neutron Sputtering	57
C. Chemical Sputtering	57
D. Reflection Coefficients	64
E. Transmutation Products	69
F. Blistering	71
III. ATOMIC PROCESS IN THE PLASMA	73
A. Charge-Exchange Probability	73
B. Impurity Radiation	75
IV. IMPURITY CONTROL AND REACTOR PERFORMANCE	83
A. Steady-State Simulation	83
B. Dynamic Simulation	101
V. SUMMARY AND CONCLUSIONS	112
REFERENCES	114

LIST OF TABLES

<u>No.</u>	<u>Title</u>	<u>Page</u>
I	Parameters for Calculation of Physical Sputter Yields for Metallic Wall Materials	34
II	Parameters for Calculation of Physical Sputter Yields for Compound Wall Materials	46
III	Comparison of Calculated Ratios of Oxide-to-Metal Sputter Yields for 10-keV Krypton with Experimental Data	53
IV	Maxwellian-Averaged Physical Sputter Coefficients	55
V	Helium and Hydrogen Production Rates in Candidate, First-Wall Materials	70
VI	Atomic Processes	77

LIST OF FIGURES

<u>No.</u>	<u>Title</u>	<u>Page</u>
1a	Schematic of D-T particle flows	5
1b	Schematic of alpha particle flows	10
1c	Schematic of wall-sputtered impurity particle flows	12
1d	Schematic of divertor chamber sputtered impurity particle flows ..	14
2	Calculated energy-dependent physical sputter yields of candidate first-wall materials bombarded with monoenergetic deuterium ions .	35
3	Calculated energy-dependent physical sputter yields of candidate first-wall materials bombarded with monoenergetic helium ions	36
4	Calculated energy-dependent physical sputter yield curves for candidate first-wall materials	37
5	Plot of calculated energy-dependent physical sputter yield curves for iron (stainless steel) showing comparison with available experimental data	38
6	Plot of calculated energy-dependent physical sputter yield curves for niobium showing comparison with available experimental data ..	39
7	Plot of calculated energy-dependent physical sputter yield curves for molybdenum showing comparison with available experimental data	40
8	Plot of calculated energy-dependent physical sputter yield curves for tungsten showing comparison with available experimental data .	41
9	Plot of calculated energy-dependent physical sputter yield curves for carbon (graphite) showing comparison with available experimental data	42
10	Calculated energy-dependent physical sputter yields of compound first-wall materials bombarded with monoenergetic deuterium ions .	47
11	Calculated energy-dependent physical sputter yields of compound first-wall materials bombarded with monoenergetic helium ions	48
12	Calculated energy-dependent physical sputter yields for compound first-wall materials bombarded by monoenergetic self-ions	50

LIST OF FIGURES (Contd.)

<u>No.</u>	<u>Title</u>	<u>Page</u>
13	Plot of calculated energy-dependent physical sputter yield curves for SiC showing comparison with available experimental data	51
14	Plot of calculated energy-dependent physical sputter yields for B ₄ C showing comparison with available experimental data	52
15	Temperature dependence of sputter yields for hydrogen ions on carbon	59
16	Effect of temperature and crystal orientation on the reaction probability of hydrogen with carbon	60
17	Calculated reflection coefficients for deuterium and helium incident on beryllium and iron	66
18	Helium re-emission during 300-keV helium implantation as a function of fluence at three different implantation temperatures in vanadium	68
19	Deuterium-tritium atomic process rates. Atomic charge-exchange, electron impact ionization and ion-impact ionization rates versus effective temperature for atoms of mass 2.5 amu	74
20	Oxygen radiation loss	81
21	Iron radiation loss	82
22a	Normalized wall-sputtered and alpha impurity concentrations and fuel replenishment rate as a function of unload divertor efficiency and divertor backflow fraction	84
22b	Normalized wall-sputtered impurity concentration as a function of unload and shielding divertor efficiencies and divertor backflow fraction	85
22c	Normalized divertor-chamber-sputtered impurity concentration as a function of unload shielding efficiency and the parameter γ_c	86
22d	Normalized wall-sputtered impurity concentration as a function of unload shielding efficiency and plasma-edge temperature	87
23a	Normalized wall-sputtered impurity concentration as a function of shielding divertor efficiency and divertor backflow fraction	89
23b	Normalized wall-sputtered impurity concentration as a function of shielding and unload divertor efficiencies	90

LIST OF FIGURES (Contd.)

<u>No.</u>	<u>Title</u>	<u>Page</u>
23c	Normalized divertor-chamber-sputtered impurity concentration as a function of shielding divertor efficiency and the parameter γ_c ...	91
23d	Normalized wall-sputtered impurity concentration as a function of shielding divertor efficiency and plasma-edge temperature	92
24a	Energy confinement required for ignition as a function of beryllium impurity concentration	95
24b	Energy confinement required for ignition as a function of iron impurity concentration	96
24c	Energy confinement required for ignition as a function of molybdenum impurity concentration	97
24d	Energy confinement required for ignition as a function of tungsten impurity concentration	98
25	Maximum impurity concentration for which ignition can be achieved	99
26	Effect of the radiation model on the predicted energy confinement required for ignition	100
27	Reactor power output as a function of first-surface material ($T_{\text{edge}} = 200$ eV)	104
28	Reactor power output as a function of first-surface material and plasma-edge temperature	105
29	Enhancement of reactor power output by supplemental heating ($T_{\text{edge}} = 200$ eV)	106
30	Reactor power output as a function of unload divertor efficiency and first-surface material	108
31	Reactor power output as a function of unload divertor efficiency with a steel first-surface and $T_{\text{edge}} = 60$ eV	109
32	Reactor power output as a function of shielding divertor efficiency and first-surface material	111

IMPURITY CONTROL IN TOKAMAK REACTORS

W. M. Stacey, Jr., D. L. Smith, J. N. Brooks,
P. J. Bertoncini and D. A. Ehst

*Fusion Power Program
Argonne National Laboratory
Argonne, Illinois 60439*

ABSTRACT

A computational model is developed for the plasma-wall-divertor interactions in a D-T burning tokamak. The data bases for important surface and atomic processes in the plasma are reviewed. An expression for the physical sputtering yield is presented and compared with experimental results. Numerical results are presented to illustrate the effect of impurity contamination upon plasma performance, to evaluate the use of low-Z first-wall surfaces and magnetic divertors for impurity control, and to assess the sensitivity of these results to uncertainties in the data and the computational models.

INTRODUCTION

Contamination of the plasma by wall-eroded impurity ions may be a serious problem in near-term tokamak experiments and in future tokamak reactors. The atomic line and recombination radiation associated with these impurity ions constitute a power loss which could prohibit the achievement of a self-sustaining power balance, or ignition. The physical processes which lead to wall erosion and the effect of impurity contamination upon the plasma have been discussed by several authors — e.g. Refs. 1-7.

It is generally recognized that some form of impurity control will be required for tokamak reactors. Magnetic divertors,⁽⁸⁻¹⁰⁾ in which the magnetic field structure is such that ions that find themselves in a scrape-off region between the plasma and the first-wall are swept out of the plasma chamber, were among the first impurity control measures suggested, and recent experimental results in tokamaks⁽¹¹⁾ have been encouraging. It has been suggested⁽¹²⁾ that a "cool" gas blanket surrounding the hot plasma could effectively insulate it from the first-wall by reducing the energy of particles incident upon the wall (sputtering rates generally increase with incident particle energy in the range of interest) and by trapping the impurity ions before they can reach the plasma. A flowing gas blanket could, furthermore, alter the particle flows within the plasma in such a way as to reverse the classically predicted inward diffusion of impurity ions.⁽¹³⁾ A third class of impurity control measures consists of modifications to the first-wall such that the first-surface upon which the plasma particles are incident is made of a low-atomic-number (low-Z) material. Because radiative power losses increase dramatically with the atomic number of the ion, substitution of a low-Z impurity for a high-Z impurity can be very beneficial for the plasma power balance. Several types of first-wall modifications are reviewed in Ref. 6.

The purposes of this report are to evaluate the possible impact of wall-eroded impurity contamination upon the power performance of tokamak reactors, to assess how this performance can be improved by two impurity control techniques — magnetic divertors and first-wall modification, to assess the data base for important wall-erosion and atomic processes in the plasma, and to determine the sensitivity of the reactor power performance to the parameters which describe the impurity control technique, to the data base and to the calculational model for radiative power losses. A computational model for the plasma-wall-divertor interaction is described in Section I. The data base for the surface phenomena which cause wall erosion is evaluated in Section II, and the data base for relevant atomic processes in the plasma is reviewed in Section III. Numerical results, which illustrate the impact of impurity contamination on power performance and the possible amelioration of this impact by magnetic divertors and/or first-wall modification, are discussed in Section IV. Conclusions of the study are summarized in Section V.

I. PLASMA-WALL-DIVERTOR INTERACTION MODEL

A model has been formulated in which the particle fluxes to the first-wall, the divertor chamber, and the plasma are written in terms of a few, physically motivated parameters which characterize the important processes involved in the plasma-wall-divertor interaction — divertor unload and shielding efficiencies, charge-exchange probabilities, sputtering yields, particle reflection coefficients, and probabilities for diverted particles subsequently backflowing into the plasma chamber. The formulation reduces to a plasma-wall interaction model, without impurity control, with an appropriate choice of parameter values.

A. Deuterium-Tritium

The flux of deuterium-tritium (D-T) ions into the divertor chamber is (see [1] in Fig. 1a)

$$\begin{aligned} \Gamma_{DT}^{div} = & \eta_{DT}^U \frac{n_{DT}}{\tau_{DT}} + \eta_{DT}^S (1 - \xi_{cx}) R_{DT}^d \Gamma_{DT}^{div} + \eta_{DT}^S (1 - \xi_{cx}) R_{DT}^W \Gamma_{DT}^{wall} \\ & + \eta_{DT}^{S_{ext}} \left(1 - \xi_{cx}^{ext} \right) S_{DT}^{ext} . \end{aligned} \quad (1)$$

The first term represents D-T ions escaping from the plasma which are swept into the divertor chamber. The second term represents D-T particles (ions or atoms) which flow back from the divertor chamber into the plasma chamber and are swept into the divertor chamber again. The third term represents D-T particles (ions or atoms) which are reflected from the first wall and then swept into the divertor chamber. The last term represents the fraction of the externally injected source, S_{DT}^{ext} , which is swept into the divertor chamber before reaching the plasma. The rate at which D-T ions escape from the

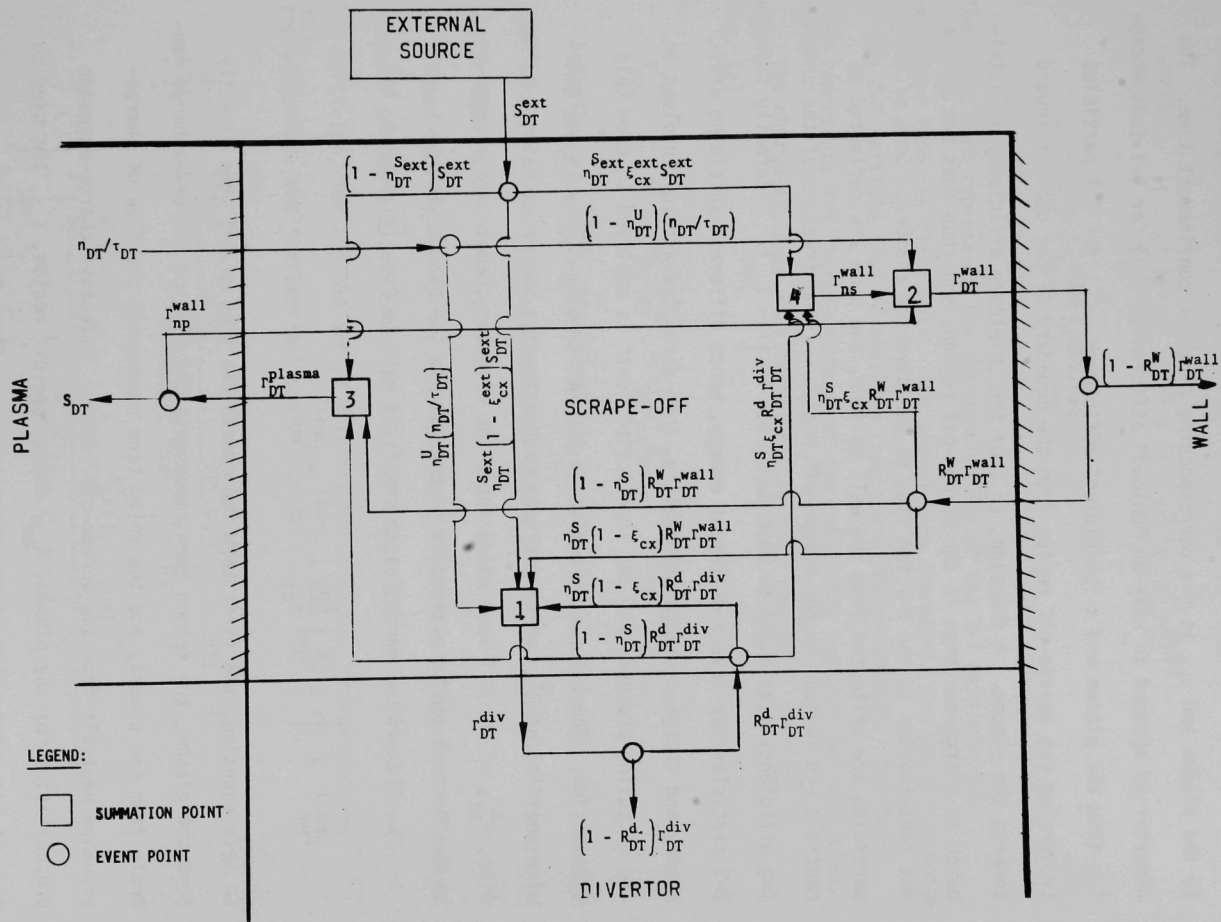


Fig. 1a. Schematic of D-T particle flows.

plasma is represented by n_{DT}/τ_{DT} , where n_{DT} is the average D-T ion density in the plasma and τ_{DT} is the corresponding particle confinement time. The divertor is assumed to have an "unload" efficiency, η_{DT}^U , for D-T ions escaping from the plasma and a "shielding" efficiency, η_{DT}^S , for D-T particles traversing the scrape-off region from the boundary of the chamber inward towards the plasma. A fraction, ξ_{cx} , of the shielding efficiency is attributed to charge-exchange in the scrape-off region, and thus does not make a net contribution to the D-T ion flux to the divertor chamber. Some of the particles are reflected from the wall as ions, and some are reflected as neutrals and ionized in the scrape-off region — the fraction of the shielding efficiency attributed to such particles is $(1 - \xi_{cx})$. Externally injected D-T particles may have a different energy, hence different shielding efficiency and charge-exchange probability, than particles already involved in the recycling process, and the superscript "ext" is employed to draw this distinction. The D-T particle flux to the first wall, Γ_{DT}^{wall} , is reflected with coefficient R_{DT}^W , which includes backscattering and re-emission. A fraction, R_{DT}^d , of the D-T ions which enter the divertor chamber are assumed to be "reflected" and to ultimately re-emerge into the plasma chamber.

The flux of D-T particles to the first wall is (see [2] in Fig. 1a)

$$\Gamma_{DT}^{wall} = \left(1 - \eta_{DT}^U\right) \frac{n_{DT}}{\tau_{DT}} + \Gamma_{np}^{wall} + \Gamma_{ns}^{wall}. \quad (2)$$

In this equation, the first term represents the flux of D-T ions directly from the plasma, the second term represents the flux of charge-exchange neutrals from the plasma, and the third term represents the flux of charge-exchange neutrals from the scrape-off region. Effective charge-exchange probabilities for the plasma, A_{cx} , and scrape-off region, ξ_{cx} , are used to account for attenuation of the charge-exchange flux; $0 \leq \xi_{cx}, A_{cx} \leq 1$.

The charge-exchange flux from the plasma is (see [3] in Fig. 1a)

$$\begin{aligned} \Gamma_{np}^{wall} = & \left(1 - \eta_{DT}^S\right) A_{cx} R_{DT}^W \Gamma_{DT}^{wall} + \left(1 - \eta_{DT}^S\right) A_{cx} R_{DT}^d \Gamma_{DT}^{div} \\ & + \left(1 - \eta_{DT}^{S_{ext}}\right) A_{cx} S_{DT}^{ext} . \end{aligned} \quad (3)$$

The first term represents the charge-exchange of the D-T particle flux reflected from the first wall. The second term represents the charge-exchange of the D-T particle flux re-emerging from the divertor chamber. The third term represents the charge-exchange of the externally injected D-T particles.

The charge-exchange flux from the scrape-off region is (see [4] in Fig. 1a)

$$\Gamma_{ns}^{wall} = \eta_{DT}^S \xi_{cx} R_{DT}^W \Gamma_{DT}^{wall} + \eta_{DT}^S \xi_{cx} R_{DT}^d \Gamma_{DT}^{div} + \eta_{DT}^{S_{ext}} \xi_{cx} S_{DT}^{ext} . \quad (4)$$

The three terms represent the same type quantities as in Eq. (3), except that in Eq. (4) the charge-exchange is taking place in the scrape-off region rather than in the plasma.

These four equations may be solved for the various D-T particle fluxes in terms of the D-T ion loss rate from the plasma and the external source of D-T particles, for a given set of divertor efficiencies, charge-exchange probabilities, and "reflection" coefficients.

$$\begin{aligned} \Gamma_{DT}^{div} = & \left[\frac{\eta_{DT}^U \left(1 - \phi_{cx} R_{DT}^W\right) + \left(1 - \eta_{DT}^U\right) R_{DT}^W \eta_{DT}^S \left(1 - \xi_{cx}\right)}{1 - R_{DT}^d \eta_{DT}^S \left(1 - \xi_{cx}\right) - \phi_{cx} R_{DT}^W} \right] \frac{\eta_{DT}}{\tau_{DT}} \\ & + \left[\frac{\phi_{cx}^{ext} R_{DT}^W \eta_{DT}^S \left(1 - \xi_{cx}\right) + \eta_{DT}^{S_{ext}} \left(1 - \xi_{cx}^{ext}\right) \left(1 - \phi_{cx} R_{DT}^W\right)}{1 - R_{DT}^d \eta_{DT}^S \left(1 - \xi_{cx}\right) - \phi_{cx} R_{DT}^W} \right] S_{DT}^{ext} \end{aligned}$$

$$\equiv W_{DT} \cdot \frac{n_{DT}}{\tau_{DT}} + V_{DT} \cdot S_{DT}^{ext}, \quad (5)$$

$$\begin{aligned} \Gamma_{np}^{wall} = & \left[\frac{(1 - \eta_{DT}^S) A_{cx}}{1 - R_{DT}^d \eta_{DT}^S (1 - \xi_{cx}) - \phi_{cx} R_{DT}^W} \right] \left[\left\{ R_{DT}^W (1 - \eta_{DT}^U) + \eta_{DT}^U R_{DT}^d \right\} \frac{n_{DT}}{\tau_{DT}} \right. \\ & \left. + \left\{ \eta_{DT}^{S_{ext}} (1 - \xi_{cx}^{ext}) R_{DT}^d + R_{DT}^W \phi_{cx}^{ext} \right\} S_{DT}^{ext} \right] + (1 - \eta_{DT}^{S_{ext}}) A_{cx}^{ext} S_{DT}^{ext}, \quad (6) \end{aligned}$$

and

$$\begin{aligned} \Gamma_{ns}^{wall} = & \left[\frac{\eta_{DT}^S \xi_{cx}}{1 - R_{DT}^d \eta_{DT}^S (1 - \xi_{cx}) - \phi_{cx} R_{DT}^W} \right] \left[\left\{ R_{DT}^W (1 - \eta_{DT}^U) + \eta_{DT}^U R_{DT}^d \right\} \frac{n_{DT}}{\tau_{DT}} \right. \\ & \left. + \left\{ \eta_{DT}^{S_{ext}} (1 - \xi_{cx}^{ext}) R_{DT}^d + R_{DT}^W \phi_{ex}^{ext} \right\} S_{DT}^{ext} \right] + \eta_{DT}^{S_{ext}} \xi_{cx}^{ext} S_{DT}^{ext}, \quad (7) \end{aligned}$$

where the total charge-exchange probability, ϕ_{cx} , is defined

$$\phi_{cx} \equiv (1 - \eta_{DT}^S) A_{cx} + \eta_{DT}^S \xi_{cx}. \quad (8)$$

The net source of D-T ions to the plasma from the recycling process and the external source is (see [3] in Fig. 1a)

$$S_{DT} = \left(1 - \eta_{DT}^S\right) \left[R_{DT}^W \Gamma_{DT}^{wall} + R_{DT}^d \Gamma_{DT}^{div} \right] \left(1 - A_{cx}\right) + \left(1 - \eta_{DT}^{Sext}\right) \left(1 - A_{cx}^{ext}\right) S_{DT}^{ext}. \quad (9)$$

The D-T ion balance equation for the plasma is

$$\dot{n}_{DT} = S_{DT} - 2p(1-p) \overline{\sigma v} n_{DT}^2 (1 + \xi) - \frac{n_{DT}}{\tau_{DT}}, \quad (10)$$

where p is the tritium fraction of the D-T mix, $\overline{\sigma v}$ is the Maxwellian-average fusion cross section, and the factor ξ accounts for suprathermal fusion when neutral beam injection is included.

B. Alpha Particles

The flux of alpha particles into the divertor chamber is (see [5] in Fig. 1b)

$$\Gamma_{\alpha}^{div} = \eta_{\alpha}^U \frac{n_{\alpha}}{\tau_{\alpha}} + \eta_{\alpha}^S \left(1 - \eta_{\alpha}^U\right) R_{\alpha}^W \frac{n_{\alpha}}{\tau_{\alpha}} + \eta_{\alpha}^S R_{\alpha}^d \Gamma_{\alpha}^{div}. \quad (11)$$

In this equation, the first term represents diversion of alpha particles as they escape from the plasma, the second term represents diversion of alpha particles that have reflected from the first wall, and the third term represents diversion of alpha particles that are emerging from the divertor chamber. The nomenclature corresponds in an obvious way to that defined for Eq. (1).

Equation (11) may be rewritten

Fig. 1b. Schematic of alpha particle flows.

$$\Gamma_{\alpha}^{\text{div}} = K_{\alpha} \frac{n_{\alpha}}{\tau_{\alpha}}, \quad (11')$$

where the overall divertor efficiency for alpha particles is defined

$$K_{\alpha} \equiv \frac{\eta_{\alpha}^U + (1 - \eta_{\alpha}^U) \eta_{\alpha}^S R_{\alpha}^W}{1 - \eta_{\alpha}^S R_{\alpha}^d}. \quad (12)$$

The alpha flux to the first wall is (see [6] in Fig. 1b)

$$\Gamma_{\alpha}^{\text{wall}} = (1 - \eta_{\alpha}^U) \frac{n_{\alpha}}{\tau_{\alpha}}. \quad (13)$$

The source of alphas recycling to the plasma is (see [7] in Fig. 1b)

$$S_{\alpha} = (1 - \eta_{\alpha}^S) R_{\alpha}^d \Gamma_{\alpha}^{\text{div}} + (1 - \eta_{\alpha}^S) R_{\alpha}^W \Gamma_{\alpha}^{\text{wall}}. \quad (14)$$

The alpha particle balance equation in the plasma is

$$\dot{n}_{\alpha} = p(1 - p) \overline{\sigma v} n_{DT}^2 (1 + \xi) + S_{\alpha} - \frac{n_{\alpha}}{\tau_{\alpha}}. \quad (15)$$

C. Impurities

Impurities sputtered from the first wall and from the collector plate in the divertor chamber are treated separately. The flux of wall-sputtered impurities, which will be identified with the subscript z , into the divertor chamber is (see [8] in Fig. 1c)

$$\Gamma_z^{\text{div}} = \eta_z^U \frac{n_z}{\tau_z} + \eta_z^S R_z^d \Gamma_z^{\text{div}} + \eta_z^S \Gamma_z^-,$$

which may be written,

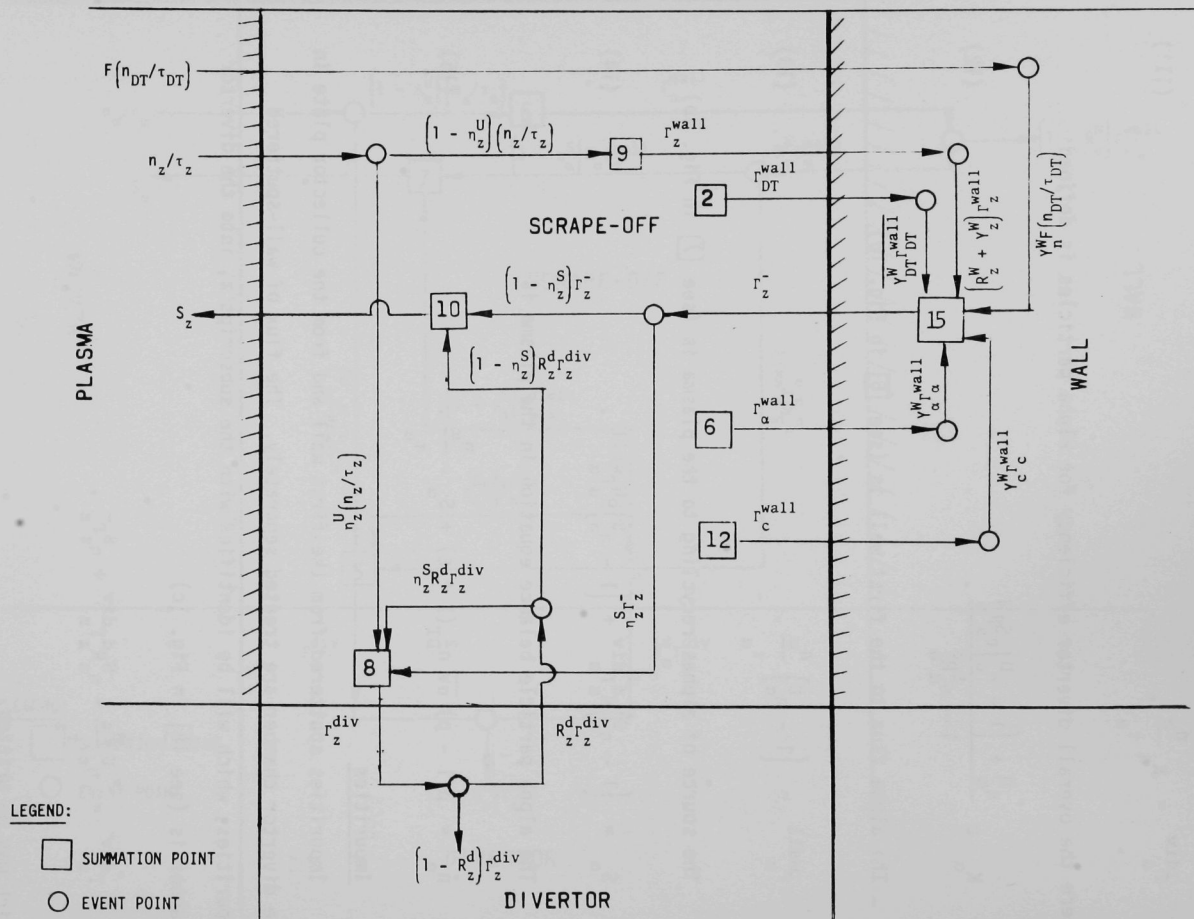


Fig. 1c. Schematic of wall-sputtered impurity particle flows.

$$\Gamma_z^{\text{div}} = \frac{\eta_z^U (n_z / \tau_z) + \eta_z^S \Gamma_z^-}{1 - \eta_z^S R_z^d}, \quad (16)$$

where Γ_z^- is the impurity flux from the first wall and is defined in Eq. (21). (see [15] in Fig. 1c.)

Similarly, the flux of collector-sputtered impurities, which will be identified by the subscript c, is (see [11] in Fig. 1d)

$$\Gamma_c^{\text{div}} = \left[\eta_c^U + \eta_c^S R_c^W (1 - \eta_c^U) \right] \frac{n_c}{\tau_c} + \eta_c^S \Gamma_c^-, \quad (17)$$

where Γ_c^- is the impurity flux returning from the divertor,

$$\Gamma_c^- = \left\{ \frac{\left[\gamma_c^c \gamma_c^c + R_c^d \right] \left[\eta_c^U + \eta_c^S R_c^W (1 - \eta_c^U) \right]}{1 - \eta_c^S (\gamma_c^c \gamma_c^c + R_c^d)} \right\} \frac{n_c}{\tau_c} + \frac{\gamma_c (\gamma_{DT}^c \Gamma_{DT}^{\text{div}} + \gamma_{\alpha}^c \Gamma_{\alpha}^{\text{div}} + \gamma_z^c \Gamma_z^{\text{div}})}{1 - \eta_c^S (\gamma_c^c \gamma_c^c + R_c^d)}. \quad (18)$$

The fluxes of impurity ions to the first wall are

$$\Gamma_z^{\text{wall}} = \left(1 - \eta_z^U \right) \frac{n_z}{\tau_z}, \quad (19)$$

and

$$\Gamma_c^{\text{wall}} = \left(1 - \eta_c^U \right) \frac{n_c}{\tau}. \quad (20)$$

The source of wall-sputtered impurities to the plasma is

LEGEND:



SUMMATION POINT



EVENT POINT

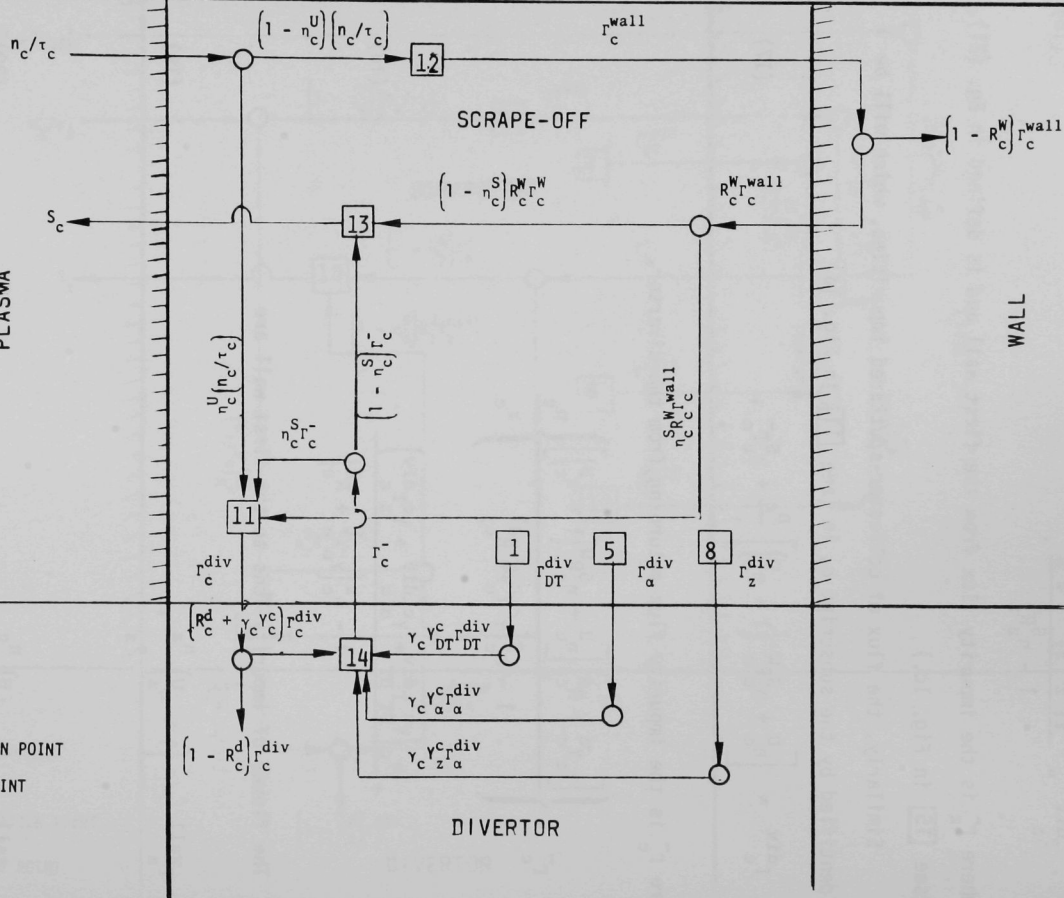


Fig. 1d. Schematic of divertor chamber sputtered particle flows.

$$S_z = (1 - \eta_z^S) \left[\left(Y_z^W + R_z^W \right) \Gamma_z^{\text{wall}} + \overline{Y_{DT}^W \Gamma_{DT}^{\text{wall}}} + Y_\alpha^W \Gamma_\alpha^{\text{wall}} + Y_c^W \Gamma_c^{\text{wall}} + F \frac{n_{DT}}{\tau_{DT}} Y_n^W + R_z^d \Gamma_z^{\text{div}} \right] \equiv (1 - \eta_z^S) \left[\Gamma_z^- + R_z^d \Gamma_z^{\text{div}} \right]. \quad (21)$$

The first term represents the impurity flux returning from the first wall due to self-sputtering, with yield Y_z^W , and to reflection, with coefficient R_z^W . The second term represents the impurity flux to the plasma due to D-T sputtering of the first wall and is a composite term defined as

$$\overline{Y_{DT}^W \Gamma_{DT}^{\text{wall}}} = Y_{DT}^W (T_{\text{edge}}) \left(1 - \eta_{DT}^U \right) \frac{n_{DT}}{\tau_{DT}} + Y_{DT}^W (T_{np}) \Gamma_{np}^{\text{wall}} + Y_{DT}^W (T_{ns}) \Gamma_{ns}^{\text{wall}}, \quad (22)$$

where the arguments indicate that the sputtering yields are evaluated at temperatures corresponding to the ion temperature at the edge of the plasma, T_{edge} , the temperature characteristic of charge-exchange neutrals from the plasma, T_{np} , and the temperature characteristic of charge-exchange neutrals from the scrape-off region, T_{ns} . The third and fourth terms in Eq. (21) represent impurity fluxes to the plasma due to first-wall sputtering by alpha particles and collector-sputtered impurities, respectively. The fifth term represents the impurity flux to the plasma due to neutron sputtering, where F is the ratio of the fusion rate to the D-T ion loss rate in the plasma

$$F = p(1 - p) \overline{\sigma v} (1 + \xi) \{ n_{DT} \tau_{DT} \}. \quad (23)$$

The balance equation for wall-sputtered impurities in the plasma is

$$\dot{n}_z = S_z - \frac{n_z}{\tau_z}. \quad (24)$$

The source of collector-sputtered impurities in the plasma is (see [13] in Fig. 1d)

$$\begin{aligned} S_c &= \left(1 - \eta_c^S\right) \left[R_c^W \Gamma_c^{\text{wall}} + \gamma_c \left(\gamma_{DT}^c \Gamma_{DT}^{\text{div}} + \gamma_{\alpha}^c \Gamma_{\alpha}^{\text{div}} + \gamma_z^c \Gamma_z^{\text{div}} + \gamma_c^c \Gamma_c^{\text{div}} \right) + R_c^d \Gamma_c^{\text{div}} \right] \\ &\equiv \left(1 - \eta_c^S\right) \left[R_c^W \Gamma_c^{\text{wall}} + \Gamma_c^- \right]. \end{aligned} \quad (25)$$

The first term in Eq. (25) represents the impurity flux reflected from the first wall, and the last term represents the impurity flux "reflected" from the divertor. The middle term represents an impurity flux emerging from the divertor chamber into the plasma chamber due to sputtering of the collector plate or divertor chamber. The parameter γ_c is included to represent both the enhancement of the sputtering due to charge-exchange within the divertor chamber and the probability that a sputtered particle will eventually reach the plasma chamber. Sputtering yields, γ^c , from the divertor chamber are evaluated for an incident particle temperature, T_c , characteristic of the plasma in the divertor chamber.

The balance equation for the collector-sputtered impurities in the plasma is

$$\dot{n}_c = S_c - \frac{n_c}{\tau_c}. \quad (26)$$

D. Steady-State Solutions

It is of interest to determine the conditions under which steady-state solutions of the particle balance equations exist and to understand how these

solutions depend upon the parameters which characterize the plasma-wall-divertor interaction. To this end the time derivatives in Eqs. (10), (15), (24), and (26) may be set equal to zero, and then the equations of the previous section may be solved for the steady-state particle concentrations in the plasma and particle fluxes to the first wall and divertor.

The source of externally injected D-T particles that is required to maintain the D-T ion density in the plasma is related to the D-T ion loss rate from the plasma.

$$S_{DT}^{ext} = \frac{2F + 1 - C_{DT}}{B_{DT}} \cdot \frac{n_{DT}}{\tau_{DT}}, \quad (27)$$

where

$$B_{DT} \equiv \left(1 - n_{DT}^S\right) \left(1 - A_{cx}\right) \left[\frac{\phi_{cx}^{ext} R_{DT}^W + R_{DT}^d S_{DT}^{ext} (1 - \xi_{cx}^{ext})}{1 - R_{DT}^d n_{DT}^S (1 - \xi_{cx}) - \phi_{cx} R_{DT}^W} \right] + \left(1 - n_{DT}^{S_{ext}}\right) \left(1 - A_{cx}^{ext}\right), \quad (28)$$

and

$$C_{DT} \equiv \left(1 - n_{DT}^S\right) \left(1 - A_{cx}\right) \left[\frac{n_{DT}^U R_{DT}^d + (1 - n_{DT}^U) R_{DT}^W}{1 - R_{DT}^d n_{DT}^S (1 - \xi_{cx}) - \phi_{cx} R_{DT}^W} \right]. \quad (29)$$

The relative alpha particle and impurity concentrations in the plasma are

$$\frac{n_\alpha}{n_{DT}} = \left[\frac{\tau_\alpha}{\tau_{DT}} \right] \frac{F}{1 - f_\alpha}, \quad (30)$$

$$\begin{aligned}
\frac{n_z}{n_{DT}} = & \left(\frac{\tau_z}{\tau_{DT}} \right) D^{-1} \left(1 - \eta_z^S \right) \left\{ \left[\left(1 - \eta_c^U \right) \gamma_c^W \left(1 - \eta_c^S \right) \gamma_c \left\{ \gamma_{DT}^c H_{DT} + \frac{\gamma_\alpha^c K_\alpha F}{1 - f_\alpha} \right. \right. \right. \\
& + \left. \left. \frac{\eta_z^S \gamma_z^c}{1 - \eta_z^S R_z^d} \left[\overline{\gamma_{DT}^W G} + \frac{\gamma_\alpha^W (1 - \eta_\alpha^U) F}{1 - f_\alpha} + \gamma_n^W F \right] \right\} \right. \\
& + \left. \left[1 - \left\{ \left(\eta_c^S + \left(1 - \eta_c^S \right) \left[\eta_c^U + \eta_c^S \left(1 - \eta_c^U \right) R_c^W \right] \right) \left(\gamma_c \gamma_c^c + R_c^d \right) \right\} \right. \right. \\
& - \left. \left. \left\{ \frac{\left(1 - \eta_c^S \right) \left(1 - \eta_c^U \right) \gamma_c \gamma_z^c \eta_z^S \gamma_z^W}{1 - \eta_z^S R_z^d} \right\} \right] \left[\overline{\gamma_{DT}^W G} + \frac{\gamma_\alpha^W (1 - \eta_\alpha^U) F}{1 - f_\alpha} + \gamma_n^W F \right] \right\}, \quad (31)
\end{aligned}$$

and

$$\begin{aligned}
\frac{n_c}{n_{DT}} = & \left(\frac{\tau_c}{\tau_{DT}} \right) D^{-1} \left(1 - \eta_c^S \right) \gamma_c \left\{ K_z \gamma_z^c \left(1 - \eta_z^S \right) \left[\overline{\gamma_{DT}^W G} + \frac{\gamma_\alpha^W (1 - \eta_\alpha^U) F}{1 - f_\alpha} + \gamma_n^W F \right] \right. \\
& + \left. \left[1 - \left(1 - \eta_z^S \right) \left(1 - \eta_z^U \right) \left(R_z^W + \gamma_z^W \right) - R_z^d \left\{ 1 - \left(1 - \eta_z^S \right) \left(1 - \eta_z^U \right) \right\} \right] \right. \\
& \times \left. \left[\gamma_{DT}^c H_{DT} + \frac{\gamma_\alpha^c K_\alpha F}{1 - f_\alpha} + \frac{\gamma_z^c \eta_z^S}{1 - \eta_z^S R_z^d} \left\{ \overline{\gamma_{DT}^W G} + \frac{\gamma_\alpha^W (1 - \eta_\alpha^U) F}{1 - f_\alpha} + \gamma_n^W F \right\} \right] \right\}. \quad (32)
\end{aligned}$$

Several composite terms introduced in these equations are defined as follows:

$$f_{\alpha} \equiv \frac{(1 - \eta_{\alpha}^S) \left[R_{\alpha}^W (1 - \eta_{\alpha}^U) + R_{\alpha}^d \eta_{\alpha}^U \right]}{1 - \eta_{\alpha}^S R_{\alpha}^d} \quad (33)$$

is the net recycling probability for alpha particles that escape from the plasma;

$$H_{DT} \equiv W_{DT} + \frac{2F + (1 - C_{DT})}{B_{DT}} V_{DT} \quad (34)$$

is the overall divertor efficiency related to D-T ions escaping from the plasma, but including the diversion of externally injected D-T ions as well, i.e.

$$\Gamma_{DT}^{div} = H_{DT} \frac{n_{DT}}{\tau_{DT}}; \quad (35)$$

$$K_z \equiv \frac{\eta_z^U + \eta_z^S (1 - \eta_z^U) (\gamma_z^W + R_z^W)}{1 - \eta_z^S R_z^d} \quad (36)$$

is the overall divertor efficiency for impurity (z) ions escaping from the plasma;

$$D \equiv \left(\left\{ 1 - (1 - \eta_z^S) (1 - \eta_z^U) (R_z^W + \gamma_z^W) - R_z^d \left[1 - (1 - \eta_z^S) (1 - \eta_z^U) \right] \right\} \right. \\ \times \left\{ 1 - (\gamma_c \gamma_c^c + R_c^d) \left[\eta_c^S + (1 - \eta_c^S) \left[\eta_c^U + \eta_c^S (1 - \eta_c^U) R_c^W \right] \right] \right. \\ \left. \left. - \frac{(1 - \eta_c^S) (1 - \eta_c^U) \gamma_c \gamma_z^c \eta_z^S \gamma_c^c}{1 - \eta_z^S R_z^d} \right\} - (1 - \eta_z^S) (1 - \eta_c^U) (1 - \eta_c^S) \gamma_z^W \gamma_c^c K_z \right); \quad (37)$$

$$\begin{aligned}
\overline{Y_{DT}^W} \equiv & \left[\left(1 - \eta_{DT}^U \right) Y_{DT}^W(T_{edge}) \right] + \frac{2F + (1 - C_{DT})}{B_{DT}} \left[\left(1 - \eta_{DT}^{S_{ext}} \right) A_c^{ext} Y_{DT}^W(T_{np}) \right. \\
& + \left. \eta_{DT}^{S_{ext}} \xi_{cx}^{ext} Y_{DT}^W(T_{ns}) \right] + \left\{ R_{DT}^W \left(1 - \eta_{DT}^U \right) + \eta_{DT}^U R_{DT}^d \right\} \\
& + \frac{2F + (1 - C_{DT})}{B_{DT}} \left\{ \eta_{DT}^{S_{ext}} \left(1 - \xi_{cx}^{ext} \right) R_{DT}^d + \phi_{cx}^{ext} R_{DT}^W \right\} \\
& \times \left[\frac{\left(1 - \eta_{DT}^S \right) A_{cx} Y_{DT}^W(T_{np}) + \eta_{DT}^S \xi_{cx} Y_{DT}^W(T_{ns})}{1 - R_{DT}^d \eta_{DT}^S (1 - \xi_{cx}) - \phi_{cx} R_{DT}^W} \right] \quad (38)
\end{aligned}$$

is a composite term which, when multiplied by n_{DT}/τ_{DT} , defines the first-wall sputtering rate by D-T particles. The sputtering yields are to be evaluated as discussed for Eq. (22). The three terms in Eq. (38) represent sputtering due to D-T ions escaping from the plasma, due to charge-exchange neutrals produced by the externally injected D-T source, and due to charge-exchange neutrals produced by the recycling D-T particles, respectively.

Particle fluxes to the first wall are proportional to the D-T ion loss rate from the plasma.

$$\begin{aligned}
r_{DT}^{wall} = & \left[\left(1 - \eta_{DT}^U \right) + \left\{ \frac{\phi_{cx} \left[R_{DT}^W \left(1 - \eta_{DT}^U \right) + \eta_{DT}^U R_{DT}^d \right]}{1 - R_{DT}^d \eta_{DT}^S \left(1 - \xi_{cx} \right) - \phi_{cx} R_{DT}^W} + \frac{1 - c_{DT}}{B_{DT}} \right. \right. \\
& \times \left. \left[\phi_{cx}^{ext} \left(1 - R_{DT}^d \eta_{DT}^S \left(1 - \xi_{cx} \right) \right) + \phi_{cx} \eta_{DT}^{Sext} \left(1 - \xi_{cx}^{ext} \right) R_{DT}^d \right] \right\} \\
& \left. + \left\{ \frac{2F}{B_{DT}} \left[\phi_{cx}^{ext} \left(1 - R_{DT}^d \eta_{DT}^S \left(1 - \xi_{cx} \right) \right) + \phi_{cx} \eta_{DT}^{Sext} \left(1 - \xi_{DT}^{ext} \right) R_{DT}^d \right] \right\} \right] \cdot \frac{n_{DT}}{\tau_{DT}} .
\end{aligned} \tag{39}$$

The alpha and impurity fluxes to the first wall can be written

$$r_x^{wall} = \left(1 - \eta_x^U \right) \frac{n_x}{\tau_x} = \left(1 - \eta_x^U \right) \left(\frac{n_x}{n_{DT}} \right) \left(\frac{\tau_{DT}}{\tau_x} \right) \frac{n_{DT}}{\tau_{DT}}, \quad x = \alpha, z, c. \tag{40}$$

Particle fluxes to the divertor chamber can also be written as proportional to the D-T ion loss rate. The D-T flux is given by Eq. (35); the alpha flux is given by Eq. (11'), which may be written

$$r_{\alpha}^{div} = K_{\alpha} \frac{n_{\alpha}}{\tau_{\alpha}} = K_{\alpha} \left(\frac{n_{\alpha}}{n_{DT}} \right) \left(\frac{\tau_{DT}}{\tau_{\alpha}} \right) \frac{n_{DT}}{\tau_{DT}} = \frac{K_{\alpha}^F}{1 - f_{\alpha}} \frac{n_{DT}}{\tau_{DT}}; \tag{41}$$

the wall-sputtered impurity flux is given by Eq. (16), which may be written

$$\Gamma_z^{\text{div}} = \left\{ K_z \left(\frac{n_z}{n_{DT}} \right) \left(\frac{\tau_{DT}}{\tau_z} \right) + \frac{n_z^S}{1 - n_z^S R_z^d} \left[\gamma_{DT}^W G + \frac{\gamma_\alpha^W (1 - n_\alpha^U) F}{1 - f_\alpha} + F \gamma_n^W \right. \right. \\ \left. \left. + \gamma_c^W (1 - n_c^U) \left(\frac{n_c}{n_{DT}} \right) \left(\frac{\tau_{DT}}{\tau_c} \right) \right] \right\} \frac{n_{DT}}{\tau_{DT}} \equiv H_z \frac{n_{DT}}{\tau_{DT}} ; \quad (42)$$

and the divertor-chamber-sputtered impurity flux is given by Eq. (17), which may be written

$$\Gamma_c^{\text{div}} = \left[K_c \left(\frac{n_c}{n_{DT}} \right) \left(\frac{\tau_{DT}}{\tau_z} \right) + \frac{n_c^S \gamma_c}{1 - n_c^S (\gamma_c^c + R_c^d)} \left(\gamma_{DT}^c H_{DT} + \frac{\gamma_\alpha K_\alpha F}{1 - f_\alpha} + \gamma_z^c H_z \right) \right] \frac{n_{DT}}{\tau_{DT}} , \quad (43)$$

where

$$K_c \equiv \frac{\left(n_c^U + n_c^S R_c^W \right) (1 - n_c^U)}{1 - n_c^S (\gamma_c^c + R_c^d)} . \quad (44)$$

These expressions for the relative impurity concentrations, Eqs. (30) through (32), the particle of fluxes to the wall, Eqs. (39) and (40), the particle fluxes to the divertor, Eqs. (35) and (41) through (43), and the required external source, Eq. (27), provide insight into the importance of the various factors which describe the plasma-wall-divertor interaction. These expressions depend upon the plasma parameters only through the ratio of confinement times, the ratio of the fusion-to-loss ratio (F) for D-T ions, the charge-exchange probability (A_{cx}) and, in the case of the particle fluxes, through the D-T ion loss rate (n_{DT}/τ_{DT}). An immediate consequence of these expressions is that steady-state solutions exist only if $D > 0$ and $f_\alpha < 1$.

In order to obtain a better insight into the physical content of these equations, it is illuminating to consider some limiting cases.

1. *No Backflow from Divertor* $(\gamma_c = R_x^d = 0)$

The conditions for the existence of steady-state solutions are

$$(1 - \eta_z^S)(1 - \eta_z^U)(R_z^W + \gamma_z^W) < 1 \quad (45a)$$

and

$$(1 - \eta_\alpha^S)(1 - \eta_\alpha^U)R_\alpha^W < 1, \quad (45b)$$

and the steady-state relative concentrations are

$$\frac{n_\alpha}{n_{DT}} = \left(\frac{\tau_\alpha}{\tau_{DT}} \right) \frac{F}{1 - (1 - \eta_\alpha^S)(1 - \eta_\alpha^U)R_\alpha^W}, \quad (46)$$

$$\begin{aligned} \frac{n_z}{n_{DT}} = & \left(\frac{\tau_z}{\tau_{DT}} \right) \frac{1 - \eta_z^S}{1 - (1 - \eta_z^S)(1 - \eta_z^U)(R_z^W + \gamma_z^W)} \\ & \times \left[\frac{\gamma_{DT}^W}{\gamma_{DT}^W} + \frac{\gamma_\alpha^W(1 - \eta_\alpha^U)F}{1 - (1 - \eta_\alpha^U)(1 - \eta_\alpha^S)R_\alpha^W} + \gamma_{nF}^W \right], \end{aligned} \quad (47)$$

and, of course

$$\frac{n_c}{n_{DT}} = 0. \quad (48)$$

2. *100% Efficient Unload Divertor* $(\eta^U = 1)$

The conditions for the existence of a steady-state solution are

$$R_z^d < 1, \quad (49a)$$

$$\gamma_c \gamma_c^c + R_c^d < 1, \quad (49b)$$

and

$$R_\alpha^d < 1, \quad (49c)$$

and the steady-state relative particle concentrations are

$$\frac{n_\alpha}{n_{DT}} = \left(\frac{\tau_\alpha}{\tau_{DT}} \right) \frac{F}{1 - \left[\left(1 - \eta_\alpha^S \right) R_\alpha^d / \left(1 - \eta_\alpha^S R_\alpha^d \right) \right]}, \quad (50)$$

$$\frac{n_z}{n_{DT}} = \left(\frac{\tau_z}{\tau_{DT}} \right) \frac{\left(1 - \eta_z^S \right)}{\left(1 - R_z^d \right)} \left(\overline{\gamma_{DT}^W} G + \gamma_n^W F \right), \quad (51)$$

$$\begin{aligned} \frac{n_c}{n_{DT}} = & \left(\frac{\tau_c}{\tau_{DT}} \right) \frac{\left(1 - \eta_c^S \right) \gamma_c}{\left[1 - \left(\gamma_c \gamma_c^c + R_c^d \right) \right]} \left\{ \frac{\left[\left(1 - \eta_z^S \right) + \eta_z^S \left(1 - R_z^d \right) \right] \gamma_z \left[\overline{\gamma_{DT}^W} G + \gamma_n^W F \right]}{\left(1 - R_z^d \right) \left(1 - \eta_z^S R_z^d \right)} \right. \\ & \left. + \left\{ \gamma_{DT}^c H_{DT} + \frac{\gamma_\alpha^c F}{1 - R_\alpha^d} \right\} \right\}. \end{aligned} \quad (52)$$

In this case, the concentration of wall-sputtered impurities (n_z) is due to neutron and charge-exchange neutral sputtering, as may be seen from Eq. (51) and Eq. (38) with $\eta_x^U = 1$.

3. 100% Efficient Shielding Divertor ($\eta^S = 1$)

The conditions for the existence of a steady-state solution are the same as those given by Eqs. (49). The relative particle concentrations are

$$\frac{n_\alpha}{n_{DT}} = \left(\frac{\tau_\alpha}{\tau_{DT}} \right) F, \quad (53)$$

and

$$\frac{n_z}{n_{DT}} = \frac{n_c}{n_{DT}} = 0 . \quad (54)$$

4. *No Divertor* $\left(\eta^U = \eta^S = R^d = \gamma_c = 0 \right)$

The conditions for the existence of a steady-state solution are

$$R_z^W + \gamma_z^W < 1 , \quad (55a)$$

and

$$R_\alpha^W < 1 , \quad (55b)$$

and the steady-state relative particle concentrations are

$$\frac{n_\alpha}{n_{DT}} = \left(\frac{\tau_\alpha}{\tau_{DT}} \right) \cdot \frac{F}{1 - R_\alpha^W} , \quad (56)$$

and

$$\frac{n_z}{n_{DT}} = \left(\frac{\tau_z}{\tau_{DT}} \right) \frac{1}{1 - (R_z^W + \gamma_z^W)} \left(\frac{\gamma_{DT}^W}{\gamma_{DT}^W} + \frac{\gamma_\alpha^W}{1 - R_\alpha^W} + \gamma_n^W \right) . \quad (57)$$

II. SURFACE PHENOMENA

The first-wall surfaces are expected to be a major source of plasma contamination in tokamak fusion reactors. In order to evaluate the extent of this contamination, a surface phenomena model has been developed that provides quantitative source terms for impurities emanating from the first wall. Results from the surface phenomena model are integrated into the plasma-wall interaction model, which is used to assess the effects of the wall impurities on plasma performance under conditions of interest.

The surface phenomena model includes the following interactions with candidate first-wall materials: (1) physical sputtering by ions and neutrals; (2) sputtering by 14-MeV neutrons; (3) chemical sputtering by hydrogen ions and neutrals; (4) reflection of plasma particles that strike the wall; and (5) generation of additional impurity sources in the wall by transmutation reactions. The dominant feature of the physical sputtering model relates to the energy dependence of the yield. Chemical sputtering is analyzed for the case of a carbon (graphite) wall, and effects on carbides are deduced. The particle reflection coefficients include both elastic backscattering and re-emission of injected particles. The release of transmutation products, e.g., helium generated in relatively thick low-Z liners, is considered where applicable. Contributions produced by electron and photon interactions and the "blistering" phenomenon have not been quantitatively assessed in the present investigation. The first-wall materials considered include transition metal structural materials as well as candidate low-Z materials such as beryllium, boron, carbon and selected compounds, e.g., oxides, nitrides, and carbides.

A. Physical Sputtering

Physical sputtering of first-wall materials by high-energy plasma particles is expected to be a major source of plasma contamination in fusion power reactors. As a result, the achievement of satisfactory plasma performance will be dependent, to a large extent, on the proper selection of the first-wall material. However, selection of the appropriate first-wall material is hindered by a lack of data for the physical sputter yields of potential first-wall materials and by uncertainties in the energies of particles incident on the first wall. Sputter yield data are particularly sparse for candidate low Z materials and the energy dependence of the yields has been experimentally determined only for a few materials. Even for the best-characterized materials, the experimental data are limited to only a fraction of the particles of interest, primarily H^+ , D^+ , and He^+ . Also, the majority of the data have been obtained at incident particle energies above 1 keV. Although the mean plasma temperature in a tokamak reactor will be of the order of 10 keV, the edge temperature and the mean-incident particle energy are expected to be substantially lower; probably in the range 50 to 1000 eV. A number of attempts have been made to theoretically predict physical sputter yields.⁽¹⁷⁻²¹⁾ Although comparison of theoretically predicted yields with available experimental data has met with some success for heavy ions at relatively high energies (>1 keV), the agreement with experimental data for light ions and low energies is, in general, not good.

In the present investigation, a model has been developed to provide energy-dependent physical sputter yield data for plasma particles of interest (ions and neutrals) incident on candidate first-wall materials. The expression for the physical sputter yield is based on both theoretical and experimental considerations. The general shapes of the energy-dependent sputter

yield curves are based on theoretical models while the magnitudes of the yields are derived primarily from experimental data. The semi-empirical model includes both high- and low-Z incident particles bombarding high- and low-Z wall materials. Although the model was developed primarily for single-element wall materials, it has also been applied, with minor modifications, to selected compound wall materials. The validity of the model is supported by comparison of calculated sputter-yield curves with experimental data. The exact form of the first surface, e.g., structural wall, low-Z coating, or radiatively cooled monolithic liner, has not been differentiated in the present analysis.

1. Model Development

The model incorporates existing information on physical sputtering into an analytical expression that gives the sputter yields as a function of pertinent parameters, viz., atomic and mass numbers of the incident particles and target (wall) materials, energy of the incident particles, binding energy of the target atoms, and appropriate constants. The general form of the sputter yield equation is developed primarily from modifications to Sigmund's theory,⁽¹⁷⁻¹⁹⁾ with the sputter yield in atoms per incident particle (ion or neutral) represented by

$$S = \frac{C}{U_0} \cdot f(Z,M) \cdot f(E) , \quad (58)$$

where C is a calibration constant, U_0 is the surface binding energy, $f(Z,M)$ is dependent on the atomic and mass numbers of the incident particles and target material, and $f(E)$ is the energy-dependent term. The heats of sublimation are used to represent the surface binding energies. Although calculations by Jackson⁽²²⁾ indicate that the surface binding energies of metals are generally

slightly greater (~30%) than the sublimation energies, the latter values are used in the present investigation. This difference is not large considering other uncertainties and a systematic deviation can be reflected in the magnitude of the constant C. For the case of the compound target materials, the heat of atomization as developed by Kelley^(23,24) is used as a measure of the surface binding energy.

The $f(Z,M)$ term, which is a simplified approximation of the theoretical equations developed by Sigmund,^(17,18) is given by

$$f(Z,M) = Z_1^2 Z_2^2 \cdot \frac{M_1}{M_2}, \quad (59)$$

where the subscripts 1 and 2 refer to the incident particles and target atoms, respectively, and Z and M are the atomic and mass numbers, respectively. This equation gives a better fit to the available experimental data for the conditions of interest than the more rigorous expression that is derived from theoretical considerations.

$$f^*(Z,M) = \frac{Z_1^2 Z_2^2}{\left[Z_1^{2/3} + Z_2^{2/3} \right]^{1/2}} \cdot \frac{M_1}{M_1 + M_2}. \quad (60)$$

The energy-dependent sputter yield term $f(E)$ is developed as follows: At high incident particle energies, interactions with metal target atoms are assumed to occur through coulomb repulsion of their nuclear charges, i.e., Rutherford scattering. This mechanism is considered valid for energies that significantly exceed a lower limit given by⁽²⁵⁾

$$E_B = 4E_R^2 Z_1^2 Z_2^2 \left(Z_1^{2/3} + Z_2^{2/3} \right) \cdot \frac{M_1}{M_2 E_d}, \quad (61)$$

where E_R is the Rydberg energy and E_d is the atomic displacement energy of the target lattice atoms. The theoretical curves⁽¹⁷⁻²¹⁾ based on complex calculations indicate that the sputter yield approaches a $1/E$ dependence at high energies. This behavior has also been confirmed by experimental observation for certain projectile-target systems. The present analytical expression provides for a $1/E$ sputter yield dependence at high-incident particle energies.

At low-incident particle energies, the energy dependence of the yield is reflected by the stopping power from hard-sphere (electron-cloud) type collisions, which is given by

$$S_n(E) = \frac{4M_1M_2}{(M_1 + M_2)^2} \cdot E. \quad (62)$$

Therefore, the present model provides for a direct dependence of sputter yield with incident particle energy at low energies.

At intermediate energies, screened-coulomb-type collisions are predicted for particle energies $E_A < E < E_B$, where E_A is given by⁽²⁶⁾

$$E_A = 2E_R Z_1 Z_2 \left(Z_1^{2/3} + Z_2^{2/3} \right)^{1/2} \cdot \frac{M_1 + M_2}{M_2} \quad (63)$$

and the constants are the same as in Eq. (61). In general, the yields are maximum in this energy range and are relatively insensitive to energy. Previous analyses^(6,19) have assumed a maximum in the sputter-yield curves at energies corresponding to Eq. (63); however, a correlation with available light-ion sputter yield data indicates that maxima in the yield curves occur at slightly lower energies. Attempts to arrive at an energy-dependent sputter-yield term from theoretical considerations have been based on correlations of

nuclear stopping cross sections with the dimensionless energy parameter ϵ given by⁽²⁷⁾

$$\epsilon = \frac{3.25 \times 10^{-2} M_2 E \text{ (eV)}}{Z_1 Z_2 (M_1 + M_2) (Z_1^{2/3} + Z_2^{2/3})^{1/2}}, \quad (64)$$

where the constants are the same as above. Values of $f(\epsilon)$ are given by Weisman and Sigmund⁽¹⁸⁾ only for values of $\epsilon \geq 0.1$. This corresponds to energies above 1 keV for most combinations of projectiles and target atoms of interest. Therefore, empirical adjustments have been required to obtain the desired relationships. In the present investigation, a simpler empirical expression for the energy dependence of the sputter yield has been developed. The peaks in the sputter yield curves, which are given as functions of Z_1 and Z_2 , are adjusted to energies less than E_A [Eq. (63)] to better conform with experimental data. The curves begin to deviate significantly from the $1/E$ dependence at energies below those given by E_B [Eq. (61)]. The constants that reflect the relative positions of the sputter yield peaks were determined primarily from correlations with available light-ion-sputter yield data for transition metal targets. The resultant expression for the energy-dependent term in Eq. (58) is given by

$$f(E) = \frac{E}{(E + 50 Z_1 Z_2)^2}, \quad (65)$$

where E is the incident-particle energy in electron volts.

The calibration constant C is also obtained empirically from available experimental data. In the determination of C , sputter yield data for the inert gas ions have been weighted slightly heavier than that of the hydrogen ions in order to minimize possible contributions from so-called chemical

sputtering. The possible presence of oxide films on target materials was also considered in the evaluation of experimental data.

The resultant equation obtained in the present investigation for the physical sputter yield is given by

$$S = \frac{20}{U_0} \cdot Z_1^2 Z_2^2 \cdot \frac{M_1}{M_2} \cdot \frac{E}{(E + 50 Z_1 Z_2)^2}, \quad (66)$$

where S is atoms per incident ion and the incident particle energy, E , and the surface binding energy, U_0 , are both in electron volts. The characteristics of sputter yield curves obtained from this equation include: (1) a direct energy dependence at low incident particle energies; (2) a $1/E$ dependence at high incident particle energies; (3) a peak at intermediate energies such that the sputter yield is relatively insensitive to energy for a moderate spectrum; (4) peaks for light ions ($M_1 \leq 4$) typically in the range 0.1 to 10 keV; (5) heavy ion ($M \geq 20$) sputter yields that increase directly with energy to energies of ~ 10 keV; and (6) empirically determined peak yields that generally agree with available light-ion sputter yield data.

It is assumed that no physical sputtering occurs below a threshold incident particle energy. The threshold energy is that at which the maximum energy transferable is equivalent to the surface binding energy U_0 of the target material. The magnitude as a function of mass numbers of the projectile and target is given by⁽²⁸⁾

$$E_t = \frac{(M_1 + M_2)^2}{4M_1 M_2} U_0. \quad (67)$$

Therefore, the sputter yield curves from Eq. (66) are terminated at values given by Eq. (67).

2. Application of Model to Metal Wall Materials

The energy-dependent physical sputter yields have been calculated for a number of incident particles and target materials of interest. Table I lists the materials parameters used in the sputter yield calculations for some candidate metal first-wall materials. Carbon or graphite is included in this section since it is treated similar to the monometallic first-wall materials. Incident particles of interest include hydrogenic plasma particles, typical plasma impurities, inert gas ions, and self-ions. In the present analysis, the sputter yields produced by neutrals are not differentiated from the corresponding ions. Figures 2 and 3 show the sputter yields calculated from Eq. (66) for beryllium, carbon, iron, and tungsten when bombarded with deuterium and helium ions, respectively. Beryllium has the lowest atomic number of any structural material; carbon is a low-Z material of much interest; iron is representative of stainless steel; and tungsten, although having a high atomic number, has one of the lowest sputter yields of candidate first-wall materials. These curves, although similar in shape, have somewhat flatter peaks than those developed previously.⁽⁶⁾ Also, the peaks in the present curves occur at slightly lower incident-particle energies. The threshold energies correspond to values calculated from Eq. (67). Figure 4 shows the calculated curves for the self-sputter yield of the same four wall materials. While the yields for the two lower-Z materials peak at ~ 1 keV, the self-sputter yields for the two higher-Z materials continue to increase at temperatures above the expected mean plasma temperature for tokamaks of ~ 10 keV.

Sputter yield curves calculated from the derived equations are compared with available sputter yield data to demonstrate the validity of the present model. Figures 5-9 show the results for iron (stainless steel), niobium, molybdenum, tungsten, and carbon. The data in Fig. 5 are actually a

TABLE I

Parameters for Calculation of Physical-Sputter Yields
for Metallic Wall Materials

Wall Material	Z	M	U_0 , eV
Be	4	9.0	3.4
B *	5	10.8	5.7
C *	6	12.0	7.4
Al	13	27.0	3.4
Si *	14	28.1	4.7
Ti	22	47.9	4.9
V	23	50.9	5.3
Fe	26	55.9	4.3
Nb	41	92.9	7.6
Mo	42	95.9	6.8
W	74	183.9	11.1

* Boron, carbon, and silicon are treated here with the metals.

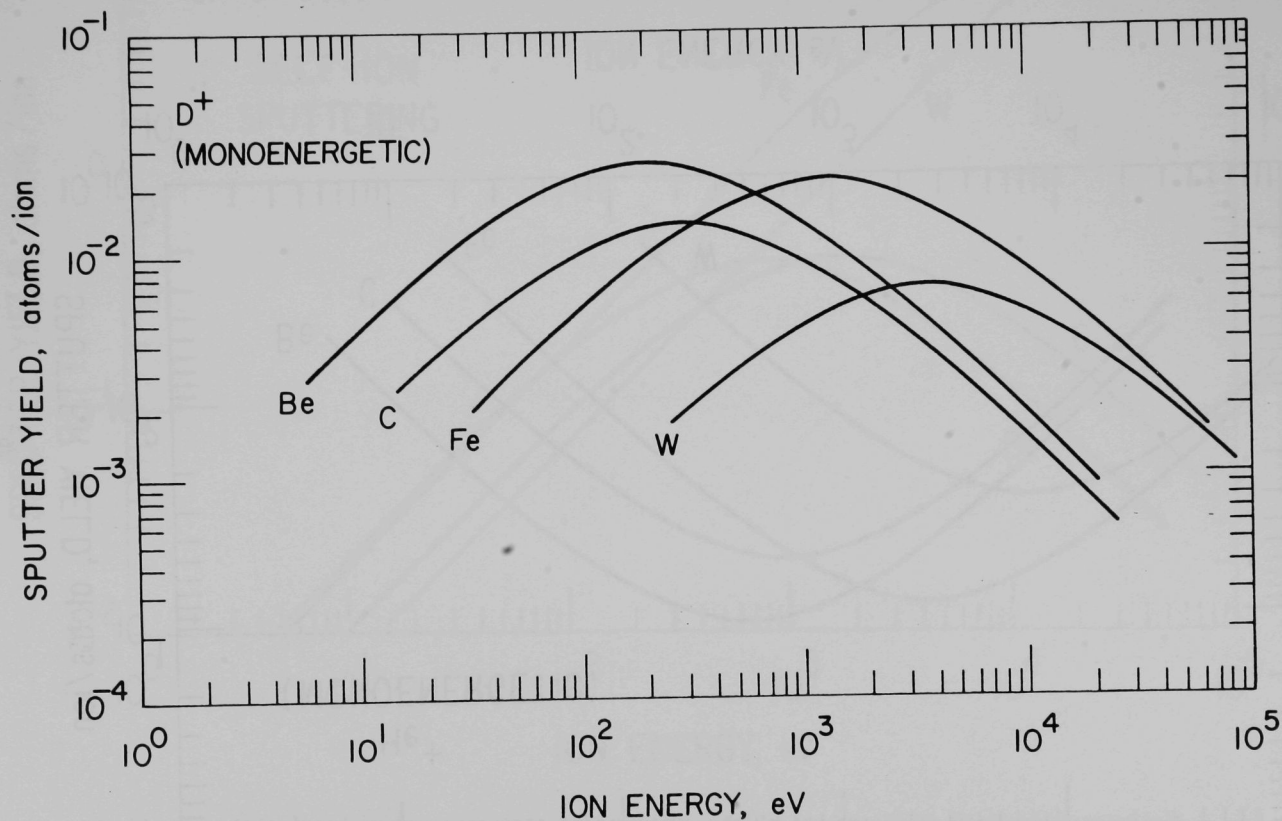


Fig. 2. Calculated energy-dependent physical sputter yields of candidate first-wall materials bombarded with monoenergetic deuterium ions.

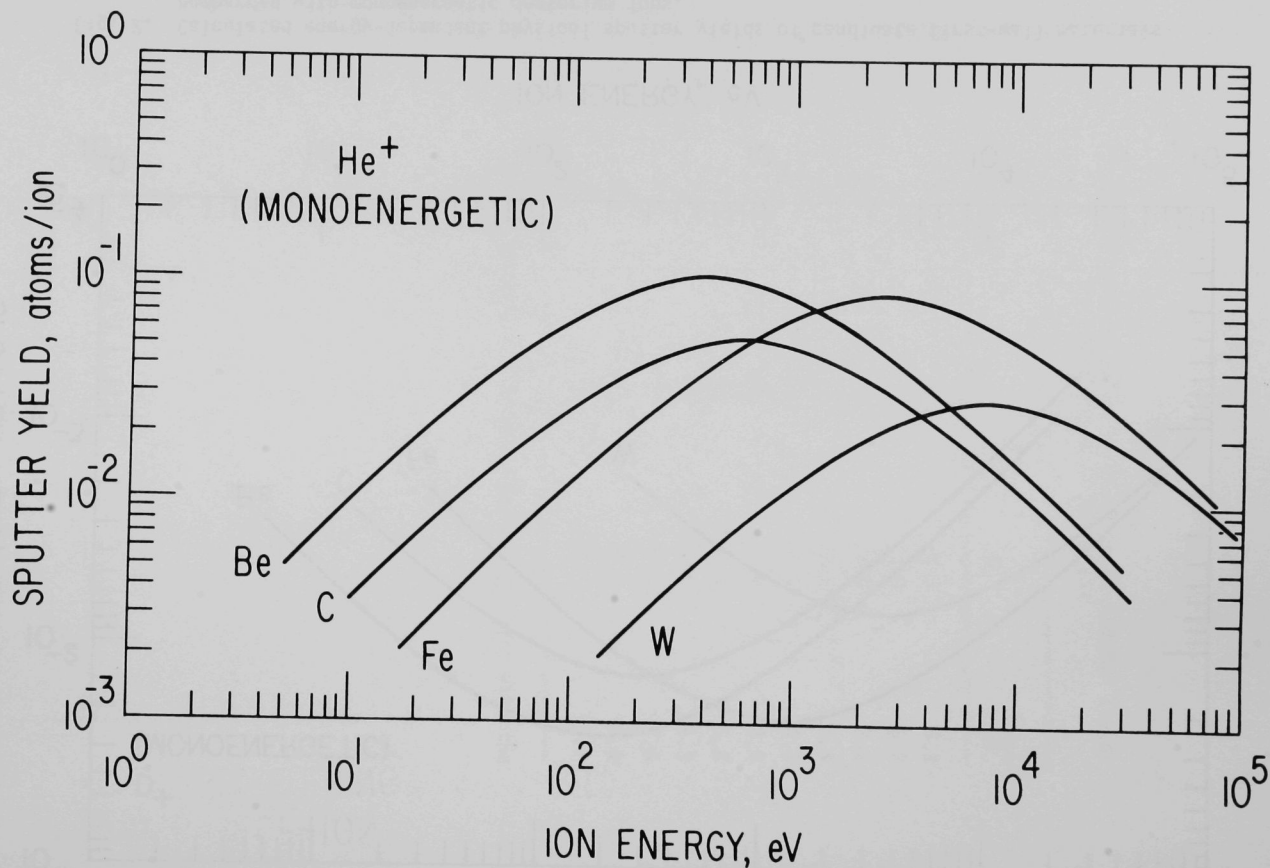


Fig. 3. Calculated energy-dependent physical sputter yields of candidate first-wall materials bombarded with monoenergetic helium ions.

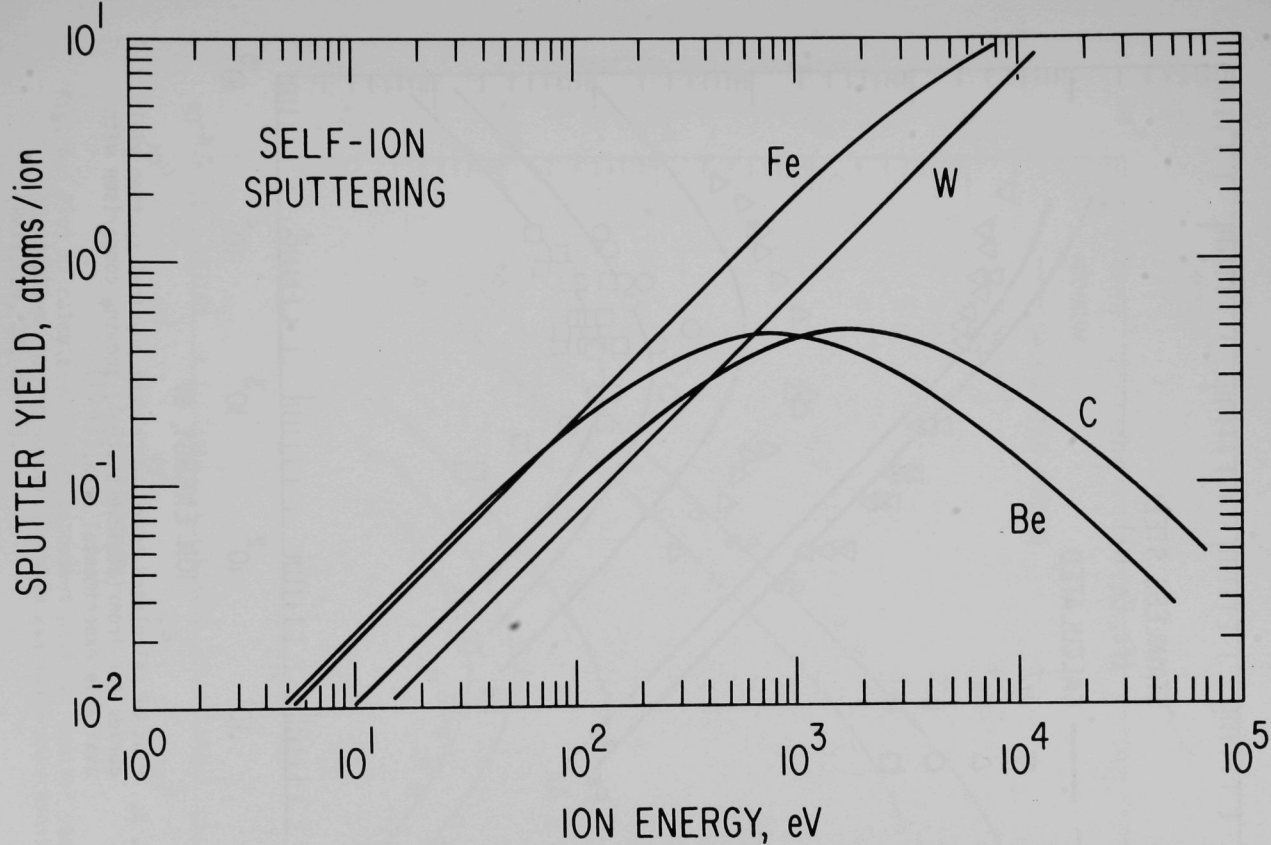


Fig. 4. Calculated energy-dependent self-sputter yields for candidate first-wall materials.

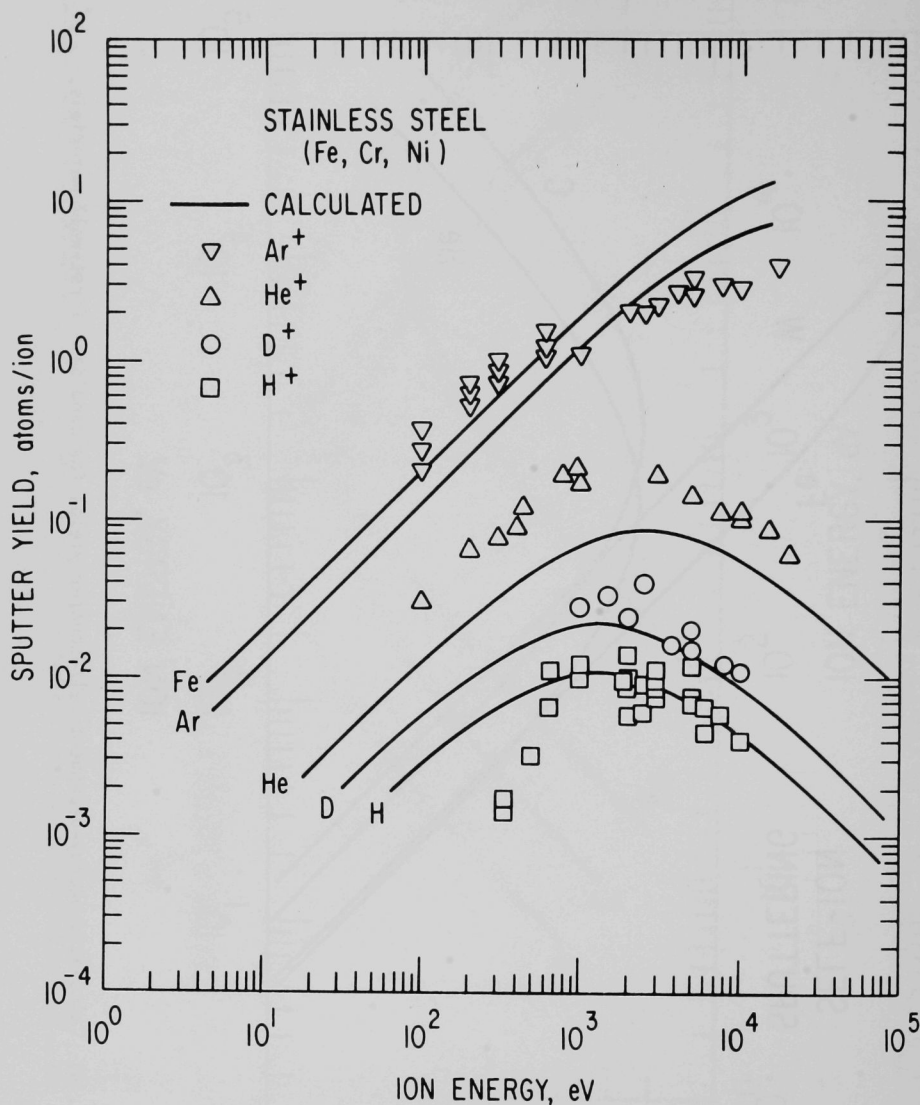


Fig. 5. Plot of calculated energy-dependent physical sputter yield curves for iron (stainless steel) showing comparison with available experimental data.⁽¹⁴⁻²¹⁾

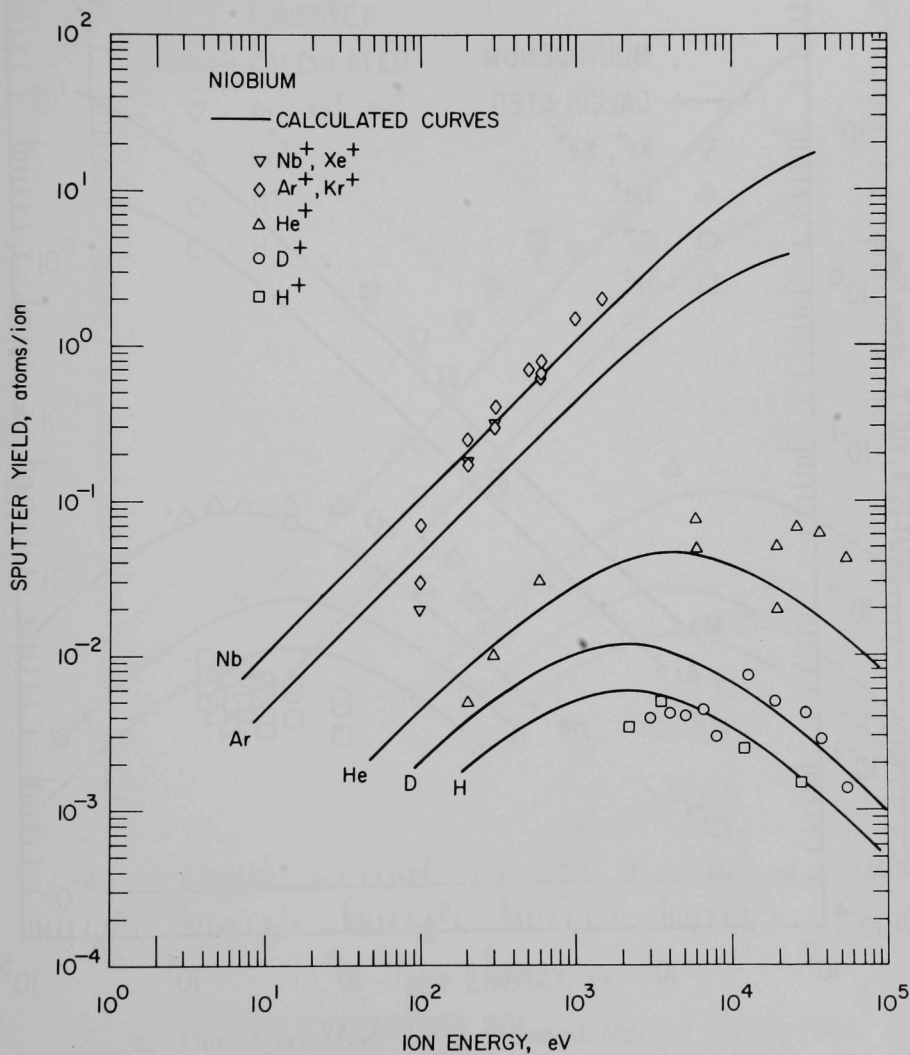


Fig. 6. Plot of calculated energy-dependent physical sputter yield curves for niobium showing comparison with available experimental data (Refs. 29, 32, 37-41).

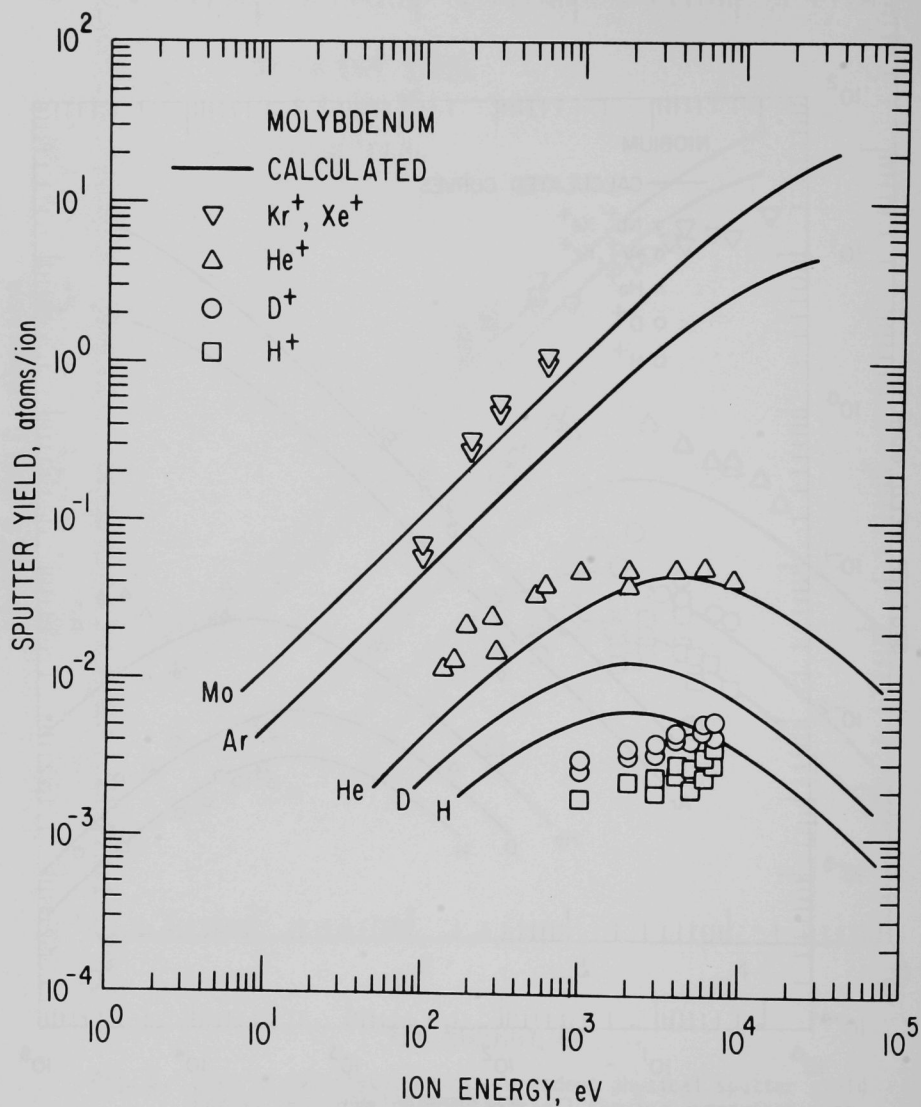


Fig. 7. Plot of calculated energy-dependent physical sputter yield curves for molybdenum showing comparison with available experimental data (Ref. 14, 26-28).

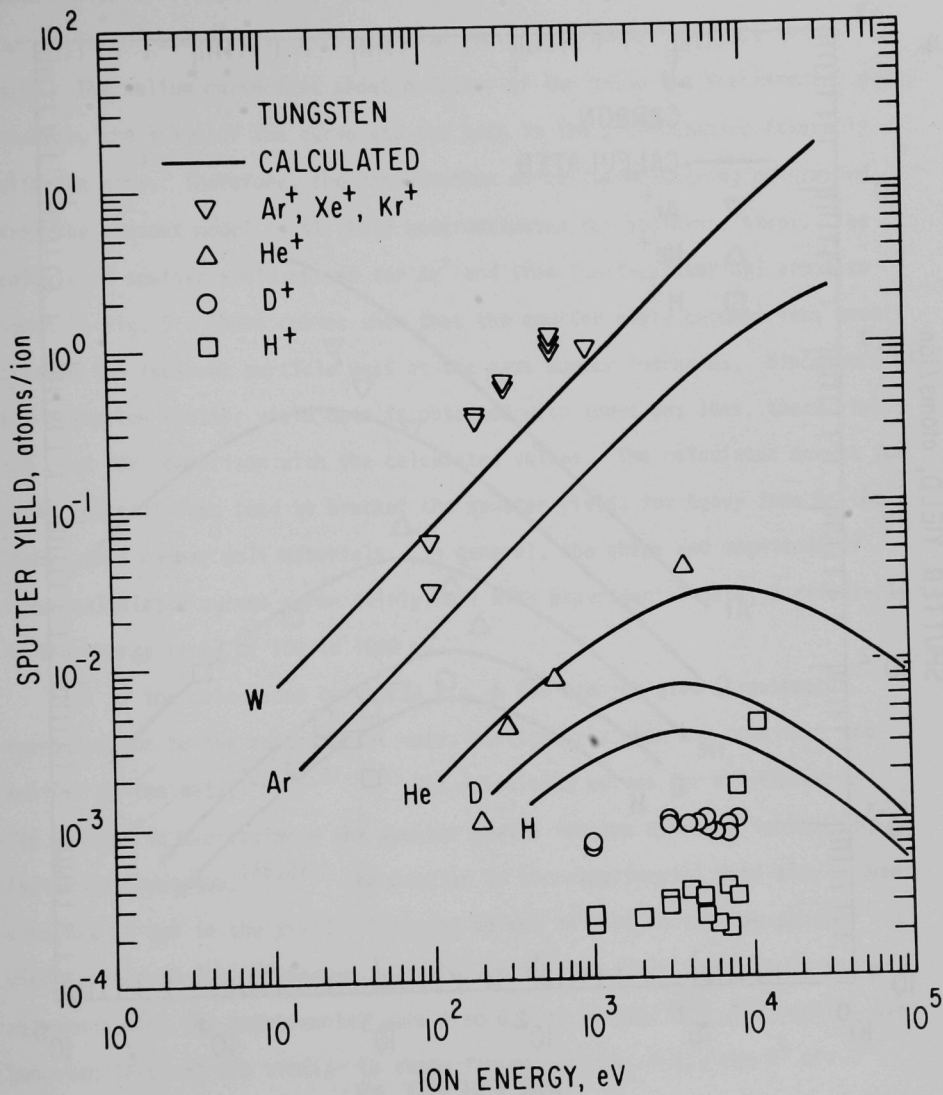


Fig. 8. Plot of calculated energy-dependent physical sputter yield curves for tungsten showing comparison with available experimental data (Ref. 14, 17, 27).

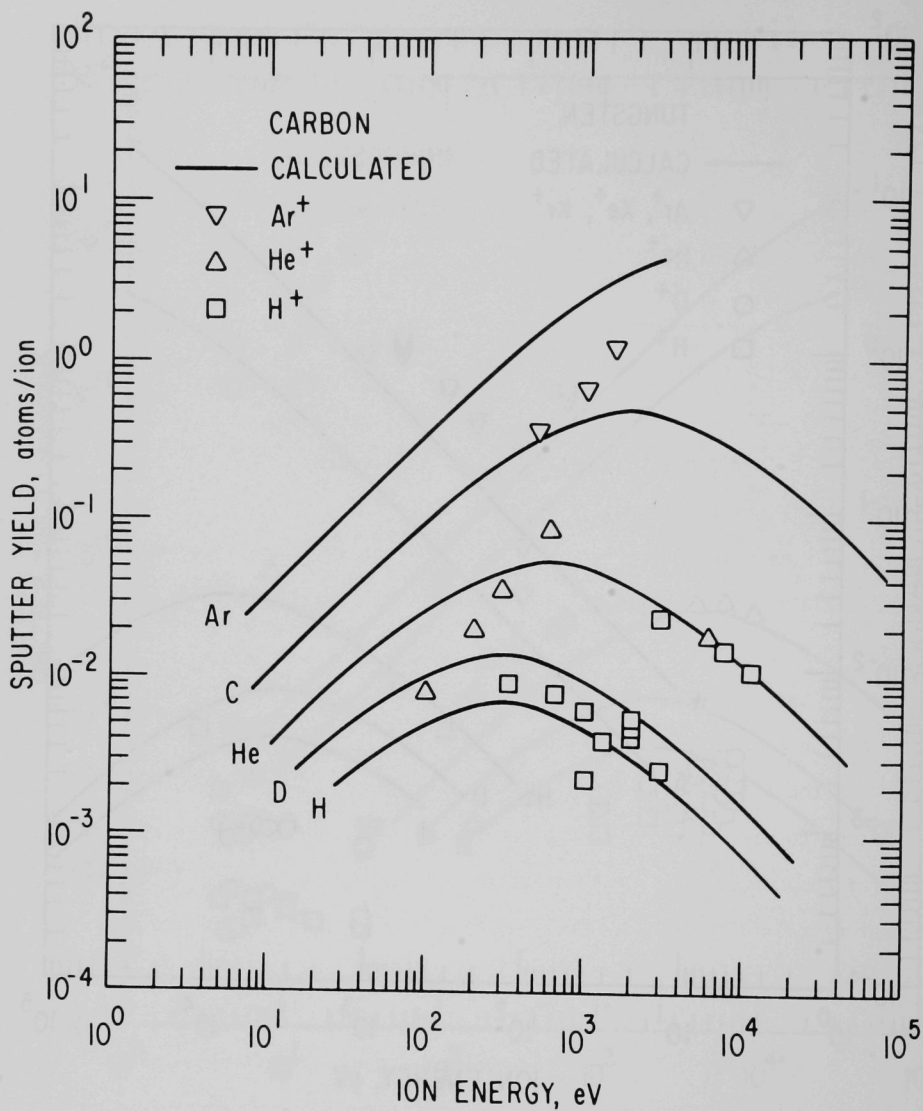


Fig. 9. Plot of calculated energy-dependent physical sputter yield curves for carbon (graphite) showing comparison with available experimental data (Ref. 14, 21, 26, 29).

combination of iron, nickel, and stainless steel data.⁽²⁹⁻³⁶⁾ The calculated curves for H^+ and D^+ give a fairly good representation of the experimental data. The helium curve lies about a factor of two below the experimental data; however, the shape of the curve and the peak in the yield compare favorably with the data. Therefore, the contribution of helium sputtering determined from the present model is slightly underestimated for stainless steel. The calculated sputter yield curves for Ar^+ and iron (self-sputtering) are also shown in Fig. 5. These curves show that the sputter yield becomes less sensitive to the incident particle mass as the mass number increases. Since much of the heavy-ion sputter yield data is obtained with inert gas ions, these yields are used for comparison with the calculated values. The calculated curves for argon and self-ions tend to bracket the sputter yields for heavy ions on the higher mass number wall materials. In general, the shape and magnitude of these calculated curves agree fairly well with experimental data, particularly in the energy range of 100 to 1000 eV.

All of the calculated curves in Fig. 6 for niobium give a reasonable approximation to the experimental data, particularly when one considers the scatter in the data.^(29,32,37-41) The calculated curves for molybdenum in Fig. 7 tend to overestimate the sputter yields for the hydrogen isotopes by a factor of about two.^(26,27) The scatter in the experimental data also exceeds a factor of two in the yield. This may be due in part to the low sputter yields observed for molybdenum. The helium sputter yield curve is in good agreement with the experimental data from 0.1 to 10 keV.⁽²⁹⁾ The results for tungsten (Fig. 8) are similar to those for molybdenum, i.e., the H^+ and D^+ curves overestimate the experimental data and the self-ion sputter yield curve gives a relatively good approximation of the heavy-ion data.^(29,32,42)

Figure 9 shows the calculated sputter yield curves for carbon (graphite).

The experimental data given for the hydrogen bombardment are for pyrolytic graphite.^(36,44) As discussed by Behrisch, et al.,⁽³⁶⁾ the data are fairly consistent for a particular type of graphite; however, considerable variation of sputter yields is observed for various types of graphite. The data shown are for low-temperature (<150°C) bombardments where the chemical sputter yield is assumed to be negligible. Much of the recent data for H^+ on carbon are in good agreement with the calculated curve. Most of the helium data agree within a factor of two with the calculated curve. Also, the calculated Ar^+ curve gives a reasonable approximation of the heavy-ion data.^(29,41)

In general, the data shown in Figs. 5-9 indicate that the model for physical sputtering [Eq. (66)] gives a reasonable approximation to the available data for the transition metals and carbon. The shapes and peaks of the calculated curves generally follow the trends of the experimental data within the uncertainty of the data. In the few cases where discrepancies occur, notably in the case of H^+ and D^+ on tungsten, adjustments in the resultant sputter behavior can be made. However, in some cases, the experimental data may also be suspect. The model is believed to provide a fairly good approximation of physical sputter yields for combinations of incident particles and metal wall materials that have not been investigated experimentally.

3. Application of Model to Compound Wall Materials

A number of compounds with low-Z atoms, e.g., BeO, BN, B_4C , and SiC, are of interest for first-wall applications. The experimental sputter yield data for this type of material are more sparse than that for the metals discussed above, and the theories for the sputtering process are less well developed. In order to obtain an evaluation of the behavior of these first-wall materials, the model described above has, with some modifications, also been applied to compounds. The binding energies used for the compounds are based on work of

Kelly, et al.,^(23,24) which was developed for oxides. As will be pointed out, the model is considered useful and will be applied only to a limited number of stable compounds. Kelly has shown that different oxides behave quite differently as far as total sputter yields are concerned. However, it has been shown that a certain class of highly stable oxides exhibit similar behavior. In the present investigation, it is assumed that selected nitrides and carbides can be treated similarly. Although other low-Z compounds such as borides and beryllides may also eventually prove to be of interest for fusion-reactor applications, these compounds are not considered further here. Table II summarizes the values that have been used for the binding energies (heats of atomization) for selected compound materials.

The atomic numbers and mass numbers of the compound wall materials are taken as the arithmetic average based on the stoichiometry of the constituent atoms. For example, the atomic number for B_4C is $0.8 Z_B + 0.2 Z_C$. The calculated values of the atomic and mass numbers for several compounds of interest are given in Table II.

Figures 10 and 11 show the calculated energy-dependent sputter-yield curves for BeO , B_4C , and SiC when bombarded by deuterium and helium, respectively. The curves for BN are similar to those for BeO . As expected from observation of the critical parameters, the yields for these compounds are similar to those shown previously for carbon or graphite. The sputter yields S for the compounds are interpreted as the total yield of all components and the yields are assumed to conform to the stoichiometry of the respective compounds. For example, the peak yield of ~ 0.015 atoms per incident deuterium ion for B_4C corresponds to a net yield of 0.012 atoms of boron and 0.003 atoms of carbon per incident deuterium ion. Although some preferential sputtering of compounds may occur when initially bombarded, the yields are expected to conform to the compound stoichiometry after a relatively short exposure time.

TABLE II

Parameters for Calculation of Physical Sputter Yields
for Compound Wall Materials

Wall Material	Z	M	U_0 , eV
BeO	6.0	12.5	6.1
B ₄ C	5.2	11.0	6.3
BN	6.0	12.4	6.1
MgO	10.0	20.2	5.1
Al ₂ O ₃	10.0	20.4	6.2
SiC	10.0	20.0	6.4
SiO ₂	10.0	20.0	6.4
TiO ₂	12.7	26.6	6.4
ZrO ₂	18.7	41.1	7.6
Nb ₂ O ₅	21.2	46.8	6.8

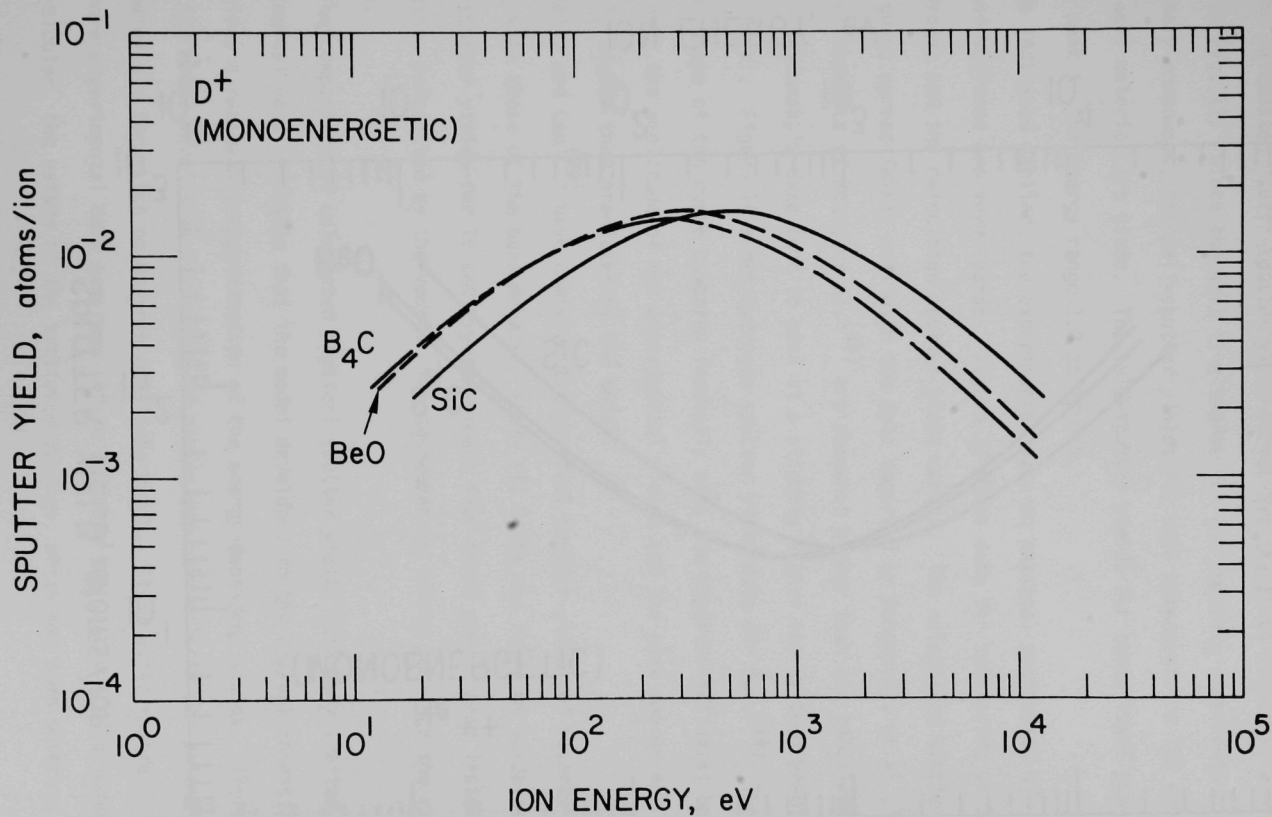


Fig. 10. Calculated energy-dependent physical sputter yields of compound first-wall materials bombarded with monoenergetic deuterium ions.

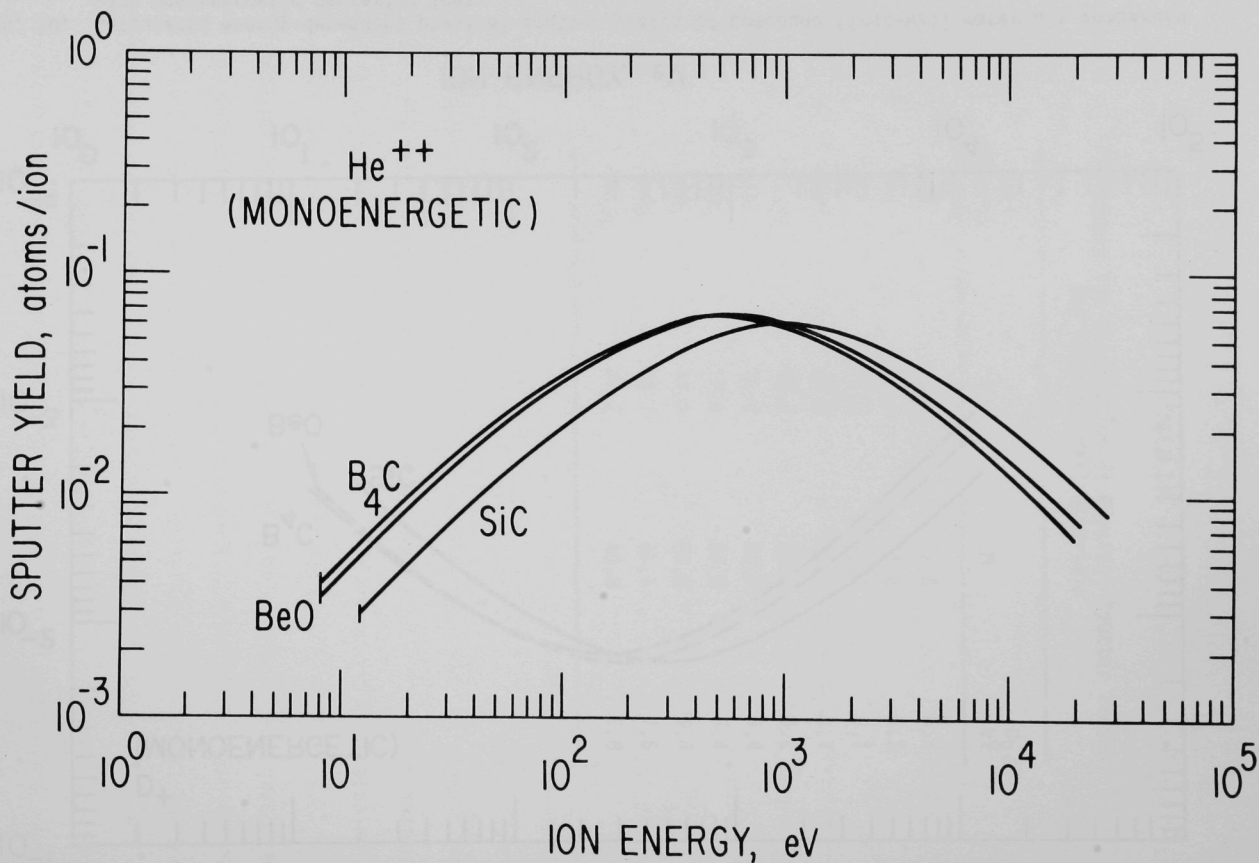


Fig. 11. Calculated energy-dependent physical sputter yields of compound first-wall materials bombarded with monoenergetic helium ions.

The calculated "self"-sputter yield curves for the three compounds are shown in Fig. 12. Since the wall is a source for two impurity components for the binary compounds, the self-sputter yields for both components on the compound wall material are given. The self-sputter yields for these low-Z compounds peak in the energy range 1.0 to 10 keV.

As indicated earlier, the experimental data on physical sputtering of compound surfaces are very sparse. Figure 13 shows data for sputtering of SiC by hydrogen and the calculated sputter yield curves. The calculated sputter yield curve agrees fairly well with the data reported by Bohdanský, et al.;⁽⁴⁴⁾ however, the data of Roth, et al.⁽⁴⁵⁾ are somewhat higher than the calculated curve. Bohdanský's data tend to peak at a slightly higher energy than predicted by the model. Figure 14 shows hydrogen sputter yield data for B₄C.⁽⁴⁴⁾ The general shape of the curve compares favorably with the experimental data; however, both the amplitude of the experimental yields and the peak energy are slightly higher than predicted by the model.

Kelly and Lam⁽²³⁾ have compared the physical sputter yields of several oxides with those of the base metals. Table III lists the ratio of oxide-to-metal sputter yields for 10 keV krypton impact from their work. Also listed are the ratios calculated by the model. The agreement is fairly good for the stable oxides.

The comparison of calculated physical sputter yields with very limited experimental data indicates that the model developed in the present investigation gives a reasonable approximation of the energy-dependent yields. Therefore, the model permits an evaluation of plasma impurity effects for potential wall materials for which no experimental data exist. It is quite apparent that more experimental data are required to validate the sputter yield model. In particular, the nature of the sputtered species, which has been observed to be

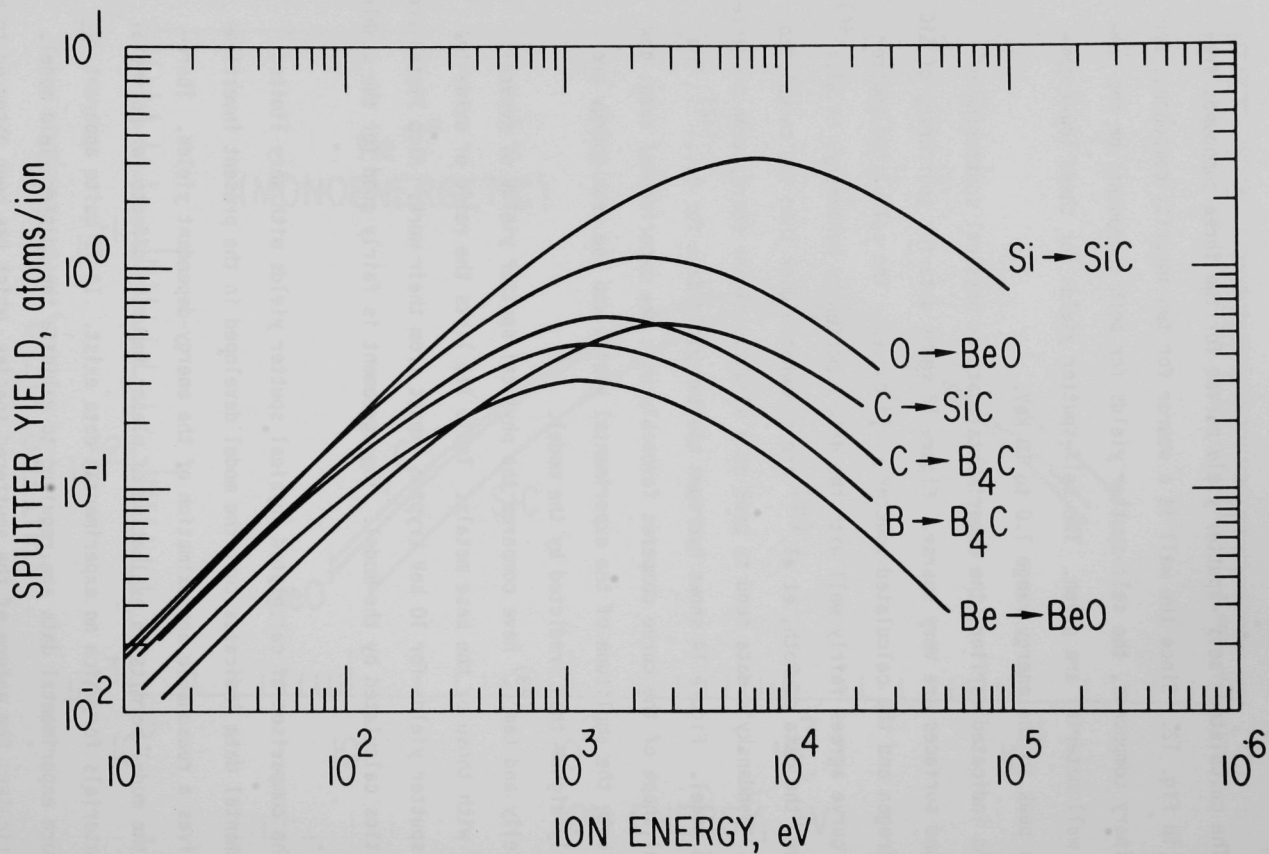


Fig. 12. Calculated energy-dependent physical sputter yields for compound first-wall materials bombarded by monoenergetic self-ions.

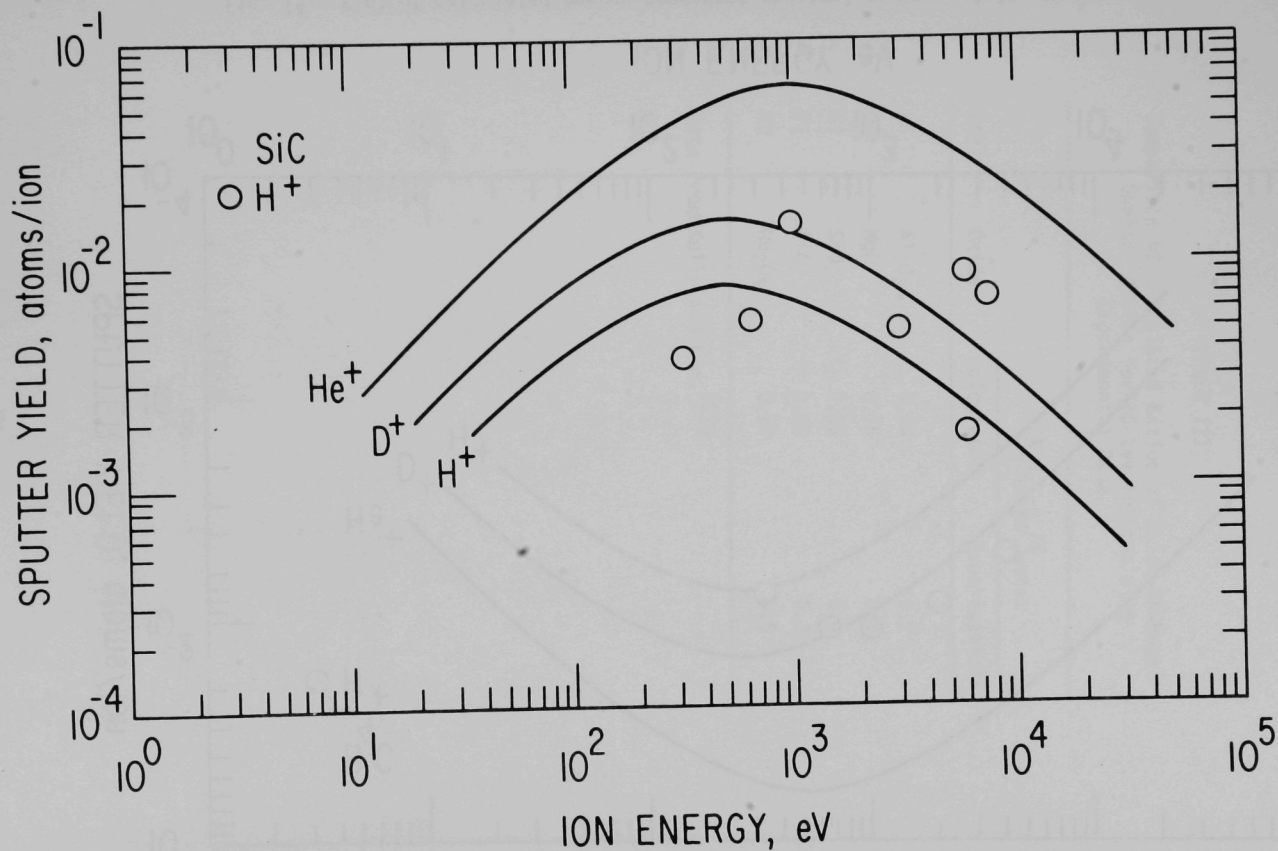


Fig. 13. Plot of calculated energy-dependent physical sputter yield curves for SiC showing comparison with available experimental data (Refs. 29, 30).

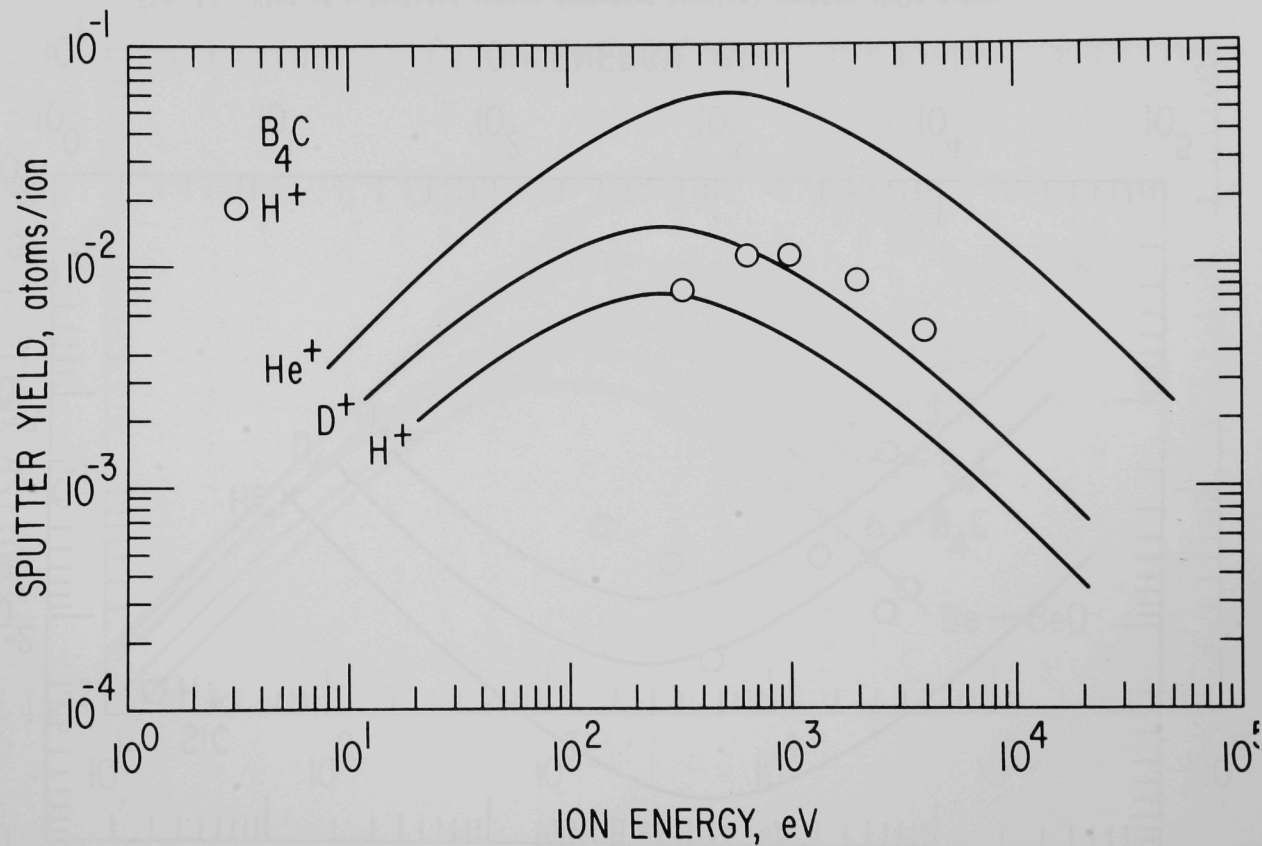


Fig. 14. Plot of calculated energy-dependent physical sputter yield curves for B_4C showing comparison with available experimental data (Ref. 29).

TABLE III

Comparison of Calculated Ratios of Oxide-to-Metal
Sputter Yields for 10-keV Krypton with
Experimental Data

Metal	Oxide	$X_m S_{\text{oxide}} / S_{\text{metal}}$	
		Calculated	Experimental*
Al	Al ₂ O ₃	0.24	0.2
Mg	MgO	0.16	0.1
Si	SiO ₂	0.55	0.6
Ti	TiO ₂	0.35	0.3
Nb	Nb ₂ O ₅	0.72	0.5

* Data from Kelly and Lam. (23)

complex in certain cases,⁽⁴⁵⁾ must be further examined for the compound wall materials. It is apparent from the estimates of the physical sputter yields that several of the low-Z compounds may be of substantial value as first-wall materials. For example, the calculated yield for beryllium oxide is less than that for beryllium, and it has been shown previously⁽⁶⁾ that beryllium is advantageous from a plasma performance viewpoint. The yields and resultant effects on plasma performance of boron-nitride and B_4C are expected to be similar to that of beryllium oxide.

4. Particle Energy Distribution

The curves and data in previous sections correspond to sputter yields produced by monoenergetic particles striking the various target/wall materials.

However, the plasma particles that are incident on the first wall of an operating fusion reactor will include a range of energies. For a tokamak, the energies of the incident particles are believed to be reasonably well described by a Maxwellian energy distribution about some mean-edge temperature. Therefore, the physical sputter yields used in the plasma-wall interaction model have been obtained by averaging the monoenergetic sputter yields with a Maxwellian distribution of incident particle energies. The average yields per incident particle for mean-edge temperatures (given by $3/2 kT$) are tabulated in Table IV for D^+ , T^+ , He^+ , and self-ions at mean-edge temperatures of 60, 200, and 1000 eV. The 200-eV edge temperature is selected as the reference case for the plasma calculations, while 60 and 1000 eV bracket the range of most interest for tokamak reactor applications. In addition to being more realistic, the Maxwellian-averaged sputter yields also tend to minimize inaccuracies produced by higher degrees of uncertainties in the sputter yields at the lower energies and effects produced by discontinuities in the yield curves at the threshold energies, i.e., $S = 0$ for $E < E_t$.

TABLE IV
Maxwellian-Averaged Physical Sputter Coefficients

Material	Mean Temp. (eV)	S_D	S_T	S_{He}	$S_{z_1}^*$	$S_{z_2}^*$	Comments
Be	60	0.0187	0.0280	0.0546	0.1571		
	200	0.0224	0.0337	0.0858	0.3142		
	1000	0.0140	0.0210	0.0742	0.3899		
B	60	0.0105	0.0160	0.0297	0.1040		
	200	0.0140	0.0210	0.0508	0.2365		
	1000	0.0096	0.0145	0.0492	0.3716		
C	60	0.0081	0.0121	0.0220	0.0851		
	200	0.0115	0.0173	0.0401	0.2113		
	1000	0.0086	0.0130	0.0427	0.3999		
Al	60	0.0108	0.0164	0.0260	0.2088		
	200	0.0204	0.0307	0.0598	0.6383		
	1000	0.0227	0.0341	0.0959	2.221		
Si	60	0.0077	0.0116	0.0182	0.1518		
	200	0.0149	0.0223	0.0429	0.4685		
	1000	0.0172	0.0259	0.0715	1.695		
Ti	60	0.0046	0.0072	0.0109	0.1482		
	200	0.0107	0.0162	0.0285	0.4753		
	1000	0.0159	0.0238	0.0595	2.086		
V	60	0.0041	0.0063	0.0096	0.1372		
	200	0.0096	0.0144	0.0251	0.4409		
	1000	0.0145	0.0217	0.0536	1.910		
Fe	60	0.0047	0.0072	0.0109	0.1695		
	200	0.0114	0.0171	0.0292	0.5478		
	1000	0.0183	0.0275	0.0660	2.438		
Nb	60	0.0012	0.0022	0.0035	0.0964		
	200	0.0044	0.0068	0.0110	0.3153		
	1000	0.0093	0.0140	0.0303	1.494		
Mo	60	0.0014	0.0025	0.0038	0.1078		
	200	0.0049	0.0075	0.0120	0.3526		
	1000	0.0103	0.0155	0.0333	1.674		
W	60	0.0001	0.0003	0.0007	0.0657		
	200	0.0013	0.0024	0.0039	0.2175		
	1000	0.0048	0.0073	0.0140	1.064		

TABLE IV (Contd.)
Maxwellian-Averaged Physical Sputter Coefficients

Material	Mean Temp. (eV)	S_D	S_T	S_{He}	$S_{Z_1}^*$	$S_{Z_2}^*$	Comments
BeO	60	0.0094	0.0143	0.0257	0.0694	0.1371	$Z_1 = \text{Be}$
	200	0.0134	0.0201	0.0467	0.1561	0.3603	$Z_2 = \text{O}$
	1000	0.0101	0.0151	0.0497	0.2402	0.7834	
B_4C	60	0.0094	0.0143	0.0257	0.0694	0.1371	$Z_1 = \text{B}$
	200	0.0129	0.0194	0.0464	0.2140	0.2565	$Z_2 = \text{C}$
	1000	0.0091	0.0136	0.0459	0.3433	0.4518	
BN	60	0.0095	0.0144	0.0259	0.0875	0.1190	$Z_1 = \text{B}$
	200	0.0135	0.0203	0.0470	0.2082	0.3040	$Z_2 = \text{N}$
	1000	0.0102	0.0152	0.0501	0.3595	0.6225	
MgO	60	0.0088	0.0132	0.0219	0.1631	0.1062	$Z_1 = \text{Mg}$
	200	0.0152	0.0227	0.0469	0.4849	0.3020	$Z_2 = \text{O}$
	1000	0.0147	0.0220	0.0656	1.522	0.8186	
Al_2O_3	60	0.0072	0.0107	0.0177	0.1500	0.0865	$Z_1 = \text{Al}$
	200	0.0123	0.0185	0.0382	0.4492	0.2460	$Z_2 = \text{O}$
	1000	0.0120	0.0180	0.0534	1.477	0.6668	
SiC	60	0.0071	0.0106	0.0175	0.1547	0.0626	$Z_1 = \text{Si}$
	200	0.0122	0.0183	0.0377	0.4662	0.1710	$Z_2 = \text{C}$
	1000	0.0118	0.0177	0.0528	1.5369	0.4112	
SiO_2	60	0.0071	0.0106	0.0175	0.1547	0.0855	$Z_1 = \text{Si}$
	200	0.0122	0.0183	0.0377	0.4662	0.2430	$Z_2 = \text{O}$
	1000	0.0118	0.0177	0.0528	1.5369	0.6589	
TiO_2	60	0.0057	0.0087	0.0138	0.2025	0.0652	$Z_1 = \text{Ti}$
	200	0.0108	0.0163	0.0319	0.6370	0.1908	$Z_2 = \text{O}$
	1000	0.0119	0.0179	0.0505	2.494	0.5657	
ZrO_2	60	0.0032	0.0052	0.0079	0.2130	0.0362	$Z_1 = \text{Zr}$
	200	0.0074	0.0112	0.0202	0.6897	0.1097	$Z_2 = \text{O}$
	1000	0.0101	0.0151	0.0391	3.099	0.3688	
Nb_2O_5	60	0.0032	0.0051	0.0079	0.2132	0.0357	$Z_1 = \text{Nb}$
	200	0.0077	0.0117	0.0207	0.6920	0.1092	$Z_2 = \text{O}$
	1000	0.0113	0.0169	0.0426	3.150	0.3803	

*Self-sputter coefficients.

B. Neutron Sputtering

Considerable effort has been expended during recent years on the investigation of 14-MeV neutron-sputter yields and large variations in the yields have been reported for various transition metals.⁽⁴⁶⁻⁵³⁾ These differences result primarily from chunk-type deposits that have been observed by some investigators and not by others. However, recent analyses indicate that the yields for chunk-type sputtering, which are dependent on both surface roughness and degree of cold work, are considerably less than originally believed.^(47,48) The yields for chunk-type neutron sputtering are now reported to be less than 10^{-4} atoms/neutron. Less discrepancy has been reported for single atom neutron sputtering, with yields typically in the range 10^{-5} - 10^{-4} atoms/neutrons.⁽⁴⁶⁻⁵³⁾ A recent review of the literature by Harling⁽⁴⁶⁾ suggests a value of $\sim 10^{-5}$ atoms/neutron for the most reliable sputter yield data. This value is in reasonable agreement with values predicted from atomic collision theory.⁽⁵⁴⁾ For the present investigation, a conservative value of 10^{-4} atoms/neutron is used for all wall materials. Since the contribution of the neutron sputter yield ($S = 10^{-4}$) is much less (<1%) than the ion physical sputter yields for anticipated reactor conditions, the results are not very sensitive to the expected variations and uncertainties in the neutron sputter coefficients.

C. Chemical Sputtering

Chemical interaction between reactive plasma particles and first-wall materials can influence the erosion yields because of effects of compound formation on lattice displacement energies, on sputtering mechanisms, and on the nature of sputtered products. Although this so-called chemical sputtering occurs in a number of systems, it is most commonly associated with the formation of hydrocarbons upon bombardment of carbon or graphite by the hydrogenic plasma particles.^(32,42,44,45,55-59) However, the release of different species upon

bombardment of ionic compounds by hydrogen ions is also classified as chemical sputtering.^(60,61) The extent of this phenomenon varies greatly with wall temperature and with the wall materials of interest. Although the major concerns regarding chemical sputtering of candidate first-wall materials relate to graphite or carbon, relevant aspects of carbides and other compound wall materials may also be important.

1. Graphite

The chemical sputtering of graphite by energetic hydrogen ions has been the subject of a number of investigations,^(32,42,44,45,55-59) and the thermodynamics of chemical interactions between hydrogen and carbon have been well established. Figure 15 shows some erosion or sputter yield data obtained from hydrogen bombardment of graphite at temperatures to $\sim 1200^{\circ}\text{C}$. Although there are some discrepancies in the published data, the general trend is for an increase in the yield as the temperature is increased from room temperature to $\sim 400^{\circ}\text{C}$, little change in the yield from 400 - 800°C , and then a rather sharp drop in the yield above 800°C . The yields observed at 400 - 800°C are approximately a factor of ten greater than the minimum observed yields for similar ion energies. The high erosion yields in the 400 - 800°C temperature range are attributed to the formation of methane (CH_4). Several investigators have detected and measured the rate of methane (including CD_4 for deuterium) gas production rates during bombardment of graphite with hydrogen or deuterium.^(55,56,59,60,62) The reaction is directly correlated with the release of trapped hydrogen rather than an ion/surface interaction. Balooch, et al⁽⁵⁸⁾ have shown that, under thermal conditions, formation of C_2H_2 may also be expected at temperatures above 1200°C . Figure 16 shows the apparent reaction probability of hydrogen with carbon as a function of temperature. Further experimental data are required to determine the importance of this reaction with energetic ions under conditions of interest.

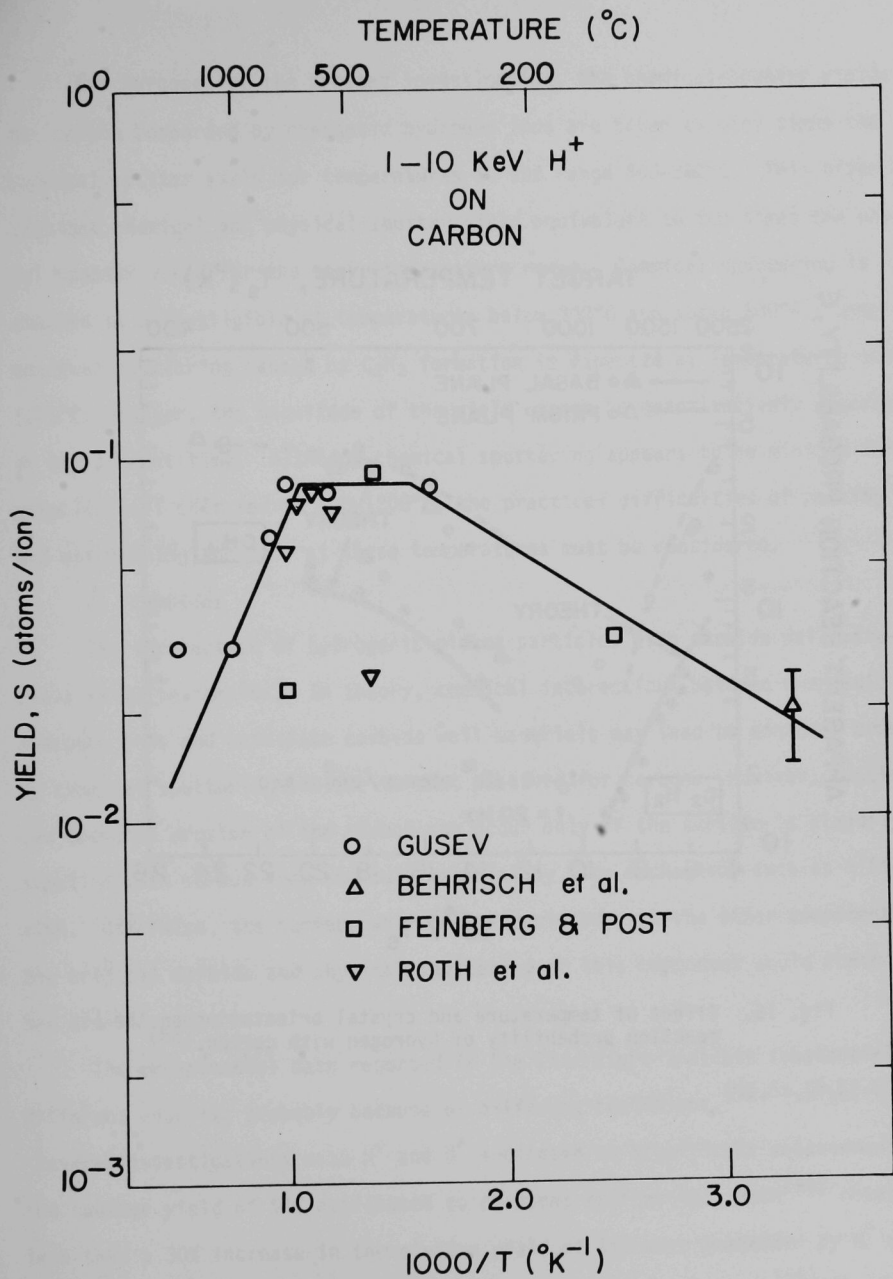


Fig. 15. Temperature dependence of sputter yields for hydrogen ions on carbon (Refs. 36, 44, 56, 57).

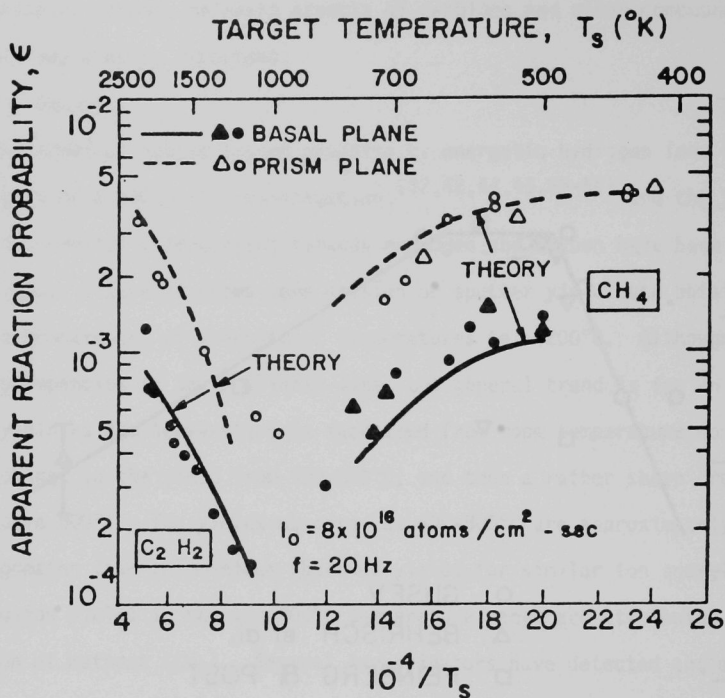


Fig. 16. Effect of temperature and crystal orientation on the reaction probability of hydrogen with carbon.⁽⁵⁸⁾

For purposes of the present investigation, the chemical-sputter yields for carbon bombarded by energetic hydrogen ions are taken as nine times the physical sputter yield for temperatures in the range 400-800°C. This gives a combined chemical and physical sputter yield equivalent to ten times the physical sputter yield for the above temperature range. Chemical sputtering is assumed to be negligible at temperatures below 300°C and above 800°C. Some chemical sputtering caused by C_2H_2 formation is expected at temperatures above 1200°C; however, the magnitude of the yield cannot be quantitatively assessed at the present time. Although chemical sputtering appears to be minimum for a graphite wall operated at 800-1200°C, the practical difficulties of heating and maintaining the wall at these temperatures must be considered.

2. Carbides

The interaction of hydrogenic plasma particles with carbide wall materials is quite complex. In theory, chemical interactions between energetic hydrogen ions and candidate carbide wall materials may lead to enhanced erosion by chemical sputtering similar to that observed for carbon. However, continuous chemical erosion of the carbon can occur only if the surface is steadily supplied with carbon from the bulk material by some mechanism, such as diffusion. Otherwise, the surface will become enriched with the other component of the original carbide and physical sputtering of this component would control the erosion rate.

The experimental data reported in the literature indicate substantially different results; probably because of differing conditions.^(45,55,59,62-65)

Several investigations with H^+ and D^+ indicated no significant enhancement of the sputter yield of SiC attributed to chemical sputtering. Roth⁽⁴⁵⁾ observed less than a 30% increase in the erosion yield of SiC when bombarded by H^+ at 535°C and 610°C compared to the room-temperature values. Veprek⁽⁵⁵⁾ found

negligible chemical erosion of SiC and B₄C by hydrogen at elevated temperatures, except for B₄C during the initial exposure. However, Wright⁽⁶³⁾ observed the formation of amorphous SiC on the surface after bombardment of crystalline SiC with 15 keV D⁺ and H⁺ ions. His analysis also indicated preferential sputtering of silicon, which resulted in a carbon-rich surface. These results tend to indicate that chemical sputtering of stable carbides by hydrogen ions is not important. However, other investigators have observed methane production when SiC and B₄C were exposed to both thermal and energetic hydrogen at elevated temperatures.^(59,62,64,65) The initial reaction rates of 20 keV D⁺ on SiC gave a methane yield with a similar temperature dependence as that obtained with carbon and a peak yield a factor of three lower. The B₄C gave a CD₄ yield nearly a factor of 10 lower than that for carbon. The peak in the yield curve occurs at ~200°C for B₄C (compared to ~500°C for SiC and carbon) and the yield drops by a factor of 10 at ~350°C. In these experiments a reduction in the methane production rate is observed with time for SiC at 500°C.

At present, it is unclear as to what extent the erosion yield of carbides is enhanced by chemical interactions with energetic hydrogenic plasma particles. It appears that some chemical interaction occurs during initial bombardment, which tends to leave the surface depleted of carbon. If this occurs, the rate limiting erosion yield may more nearly approximate that of physical sputter yields of the enriched component, e.g. silicon in the case of SiC and boron in the case of B₄C, than the physical sputter yields of the compound (see subsection A above). The importance of simultaneous bombardment by other ions, e.g., He⁺ and self-ions, which may also alter the surface morphology,⁽⁶⁶⁾ must also be investigated. It is readily apparent that additional experimental data are required before the chemical sputter yields of carbides can be quantitatively

assessed. At present, the chemical sputter yields for stable carbides of interest are believed to vary from negligible to approximately three times the physical sputter yields for the compounds. This range is substantially less than that for graphite; however, the effect on plasma performance is likely to be critical.

3. *Oxides and Other Compounds*

Hydrogen may also reduce oxides and other compounds that are of interest for first-wall materials. The stabilities of compounds in a thermal hydrogen environment are fairly well understood and can be used as a guideline for selection of appropriate materials. Compounds that are not stable in thermal hydrogen at partial pressures of interest would not likely withstand bombardment by energetic hydrogen ions. Although experimental data on chemical sputtering of compounds are very limited, Gruen^(61,67) has investigated the chemical interactions of selected oxides, with energetic hydrogen and deuterium ions. Bombardment of Al_2O_3 with 15 keV H^+ results in yields of several complex ions.

McCracken⁽⁶⁸⁾ has also observed production of complex species upon bombardment of nonmetals by hydrogen discharges. In general, these investigations have focused primarily on identification of the sputtered species and not on the magnitude of the erosion yield. As a result, it is difficult to assess the importance of chemical sputtering of oxides and similar compounds with respect to physical sputter yields and other erosion processes. For purposes of the present investigation, it is assumed that chemical sputtering is not a major erosion process for stable compounds whose components have relatively low reactivity with hydrogen. Additional data are required to identify the compounds that do not chemically react with energetic hydrogen ions and confirm the validity of this assumption.

4. Metals

Certain structural metals are known to chemically react with hydrogen to form stable hydrides. Titanium and zirconium alloys are known to be particularly strong hydride formers at relatively low hydrogen partial pressures (<1 torr at 300°C). As a result, bombardment of metal surfaces with reactive ions, e.g., H^+ , D^+ , and O^+ , may result in chemical interactions which could affect erosion yields. Gruen^(60,69) has attributed observed variations in the sputtered species from metal surfaces to chemical effects. These variations include the detection of molecular species coming from the wall and a rather large (up to 40%) fraction of the sputtered particles coming off as ions rather than neutrals. This observation may have important implications with respect to divertors for removal of wall-eroded impurities from the plasma region. Changes in the surface morphology resulting from compounds formed on the surface and chemical effects on trapping efficiencies of incident particles may also be important.

The relative importance of these chemical effects compared with other erosion phenomena, e.g., physical sputtering, have not been well established. For purposes of the present investigation, an enhancement of the erosion rates by chemical interaction has not been considered for the metal wall materials. It is conceivable that the experimental results used to establish the physical sputtering yields are already biased by chemical effects. The slight increase in physical sputter yields of stainless steel by H^+ at 500°C compared to those at room temperature may be an indication of chemical effects.⁽⁴³⁾ Further information is required to quantitatively assess the importance of chemical sputtering of metal for condition of interest.

D. Reflection Coefficients

A fraction of the plasma particles that strike the first wall of a fusion reactor eventually return to the plasma. The "reflection" coefficient, R , used

in the plasma-wall interaction model includes both backscattering and re-emission. The backscattered particles are the incident particles that return from the wall via elastic and inelastic collisions ($\ll 1$ s) whereas the re-emitted particles are those that have penetrated the wall at an earlier time and are subsequently released by diffusion to the surface or erosion of the wall material.

1. Light Ions

Several models have been developed and experiments conducted to assess the extent of backscattering and re-emission of light ions, primarily H^+ and He^+ , from several wall materials.^(6,14,70-80) Backscatter coefficients calculated from the theory of Weissman and Sigmund⁽⁷⁰⁾ are shown in Fig. 17 for D^+ and He^+ on beryllium and iron as a function of incident particle energy. These curves are in fairly good agreement with results reported recently by other investigators.⁽⁷⁴⁾ The backscatter coefficients for light ions typically increase with a decrease in incident ion energy. In certain cases, the values exceed 50% for ion energies in the range 100-1000 eV.

The use of the backscatter coefficients for the reflection coefficients is appropriate only for initial startup, since the concentrations of light atoms, viz., deuterium, tritium, and helium, will build up in the surface regions after relatively short periods of operation. Therefore, re-emission of the injected hydrogen isotopes and helium from the surface will occur during normal operation. Data of several investigators indicate that high percentages of light ions injected into a variety of target materials are re-emitted after fluences of the order of 10^{17} ion/cm².⁽⁷⁵⁻⁸⁰⁾ The period or incident fluence required before significant re-emission occurs varies with incident particle energy (deposition range) and target/wall material and temperature. The re-emission process is enhanced by elevated wall temperatures and generally approaches a steady state

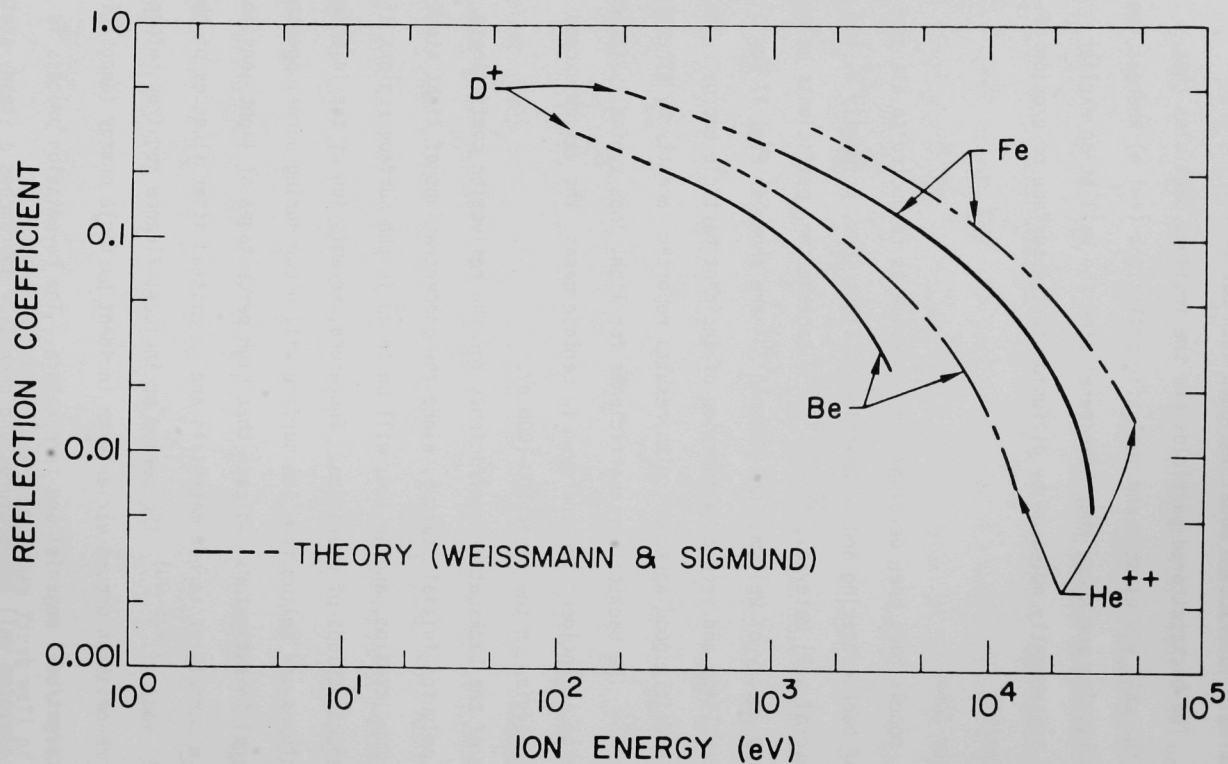


Fig. 17. Calculated reflection coefficients for deuterium and helium incident on beryllium and iron.

near 100% of the injected particles. Figure 18 shows a typical curve that illustrates the effect of temperature on the re-emission of helium from an implanted wall material.

For purposes of this work it is assumed that a steady-state condition is reached and that a combination of backscattering and re-emission results in the return of almost all of the light ions and neutrals incident on the first wall. A small allowance is made for loss of particles at ports in the wall. A second allowance in the reflection coefficient is also considered for cases where a cyclic plasma burn is encountered. A fraction of the re-emitted particles may be assumed to be emitted during the "off" cycle and pumped out of the chamber before the next burn occurs. As indicated by the temperature dependence of release rates (see Fig. 18), this effect is sensitive to the thermal response of the wall. A thermal spike that results from a plasma dump at the end of a burn cycle (see Chapt. 8, Ref. 14) may significantly enhance this end-of-cycle release and thus reduce the effective reflection coefficient. Since these effects are somewhat dependent on reactor design and burn-cycle characteristics, a range of effective reflection coefficients are proposed for the plasma performance calculations. A value of 0.98 is considered as an upper limit and a value of 0.90 is suggested for the case where significant end-of-cycle release occurs. A value of 0.95 is used as a representative average.

2. Self-Ions

Self-ions that have previously been eroded from the first wall are also expected to impact the wall. A high sticking probability is expected for energetic self-ions on a clean surface. In most cases the experimentally determined physical sputter yields by self-ions do not differentiate between sputtered and backscattered component. For the present investigation a near-zero reflection coefficient is assumed for self-ions and neutrals. This is

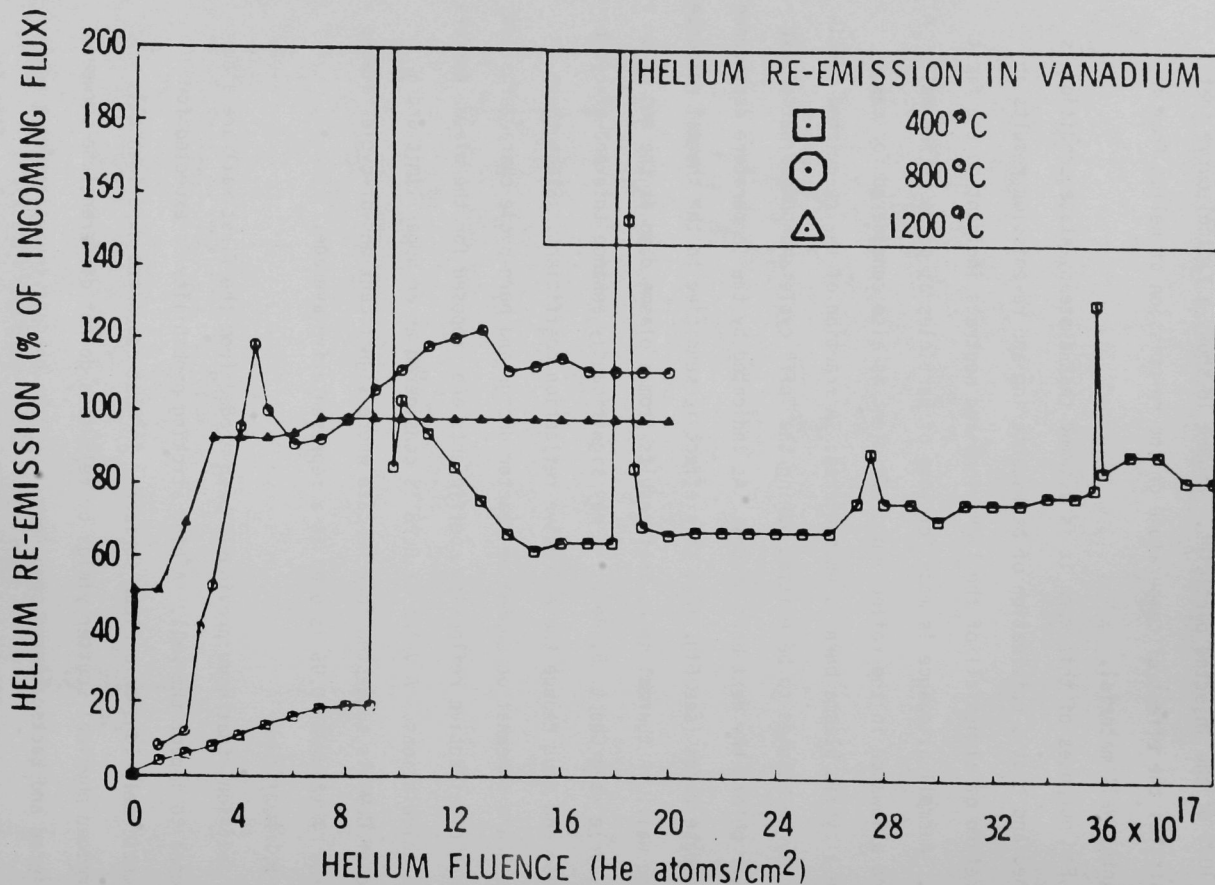


Fig. 18. Helium re-emission during 300-keV helium implantation as a function of fluence at three different implantation temperatures in vanadium.⁽⁷⁷⁾

probably a good assumption for high-energy particles which result in substantial penetration distances. Also, the relatively high-physical sputter yields for high-Z self-ions at energies in the keV range would tend to mask moderate uncertainties in the reflection coefficients. Additional information is required to validate the assumption at low-incident particle energies; however, the similarity to vapor deposition processes would tend to support this conclusion. The wall-operating temperature is expected to be an important parameter for some materials operated at temperatures where thermal vaporization is significant.

E. Transmutation Products

The high-energy neutrons generated by the D-T fusion reaction will produce large neutron fluxes in the first wall. Neutron reactions such as (n,α) and (n,p) will result in substantial amounts of light-atom transmutation products in the first-wall materials. Large amounts of helium are generated in most low-Z materials, while hydrogen is a major transmutation product in the transition metals. Table V gives the helium and hydrogen production rates of several candidate first-wall materials for an integrated neutron wall loading of 1 MW-yr/m^2 . In a practical situation it can be assumed that a fraction of these gaseous transmutation products are released to the plasma chamber. For the case of a monolithic low-Z liner, the release rate is expected to approach the production rate after an initial incubation period. An average production rate obtained from Table V for typical low-Z materials is in excess of 2000 appm/yr for a 1 MW-yr/m^2 neutron wall loading. Therefore, the helium-generation rate in a 1-cm thick low-Z liner would be $7 \times 10^{16} \alpha\text{-m}^{-2}\text{-s}^{-1}$. This value corresponds to our estimated α -particle current to the wall of $5 \times 10^{17} \alpha\text{-m}^{-2}\text{-s}^{-1}$ for a 1-MW/m^2 neutral wall loading.⁽¹⁴⁾ The helium generated in a 1-cm thick, low-Z wall is about 14% of the helium current to the wall. If a steady state is reached where the release rate is equivalent to the helium-generation rate, this amount

TABLE V

Helium and Hydrogen Production Rates
in Candidate, First-Wall Materials

Material	appm/(MW-yr/m ²)	
	Helium	Hydrogen
Beryllium	3110	51
Boron	70130 ^a	534
Carbon	2241	—
BeO	2018	72
Be ₂ C	2820	34
B ₄ C	56550 ^a	427
SAP ^b	410	790
316 SS ^c	200	540
Niobium	24	79
Molybdenum	47	95
Vanadium	57	100
Titanium	107	157

^aNatural boron (19.8% ¹⁰B and 80.2% ¹¹B) with >99% of helium produced by ¹⁰B.

^bSintered aluminum product, 5-10% Al₂O₃ in aluminum.

^cType 316 stainless steel.

of helium recycling would have a significant effect on plasma performance. Since this helium-release mechanism is similar to the re-emission of injected helium discussed in Section D, the contribution of transmuted helium can be incorporated into the reflection coefficient. For the example illustrated above, this could be equivalent to an increase in the reflection coefficient of 14%, resulting in reflection coefficients for helium of 1.04 to 1.12% instead of the 0.90 to 0.98% range recommended in Subsection D above. Of course, a thin low-Z coating would substantially reduce the importance of transmuted helium. The effects of this phenomenon on plasma performance have not been included in the present series of calculations.

F. Blistering

Considerable information has been obtained in recent years on the "blistering" phenomenon produced by injecting high-energy light ions (primarily H and He) into the surface regions of candidate fusion reactor first-wall materials. Several investigators have observed extensive blister formation and high erosion rates for metals bombarded with ~ 0.1 to 1000 keV helium under a variety of conditions.⁽⁸¹⁻⁹⁰⁾ Blister size and skin thickness have been correlated with incident particle energy and penetration depth profile. The blister erosion rates are strongly temperature-dependent for some materials and material preparation history is also important.⁽⁸¹⁻⁹⁰⁾ Erosion rates for stainless steel bombarded with 100-keV and 0.5-MeV helium increases substantially at temperatures of 400-500°C compared to room-temperature bombardment. Similar behavior has also been observed for vanadium.⁽⁸⁸⁾ Considerably different surface morphologies have been observed after bombardment at quite high temperatures. Some investigators conclude that the blistering subsides after initial formation of several blister skins.⁽⁸²⁻⁸⁵⁾ The results obtained from helium-injected nonmetals generally show a flaking or spalling rather than the typical blister formation.⁽⁹¹⁻⁹³⁾

This phenomenon is generally attributed to low ductility which limits the plastic strain needed for classical blister formation. Glasses with relatively high helium diffusivities show little or no blistering or flaking.⁽⁹²⁾ Kaminsky has also shown that blistering of sintered material is greatly suppressed compared to vacuum-cast materials.⁽⁸⁹⁻⁹⁰⁾ This reduction in blistering, which was observed for both aluminum and beryllium, is attributed primarily to modifications of the surface microstructure, viz., grain size and porosity. Reductions in the erosion rates by as much as three orders of magnitude were observed at both room and elevated temperatures. This type of data indicate that blistering can be minimized by appropriate modifications to the surface structure. The plasma spray coating process, which permits wide variations in grain size and porosity of the coatings, has been proposed as a method of obtaining desirable properties.^(6,14)

For the present model, it is assumed that the surface microstructure of the first-wall material can be properly tailored to minimize erosion rates by the "blistering" mechanism. Erosion rates comparable to those observed for sintered beryllium and aluminum ($\leq 10^{-3}$ atom/ion for 10-keV helium)^(89,90) which are much lower than the predicted physical sputter yields for helium (see Subsection A — $S \sim 10^{-1}$ atom/ion for beryllium), would be negligible. Since the mean particle energies are expected to be much lower under reactor conditions than those for which most blistering data have been accumulated, additional data at energies below 1 keV are needed to demonstrate that materials with low blister erosion yields can be fabricated. Although recent experiments have attempted to investigate the importance of particle energy spectrum as opposed to mono-energetic injection,⁽⁸¹⁾ further work is also needed in this area to more nearly simulate reactor conditions.

III. ATOMIC PROCESS IN THE PLASMA

In treating the plasma-wall-divertor problem, several atomic processes are important. The charge-exchange probability, ξ_{cx} , is needed in the plasma-wall-divertor model. The power lost by line and recombination radiation is an important factor in the plasma electron power balance when impurities are present. In this section we will examine the data base for the atomic processes important to this work and discuss the radiation models used in this survey.

A. Charge-Exchange Probability

The calculation of the charge-exchange probabilities involves knowing the charge-exchange and collisional-ionization rates for neutral deuterium and tritium as a function of plasma and neutral temperatures. In principle, charge-exchange and collisional-ionization rates for D-T with all particles present in the plasma should be used to obtain the charge-exchange probability, ξ_{cx} . In this work, only charge-exchange of D-T neutrals with D-T ions and collisional ionization of D-T neutrals by electrons and D-T ions are considered. Atomic cross-section data is readily available for these processes⁽⁹⁴⁻⁹⁷⁾ over a wide range of temperatures, and various workers have reported the Maxwellian-averaged charge-exchange and collisional ionization rates for hydrogen atoms on protons and electrons.⁽⁹⁶⁻⁹⁷⁾ In this work, D-T neutrals and ions are assumed to have mass 2.5. In using the hydrogenic data, the charge-exchange and ion collisional ionization rates can be obtained by scaling the energy scale for hydrogen by a factor of $E/2.5$. The D-T electron-collisional ionization rates are the same as those for hydrogen. The rates used are shown in Fig. 19 as a function of effective temperatures and were obtained directly from the experimental cross sections by Hermite-Gauss quadratures. The effective temperature is defined as $T = (M_2 T_1 + M_1 T_2)/(M_1 + M_2)$ for collisions

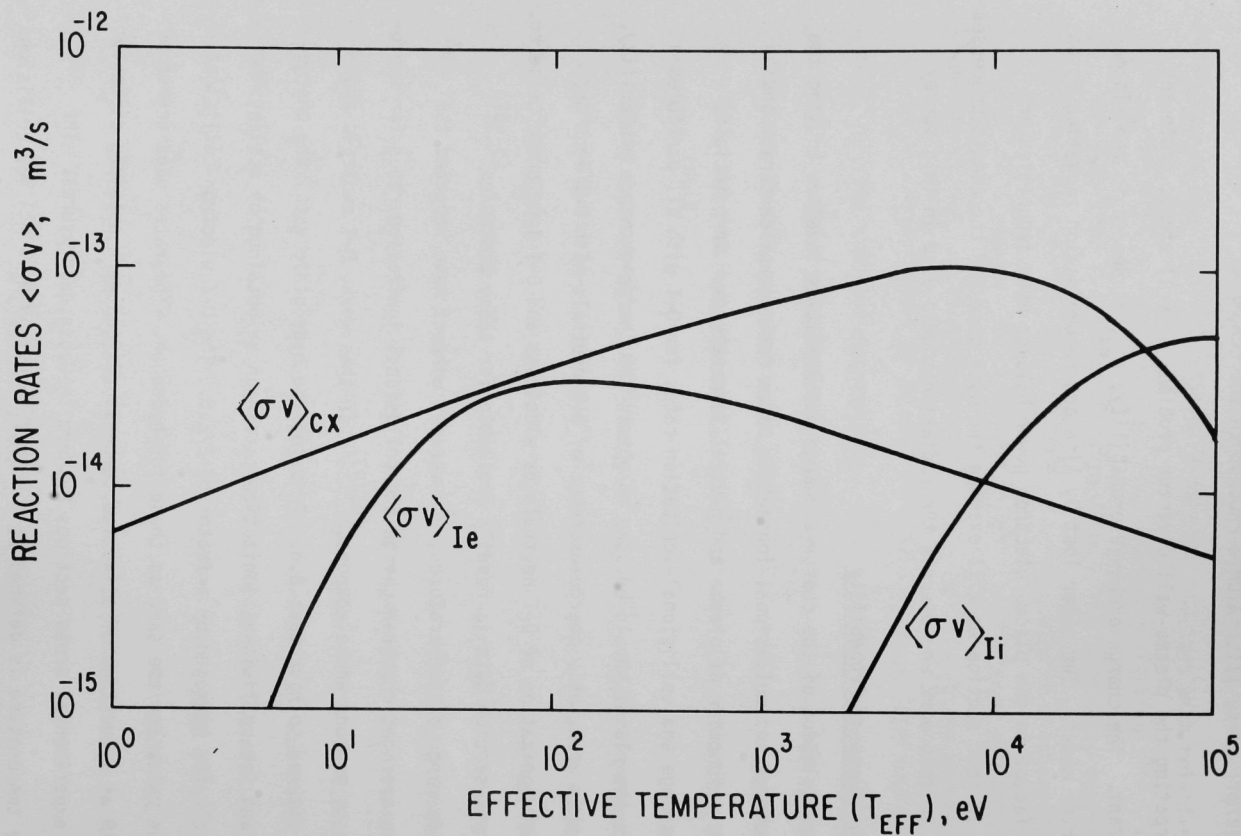


Fig. 19. Deuterium-tritium atomic process rates. Atomic charge-exchange, electron-impact ionization and ion-impact ionization rates versus effective temperature for atoms of mass 2.5 amu. $T_{\text{eff}} = (M_2 T_1 + M_1 T_2) / (M_1 + M_2)$, where M_1 and M_2 are the masses and T_1 and T_2 are the temperatures of the colliding species.

between two Maxwellian distributions of velocities characterized by temperatures T_1 and T_2 and masses M_1 and M_2 , respectively. To use Fig. 19 for charge-exchange and ion impact ionization for isotopic masses other than 2.5, one obtains the reaction rate at effective temperature T' by reading Fig. 19 at temperature T given by $T = (1.25/\mu')T'$, where μ' is the reduced mass of the new system.

B. Impurity Radiation

The radiation power loss in plasmas may be treated as being due to bremsstrahlung, resonance line, recombination, and cyclotron radiation. For temperatures of interest in this work, bremsstrahlung and cyclotron radiation play a minor role. The power lost by these processes are treated as previously described (see Appendix B, pg. 17 of Ref. 14). In treating the line and recombination radiation from medium density ($\sim 1 \times 10^{20}/\text{m}^3$) plasmas, the important elementary processes are electron-collisional excitation and ionization and radiative recombination. Collision de-excitation and three-body recombination can be ignored relative to radiative de-excitation and recombination at these densities. Also, at these densities, it is assumed that radiative decay occurs immediately upon formation of an excited state.

Thus, the elementary process data necessary to adequately treat the radiation from tokamak plasmas reduces to determining the electron-collisional excitation and ionization rates and the radiative recombination rates for all term levels of all ionized states of all atomic species present in the plasma. Such a task is a formidable one indeed and only very recently has work begun on some of the systems of interest in tokamak design.

Experimentally, it is very difficult to obtain data for highly stripped medium-to-high-Z systems in laboratory or astrophysical plasmas. However, cross sections can now be obtained from both theory and experiment with reasona-

ble accuracy for the lighter elements.⁽⁹⁸⁻¹⁰²⁾ Even for the hydrogen-like ions of the heavier elements, however, neither theory nor experiment has as yet provided complete data. Thus, the transition between the low-Z and medium-to-high Z elements remains to be bridged. For the low-Z elements, cross sections can now be determined with uncertainties to within a factor of two; while, for the intermediate-to-high-Z elements, some of the rate coefficients are likely to be an order of magnitude in error.⁽¹⁰³⁾

Table VI presents a matrix of references to work giving atomic cross section or rate data for the elements considered in this paper. One is struck by the incompleteness of this information for the heavier elements.

Since radiative decay occurs essentially instantaneously after an ion is collisionally excited by an electron, in medium density plasmas, the rate of energy loss from the plasma is determined by the rate of production of excited states. Thus, the resonance line radiation power loss is given by

$$P_L = N_e \sum_Z \sum_L N_Z E_{ZL} X_{ZL}, \quad (68)$$

where

N_e is the electron density

N_Z is the density of the Z-th ionic state of the element

E_{ZL} is the transition energy for the L-th energy level to the ground energy level of the Z-th ionic state of the element

X_{ZL} is the electron collisional excitation rate for the excitation of the L-th energy level from the ground energy level.

The power lost by radiative recombination of an electron of energy E with an ion in the Z + 1-st ionic state ground energy level to the Z-th ionic state ground energy level is given by

TABLE VI. Atomic Processes

Element	State	Electron Impact Excitation ^a	Electron Impact Ionization	Recombination Rates ^b	Comments
H	I	94,95,115 ^c ,122 ^d ,125 ^c ,132 ^c	94-97 ^c ,131 ^c	95	122 ^d -13.5 to 500 eV
He	I	95,115 ^c ,121 ^d ,124 ^c ,125 ^c ,137 ^c	95,97 ^c	95	130 ^c ,140 ^c -III
	II	95,115 ^c , ^d ,136 ^c	95 ^c	133 ^c	
Be	I		97 ^c	130 ^c	130 ^c ,140 ^c -V
	II	115 ^c , ^d			
	III	115 ^c			
	IV	115 ^c		133 ^c	
C	I	95 ^c ,115 ^c ,116 ^c	95,97 ^c ,116 ^c ,126 ^d	116 ^c	117 ^d -2000 to 2500 eV
	II	95 ^c ,114 ^c ,115 ^c	119 ^c	128 ^c	119 ^c -50 to 3000 eV
	III	95 ^c ,114 ^c ,115 ^c	117 ^d ,119 ^c		126 ^d -7.3 to 997.3 eV
	IV	95 ^c ,114 ^c ,115 ^c	117 ^d ,119 ^c		130 ^c ,140 ^c -VII
	V	95 ^c ,114 ^c ,115 ^c ,118 ^c	117 ^d ,119 ^c		
	VI	95 ^c ,114 ^c ,115 ^c	117 ^d ,119 ^c	133 ^c	
O	I	95 ^c , ^d ,115 ^c ,116 ^c ,118 ^c ,123 ^c ,134 ^d	95,97 ^c ,116 ^c ,126 ^d	116 ^c	126 ^d -8.3 to 997.3 eV
	II	95 ^c ,115 ^c ,118 ^c	95,119 ^c		130 ^c ,140 ^c -IX
	III	95 ^c ,115 ^c ,118 ^c	95,119 ^c		
	IV	114 ^c ,118 ^c	119 ^c		
	V	114 ^c ,118 ^c	119 ^c	128 ^c	
	VI	95 ^c ,114 ^c ,118 ^c ,127 ^c	119 ^c		
	VII	95 ^c ,114 ^c ,118 ^c	119 ^c		
	VIII	95 ^c ,114 ^c	119 ^c	133 ^c	
Fe	VIII-XI	115 ^c , ^d ,116 ^c ,120 ^c ,139 ^c	116 ^c	116 ^c ,141 ^c	139 ^c -10-10 ⁶ eV
	XII-XVI	95,116 ^c ,120 ^c ,139 ^c		129 ^c	120 ^c -IX-XXV 129 ^c -XV-XXV
	XVII-XXVI	115 ^c ,120 ^c ,139 ^c		129 ^c	130 ^c ,140 ^c -XXVII 139 ^c -XI,XIV-XV, XVII,XIX,XX,XXIII
Mo	I-XXXXIII	116 ^c	116 ^c	116 ^c ,130 ^c ,135 ^c	135 ^c -1 to 100 keV

^aAlso see Ref. 113.^bAlso see Ref. 142.^cTheoretical.^dExperimental.

$$\begin{aligned}
P_R &= N_e \sum_Z N_{Z+1} \langle (E_{Z+1} + E) v \sigma_R \rangle_{Z+1} \\
&= N_e \sum_Z N_{Z+1} \left[E_{Z+1} R_{Z+1} + \langle E v \sigma_R \rangle_{Z+1} \right],
\end{aligned}$$

where

E_{Z+1} is the ionization potential for formation of ionic state $Z + 1$ from state Z ;

R_{Z+1} is the recombination rate for formation of state Z from state $Z + 1$; and

$\langle E v \sigma_R \rangle_{Z+1}$ is the average over the Maxwellian distribution of the recombination cross section from state $Z + 1$ times $E v$.

Since all ionic species are assumed to be in the ground energy level, the distribution of a given element over its various ionic states is given by

$$\frac{dN_Z}{dt} = N_e \left(I_{Z-1} N_{Z-1} + R_{Z+1} N_{Z+1} - I_Z N_Z - R_Z N_Z \right), \quad (70)$$

where

I_Z is the ionization rate for ionization of state Z to state $Z + 1$

R_{Z+1} is the recombination rate for recombination of state $Z + 1$ to state Z .

The recombination rate includes dielectronic recombination, and the sum over N_Z gives the density of the element at a given point in the plasma.

If it is assumed that the characteristic time scales for the atomic processes are short compared to the other processes taking place in the plasma, then $dN_Z/dt = 0$, and a tri-diagonal system of equations results which has

the solution

$$N_{Z+1}/N_Z = I_Z/R_{Z+1} \cdot \quad (71)$$

This treatment, known as the coronal equilibrium model, has been used to calculate the radiated power loss from various elements in high-temperature plasmas.⁽¹⁰⁴⁻¹²²⁾ Since, as Table VI shows, the elementary process data is incomplete for many systems, various estimates have been used for the rate coefficients. We have chosen to compare several of these calculations for oxygen and iron-seeded D-T plasmas to determine how the calculated radiation loss from each affects the conclusions drawn from the plasma-wall-divertor calculations. The model used in this study⁽¹⁴⁾ for impurity radiation loss is compared with those of Dücks, et al.,⁽¹⁰⁴⁾ Breton, et al.,⁽¹⁰⁶⁾ and Hinnoy⁽¹⁰⁶⁾ for oxygen and with those of Breton, et al.,⁽¹⁰⁵⁾ Hinnoy,⁽¹⁰⁶⁾ and Merts, et al.⁽¹⁰⁷⁾ for iron.

Briefly, the impurity radiation model used in this study is a modification of a model due to Hopkins.⁽¹⁰⁸⁾ The bremsstrahlung, line and recombination radiation power is given by the following expressions,

$$P = 4.8 \times 10^{-43} n_e n_Z \left\{ Z^2 T_e^{1/2} + \left[(3.792 \times 10^{-2} Z^4) / T_e^{1/2} + (8.604 \times 10^{-4} Z^6) / T_e^{3/2} \right] \times (T_e / T)^2 \right\} (\text{MW/m}^3), \quad (72)$$

where we have modified Hopkin's model to go quadratically to zero when T_e is less than T_c , and where

$$T = \begin{cases} T_e & ; \quad T_e \geq T_c \\ T_c & ; \quad T_e < T_c \end{cases}$$

where

$$T_c = \left[1.033 \times 10^{-7} (Z - 3)^3 + 3.4266 \times 10^{-3} (Z - 3)^2 + 5.5574 \times 10^{-3} (Z - 3) + 0.529 \times 10^{-3} \right] \text{ (keV) .} \quad (73)$$

with T in keV and densities in particles/m³. On the other hand, Hinnov⁽¹⁰⁶⁾ gives for the power lost by line radiation,

$$P = 2 \times 10^{-38} n_e n_z \text{ (MW/m}^3\text{) .} \quad (74)$$

The radiative power losses (excluding bremsstrahlung and cyclotron processes) that would be predicted on the basis of the various models are shown in Figs. 20 and 21 for oxygen and iron, respectively, in a D-T plasma. The model used in this study underpredicts (relative to the other models), the radiation during the very early startup (≤ 50 eV) for oxygen and during the entire startup ($\leq 10^3$ eV) for iron in a D-T plasma. Thus, the difficulties, cited elsewhere in this work, encountered in starting up a plasma with impurities present are probably understated. The predicted radiative power loss in the operating regime (≥ 8 keV) is comparable for the model used in this study with that of Merts⁽¹⁰⁷⁾ and Breton,⁽¹⁰⁵⁾ all of which are lower than the prediction based on the Hinnov model. Consequently, tolerable impurity levels computed on the basis of the model of this study and those of Merts and Breton should be comparable and somewhat greater than levels computed on the basis of the Hinnov model.

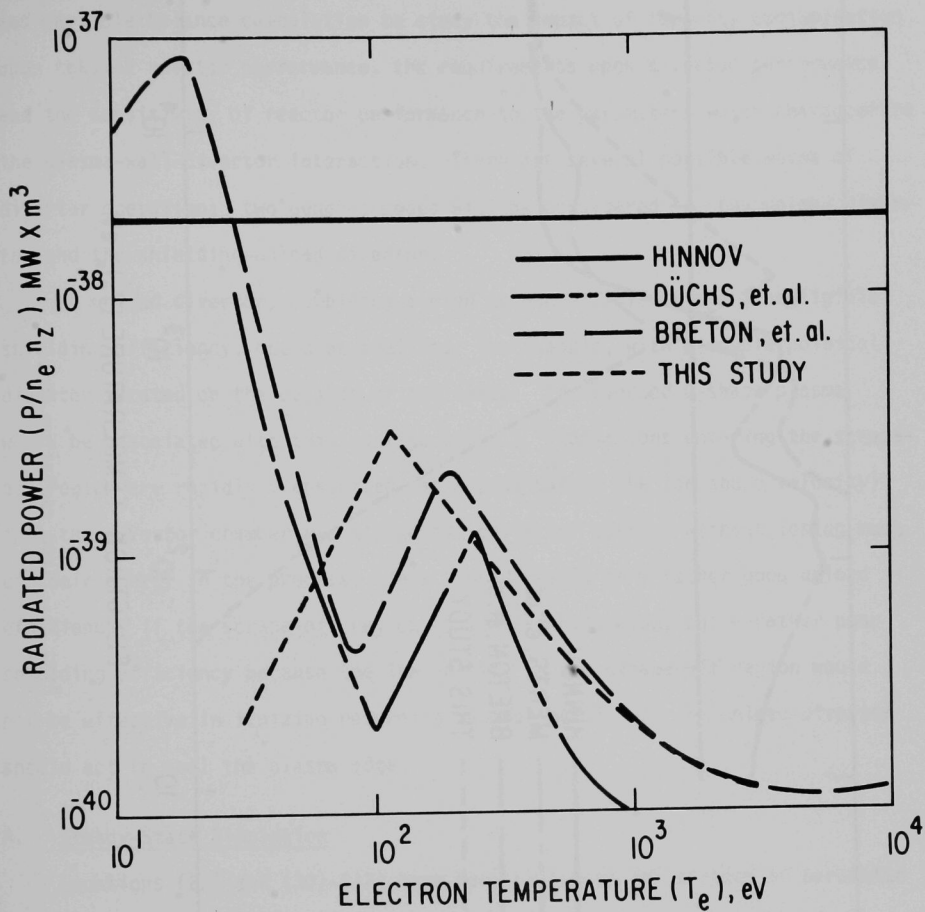


Fig. 20. Oxygen radiation loss.

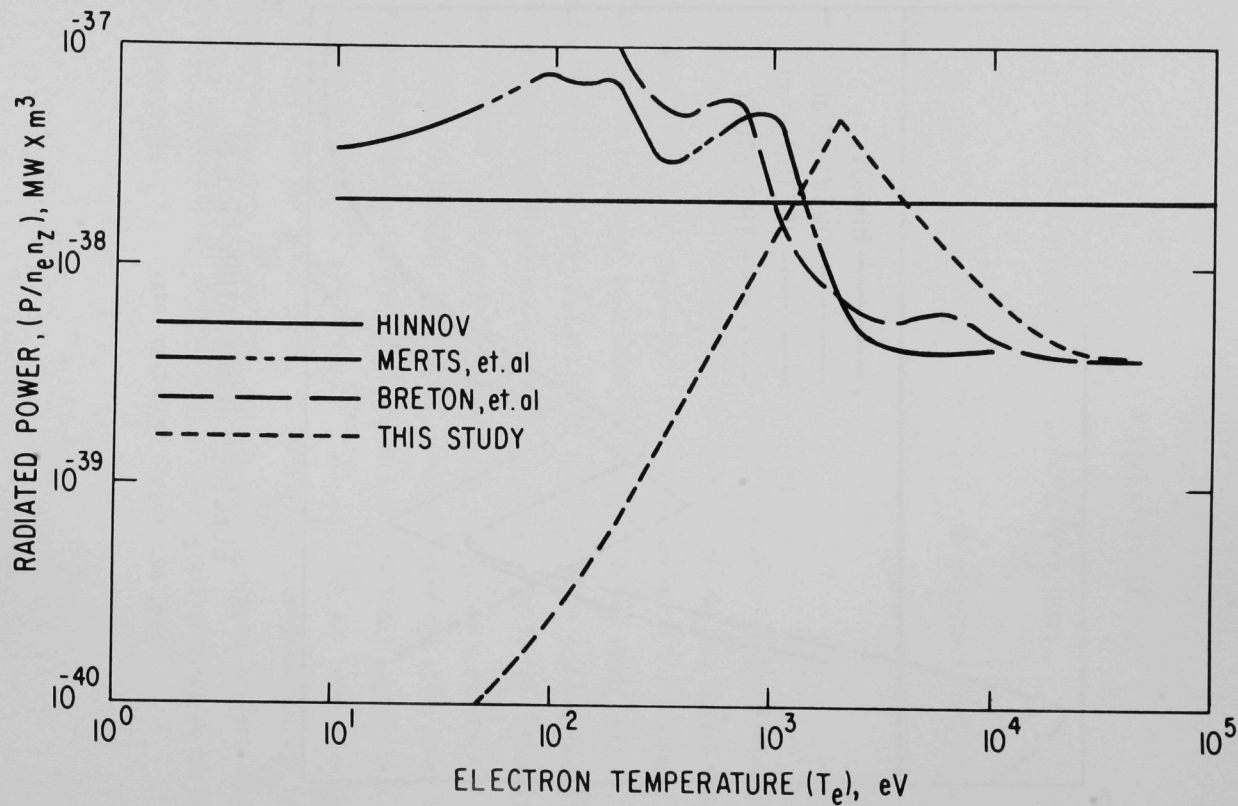


Fig. 21. Iron radiation loss.

IV. IMPURITY CONTROL AND REACTOR PERFORMANCE

The results of the previous sections can be combined with a plasma power and particle balance calculation to study the impact of impurity contamination upon tokamak reactor performance, the requirements upon divertor performance, and the sensitivity of reactor performance to the parameters which characterize the plasma-wall-divertor interaction. There are several possible modes of divertor operation: two generic modes will be considered — the unload divertor and the shielding-unload divertor.

An unload divertor, combining a high unload efficiency and a negligible shielding efficiency, could be realized, for example, with a double poloidal divertor located on the outside of the torus. (A reversed D-shape plasma would be associated with this configuration.) Plasma ions entering the scrape-off region are rapidly transported (at approximately the ion sound velocity) into the divertor chamber and strike the collector surface without losing much of their energy in the process. This should result in a rather good unload efficiency, if the scrape-off region is sufficiently wide, but a rather poor shielding efficiency because the low density in the scrape-off region would not be effective in ionizing returning neutral particles. An unload divertor should act to cool the plasma edge.

A. Steady-State Simulation

Equations (27) and (30)-(32) have been evaluated for a range of parameter values characteristic of an unload divertor. The results are plotted in Figs. 22a-22d. Note from Eq. (27) that the external source which is required to maintain the plasma density is proportional to the ion loss rate, so that it is possible to display a normalized source, $S_{DT}^{ext} \div n_{DT}/\tau_{DT}$, which is independent of the particle loss rate. Similarly, the relative impurity concentrations

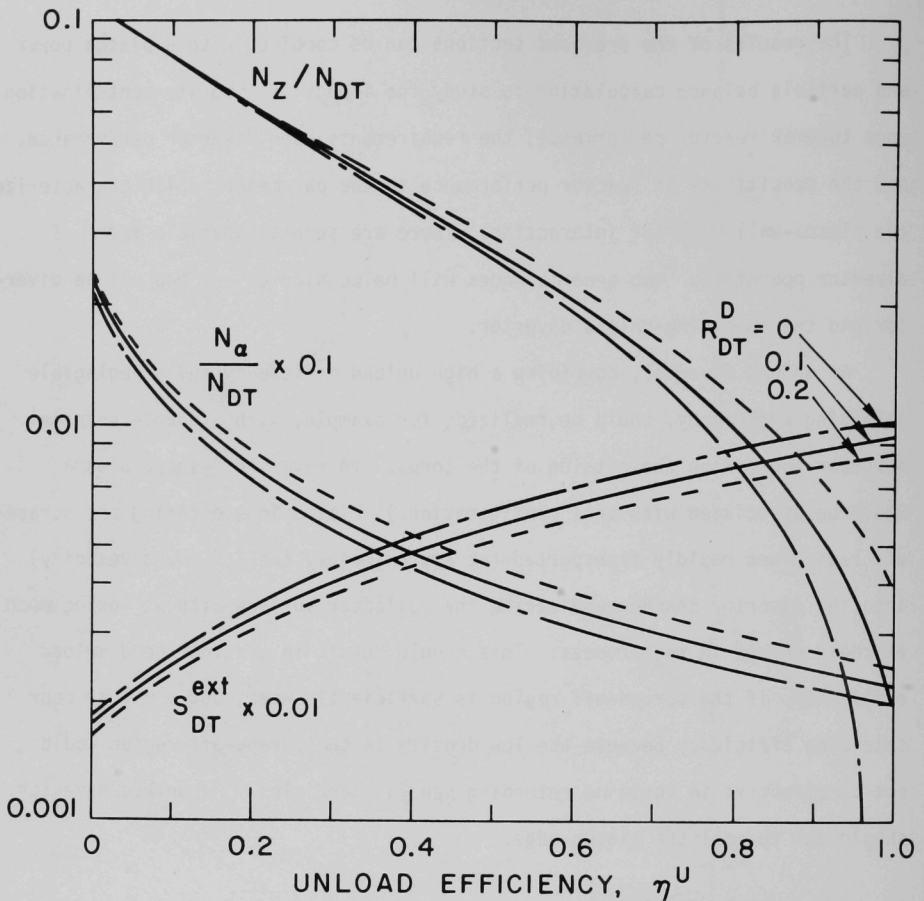


Fig. 22a. Normalized wall-sputtered and alpha impurity concentrations and fuel replenishment rate as a function of unload divertor efficiency and divertor backflow fraction. ($\eta^S = 0.05$, $R_{DT}^W = R_\alpha^W = 0.95$, $R_z^W = R_c^W = 0.05$, $R_\alpha^d = R_{DT}^d = 0.1$, $R_z^d = R_c^d = 0$, $\gamma_c = 0.05$, $T_{edge} = 200$ eV, $T_c = T_{ns} = 1/2 T_{edge}$, $T_{np} = 2 T_{edge}$.)

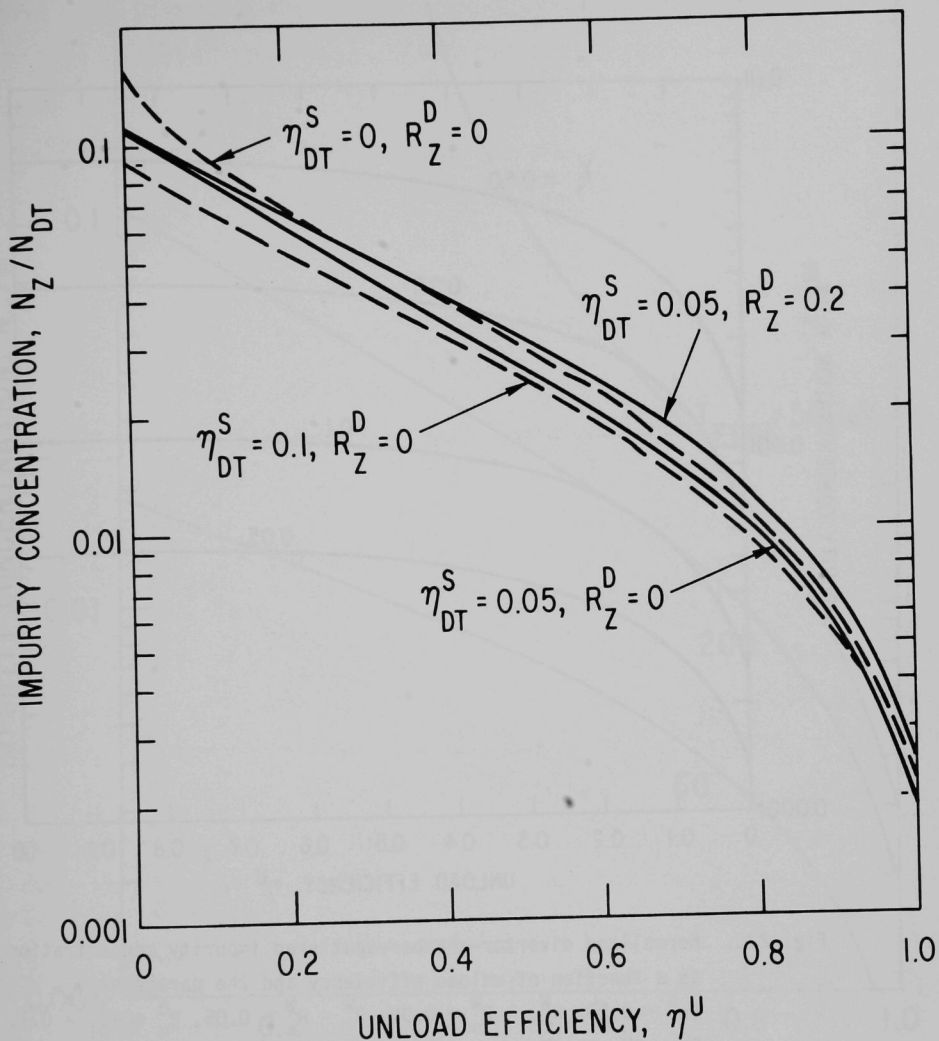


Fig. 22b. Normalized wall-sputtered impurity concentration as a function of unload and shielding divertor efficiencies and divertor backflow fraction. ($R_{DT}^W = R_\alpha^W = 0.95$, $R_Z^W = R_C^W = 0.05$, $R_\alpha^d = R_{DT}^d = 0.1$, $R_C^d = R_Z^d$, $\gamma_c = 0.05$, $T_{edge} = 200$ eV, $T_c = T_{ns} = 1/2 T_{edge}$, $T_{np} = 2 T_{edge}$.)

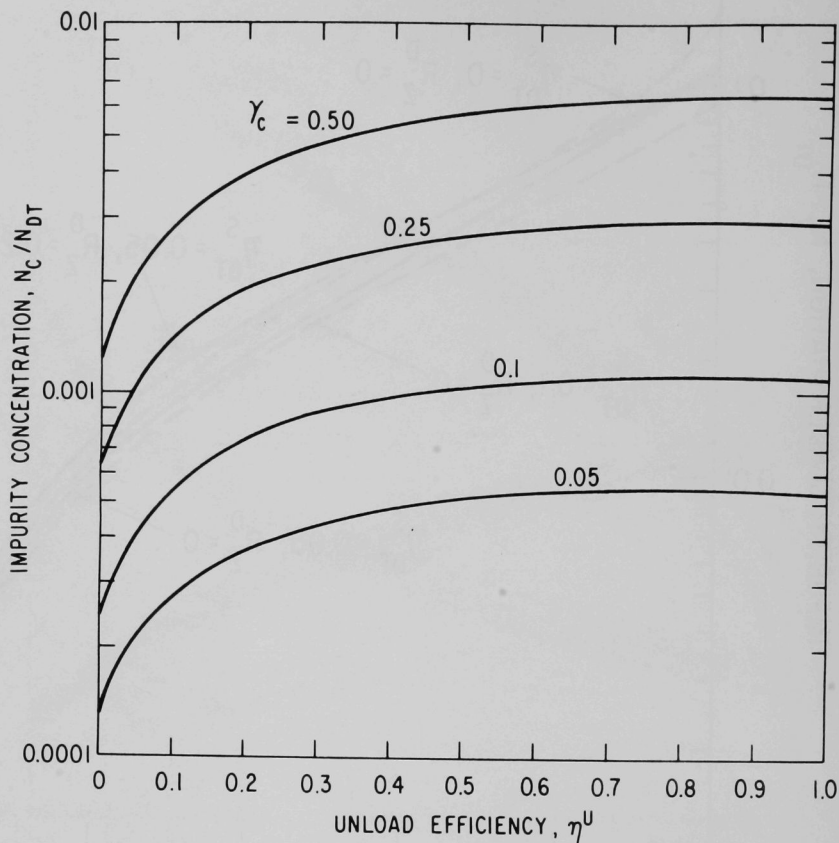


Fig. 22c. Normalized divertor-chamber-sputtered impurity concentration as a function of unload efficiency and the parameter γ_c .
 ($\eta^S = 0.05$, $R_{DT}^W = R_\alpha^W = 0.95$, $R_z^W = R_c^W = 0.05$, $R_\alpha^d = R_{DT}^d = 0.1$,
 $R_c^d = R_z^d = 0$, $T_{edge} = 200$ eV, $T_c = T_{ns} = 1/2 T_{edge}$,
 $T_{np} = 2 T_{edge}$.)

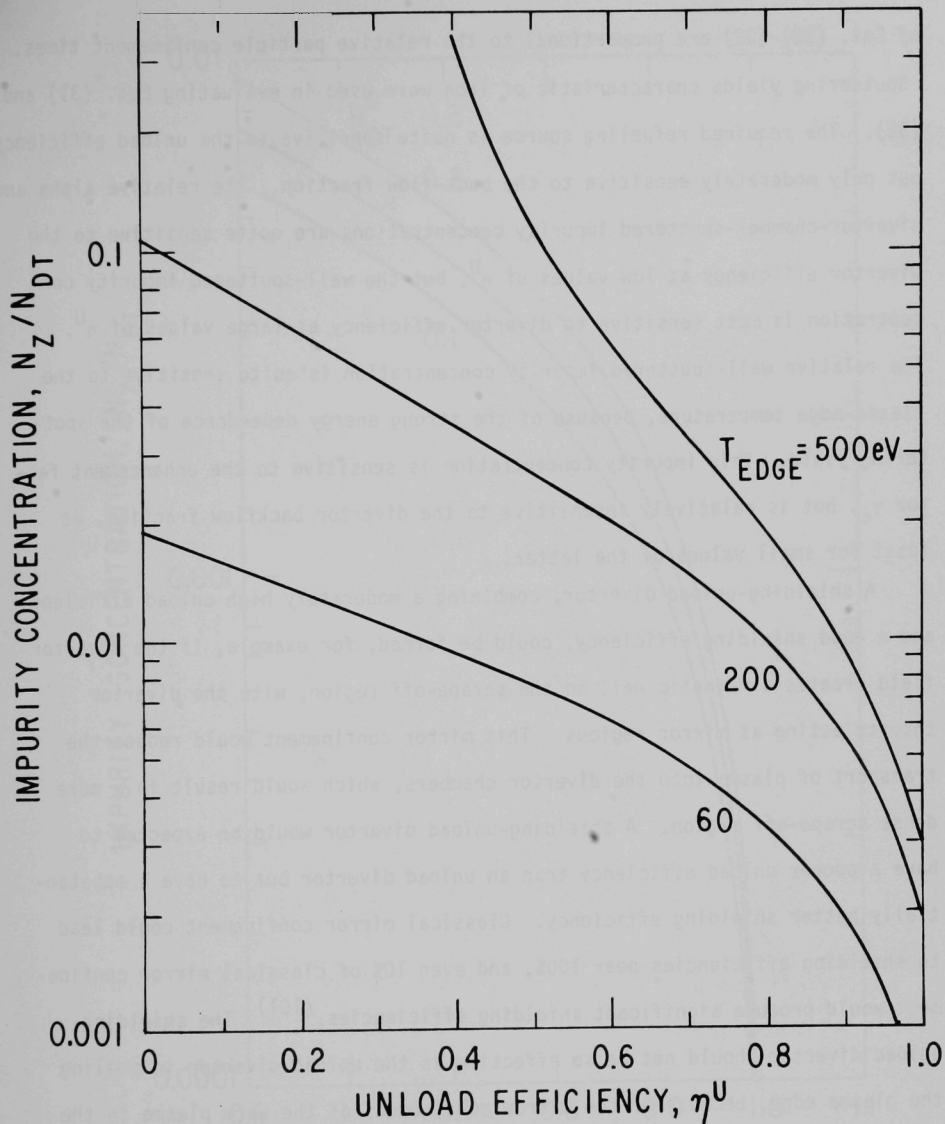


Fig. 22d. Normalized wall-sputtered impurity concentration as a function of unload efficiency and plasma-edge temperature ($\eta^S = 0.05$, $R_{DT}^W = R_\alpha^W = 0.95$, $R_z^W = R_c^W = 0.05$, $R_\alpha^d = R_{DT}^d = 0.1$, $R_c^d = R_z^d = 0$, $\gamma_c = 0.05$, $T_c = T_{ns} = 1/2 T_{edge}$, $T_{np} = 2 T_{edge}$.)

of Eqs. (30)-(32) are proportional to the relative particle confinement times.

Sputtering yields characteristic of iron were used in evaluating Eqs. (31) and (32). The required refueling source is quite sensitive to the unload efficiency but only moderately sensitive to the back-flow fraction. The relative alpha and divertor-chamber-sputtered impurity concentrations are quite sensitive to the divertor efficiency at low values of n^U , but the wall-sputtered impurity concentration is most sensitive to divertor efficiency at large values of n^U . The relative wall-sputtered impurity concentration is quite sensitive to the plasma-edge temperature, because of the strong energy dependence of the sputtering yield. This impurity concentration is sensitive to the enhancement factor γ_c , but is relatively insensitive to the divertor backflow fraction, at least for small values of the latter.

A shielding-unload divertor, combining a moderately high unload efficiency and a good shielding efficiency, could be formed, for example, if the divertor field creates a magnetic well in the scrape-off region, with the divertor throats acting as mirror regions. This mirror confinement would reduce the transport of plasma into the divertor chambers, which would result in a more dense scrape-off region. A shielding-unload divertor would be expected to have a poorer unload efficiency than an unload divertor but to have a substantially better shielding efficiency. Classical mirror confinement could lead to shielding efficiencies near 100%, and even 10% of classical mirror confinement would produce significant shielding efficiencies.⁽¹⁰¹⁾ The shielding-unload divertor should not be so effective as the unload divertor in cooling the plasma edge, because of the mirror confinement of the warm plasma in the scrape-off region.

Equations (27) and (30)-(32) have been evaluated for a range of parameter values characteristic of a shielding-unload divertor. These results are plotted in Figs. 23a-23d. The normalization is the same as discussed previously. The wall-sputtered impurity concentration is extremely sensitive to

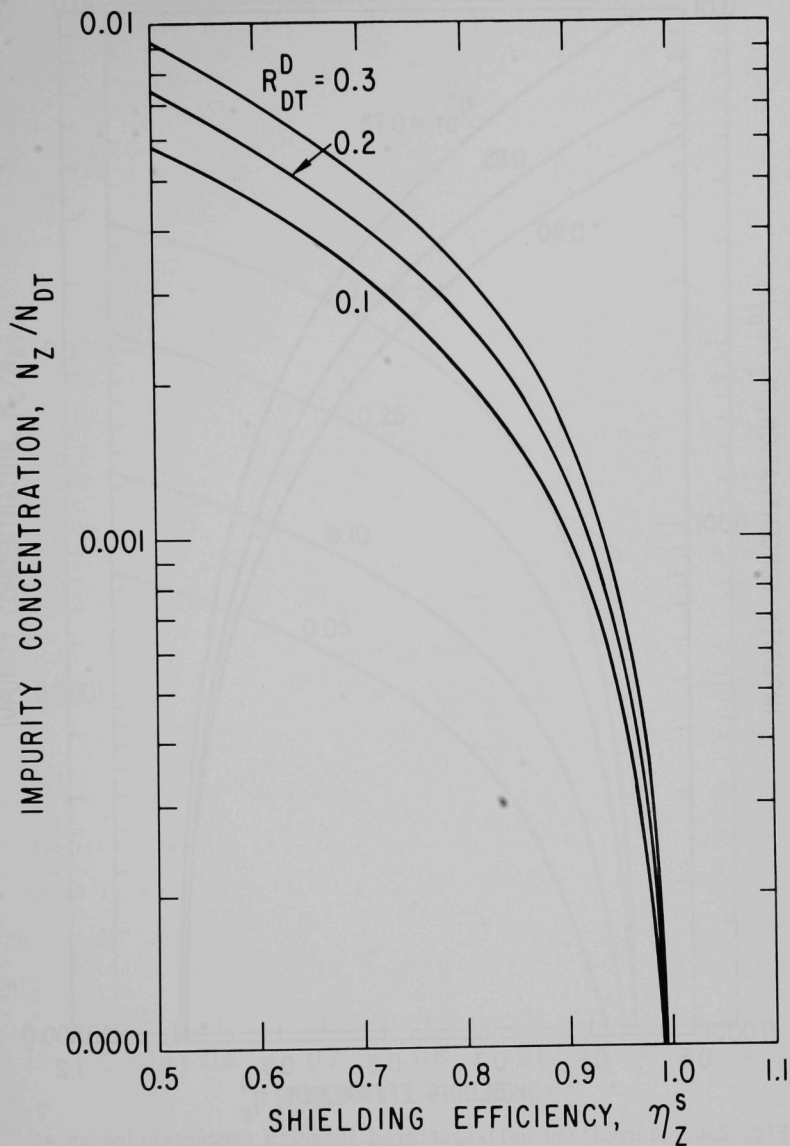


Fig. 23a. Normalized wall-sputtered impurity concentration as a function of shielding divertor efficiency and divertor backflow fraction. ($\eta^U = 0.85$, $\eta_c^S = \eta_z^S$, $\eta_{DT}^S = \eta_\alpha^S = 0.50$, $R_\alpha^d = R_{DT}^d$, $R_c^d = R_z^d = 0.05$, $R_{DT}^W = R_\alpha^W = 0.95$, $R_z^W = R_c^W = 0.05$, $\gamma_c = 0.1$, $T_{edge} = 500$ eV, $T_c = 1/10 T_{edge}$, $T_{ns} = 1/2 T_{edge}$, $T_{np} = 2 T_{edge}$.)

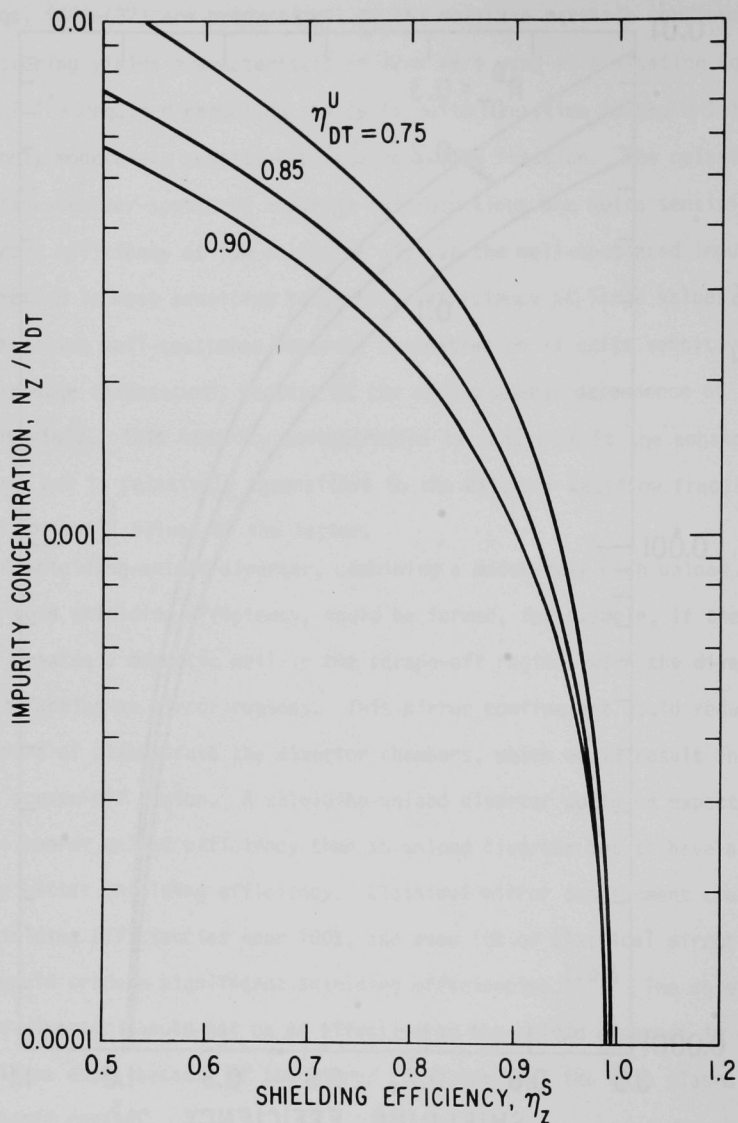


Fig. 23b. Normalized wall-sputtered impurity concentration as a function of shielding and unload divertor efficiencies.

($\eta_z^U = \eta_z^U = \eta_z^U = \eta_{DT}^U$, $\eta_c^S = \eta_z^S$, $\eta_{DT}^S = \eta_\alpha^S = 0.50$, $R_{DT}^d = R_{DT}^d = 0.2$, $R_z = R_c = 0.05$, $R_{DT}^W = R_\alpha^W = 0.95$, $R_z^W = R_c^W = 0.05$, $\gamma_c = 0.1$, $T_{edge} = 500$ eV, $T_c = 1/10 T_{edge}$, $T_{ns} = 1/2 T_{edge}$, $T_{np} = 2 T_{edge}$.)

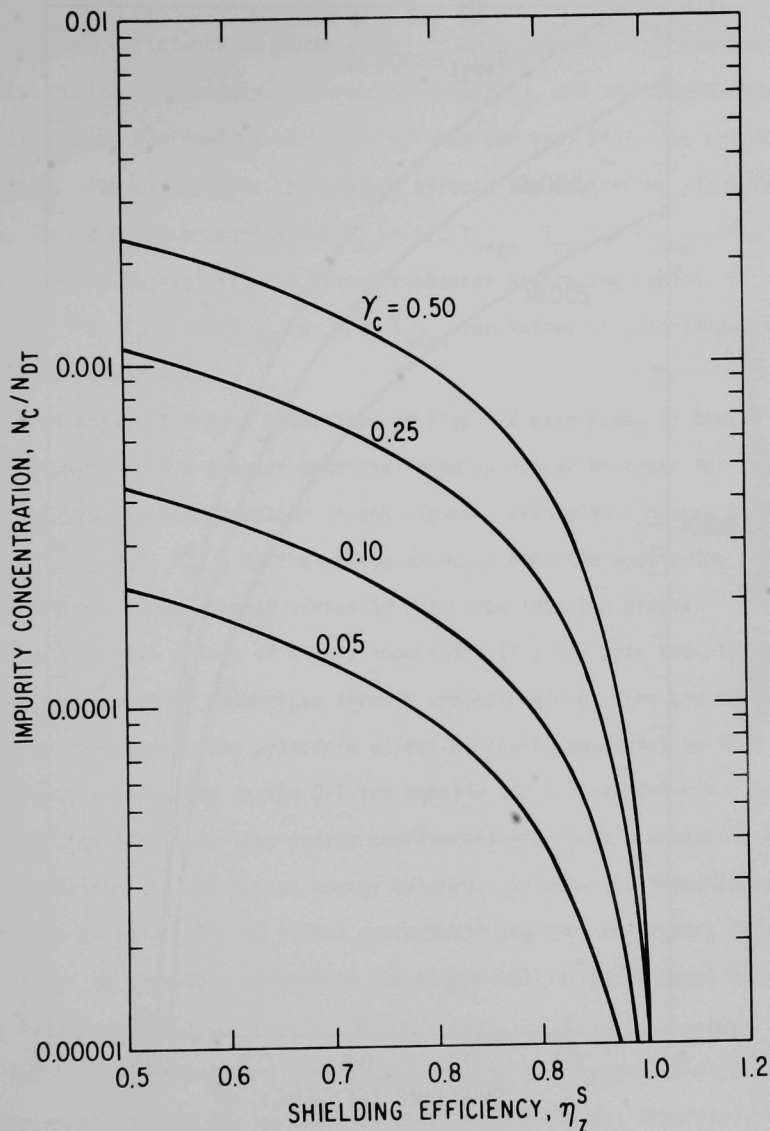


Fig. 23c. Normalized divertor-chamber-sputtered impurity concentrations as a function of shielding divertor efficiency and the parameter γ_c . ($\eta^U = 0.85$, $\eta_c^S = \eta_z^S$, $\eta_{DT}^S = \eta_\alpha^S = 0.50$, $R_{DT}^d = R_\alpha^d = 0.2$, $R_c^d = R_z^d = 0.05$, $R_{DT}^W = R_\alpha^W = 0.95$, $R_z^W = R_c^W = 0.05$, $T_{edge} = 500$ eV, $T_e = 1/10 T_{edge}$, $T_{ns} = 1/2 T_{edge}$, $T_{np} = 2 T_{edge}$.)

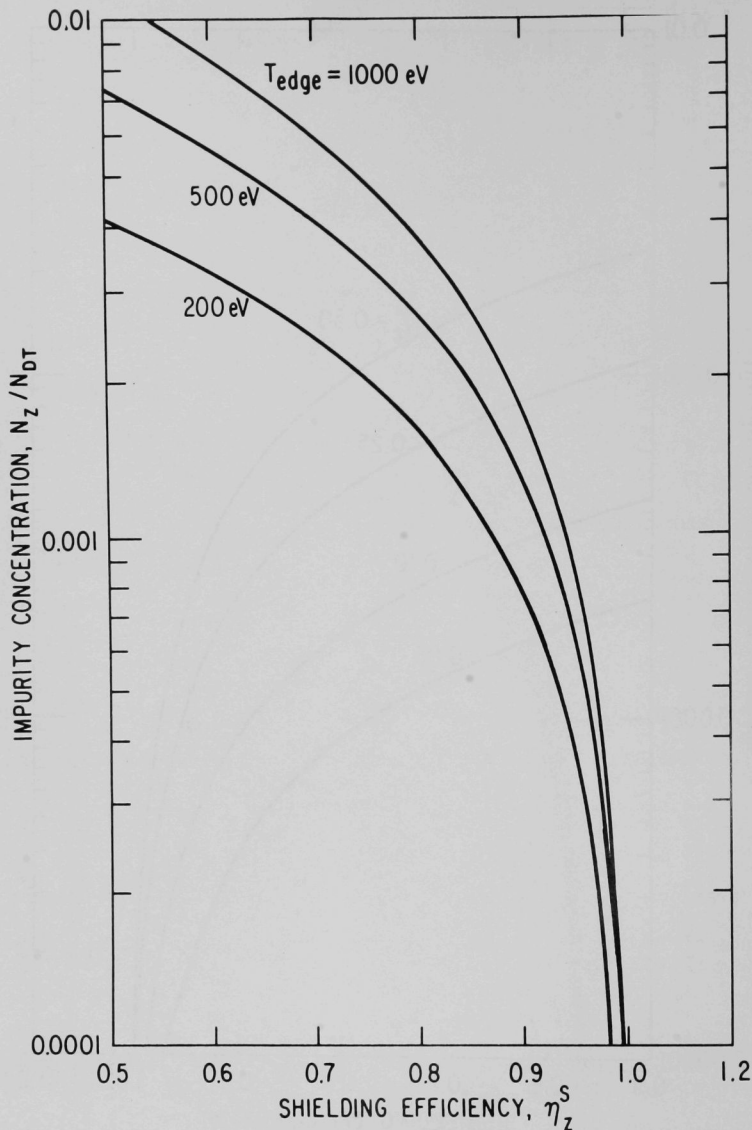


Fig. 23d. Normalized wall-sputtered impurity concentration as a function of shielding divertor efficiency and plasma-edge temperature. ($\eta^U = 0.85$, $\eta_c^S = \eta_z^S$, $\eta_{DT}^S = \eta_\alpha^S = 0.50$, $R_{DT}^d = R_\alpha^d = 0.2$, $R_c^d = R_z^d = 0.05$, $R_{DT}^W = R_\alpha^W = 0.95$, $R_z^W = R_c^W = 0.05$, $\gamma_c = 0.1$, $T_c = 1/10 T_{edge}$, $T_{ns} = 1/2 T_{edge}$, $T_{np} = 2 T_{edge}$.)

the shielding efficiency at large values of η^S . Importance of the back-flow fraction, unload efficiency, divertor parameter γ_c , and the plasma-edge temperature is greater for smaller values of η^S than for very efficient shielding divertors. The plasma-edge temperature affects the sputtering yield according to Eq. (22) and the prescriptions $T_{ns} = 1/2 T_{edge}$, $T_{np} = 2 T_{edge}$. The temperature, T_c , used to evaluate the divertor chamber sputtering yields, Y^c , is evaluated from $T_c = 1/2 T_{edge}$ or $1/10 T_{edge}$ for unload or shielding-unload divertors, respectively.

It is apparent from a comparison of Figs. 22 with Figs. 23 that a shielding-unload divertor has a greater potential than an unload divertor for achieving a very low impurity concentration in the plasma. Even with a nearly perfect divertor ($\eta_{DT}^U \leq 1$, $R_{DT}^d \geq 0$) the charge-exchange enhanced sputtering produces impurity atoms which proceed virtually unimpeded into the plasma.

The principal effect of high-Z impurities ($Z \geq 14$) upon the plasma is to enhance the radiative power loss through bremsstrahlung, line and recombination radiation processes. The principle effect of low-Z impurities is that they necessitate a reduction in the D-T ion density for a fixed β -limit. Both types of impurities also alter the energy confinement and cause a number of less important alterations in the plasma energy balance. In order to investigate the importance of impurities to plasma performance and the requirement for impurity control, it is necessary to combine the plasma-wall-divertor model with a plasma power balance model.

The plasma computational model used in this study consists of coupled balance equations for the various ion species (D-T, alpha, impurity), as described in Section I, and power balance equations⁽¹⁴⁾ for the D-T ions and electrons. A relatively flat spatial density profile and a spatial temperature profile somewhat more peaked than parabolic are used in the power balance calculations. Neutral beam and fusion-alpha heating and radiative and trans-

port power losses are treated. The radiative power loss model was described in Section III.

This plasma model has been employed to compute the value of the energy confinement parameter, $n\tau_E$, which is required for a self-sustaining fusion reaction. Results are shown in Figs. 24a-24d for different impurities as a function of relative impurity concentrations and average electron temperature. A 1/2% background oxygen concentration and an equilibrium alpha particle concentration with no alpha recycling are also present. The devastating effect of even small quantities of high-Z impurities is apparent. The maximum impurity concentration for which a self-sustaining reaction can be achieved is shown in Fig. 25 as a function of the atomic number of the impurity. For comparison, the same quantity calculated with a more elaborate radiative power-loss model⁽¹⁵⁾ and a somewhat different plasma power balance model is also shown.⁽⁷⁾

The type of divertor parameters which would be required to achieve suitably small impurity concentrations can be determined by comparing Figs. 22 and 23 with Figs. 24 and 25. For first-wall materials other than stainless steel (represented by iron), the concentrations in Figs. 22 and 23 must be scaled by the sputtering yield of the material in question relative to that of iron, using Table IV.

The sensitivity of the confinement required for ignition to the radiation model is shown in Fig. 26. The upper curve is based upon Eq. (72), which was used for the calculations reported in Figs. 23 and 24. The lower curve is based upon the calculations of Merts, et al.⁽¹⁰⁷⁾ shown in Fig. 21. No ignited solution was found in calculations which used Eq. (74).

These results provide a general perspective of the effect of impurities upon ignition (self-sustaining operation) conditions and of the efficiency

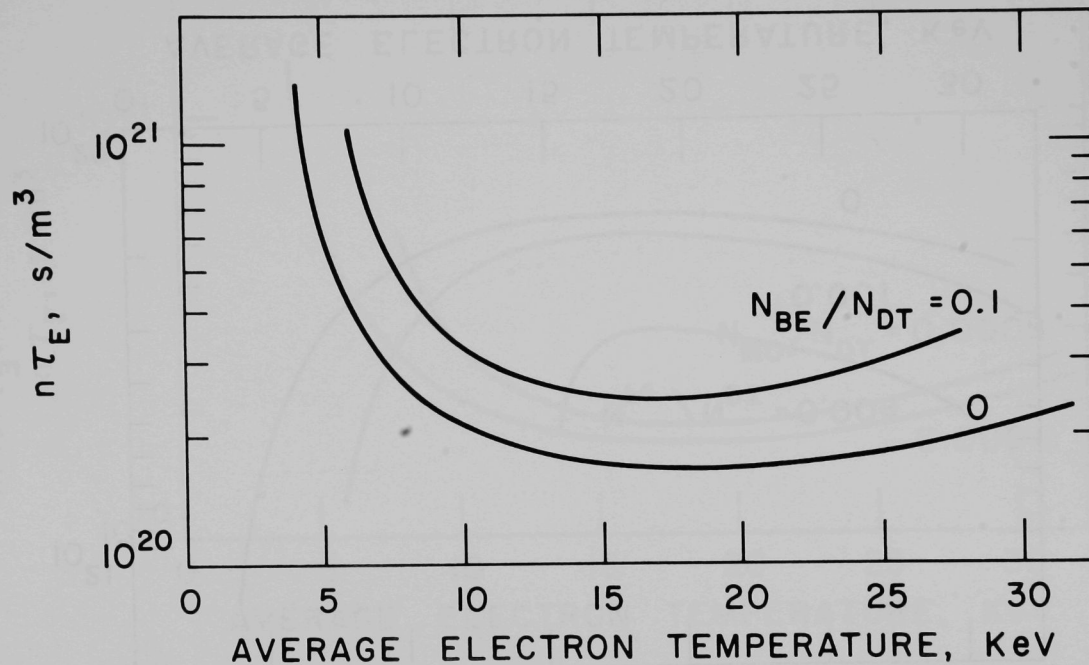


Fig. 24a. Energy confinement required for ignition as a function of beryllium impurity concentration.

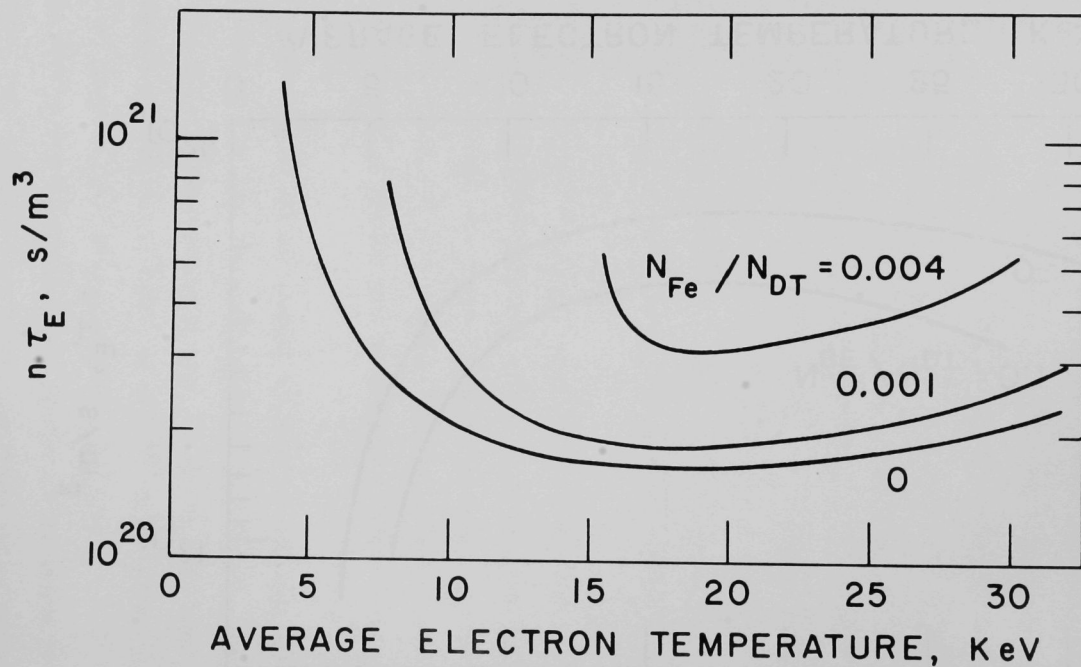


Fig. 24b. Energy confinement required for ignition as a function of iron impurity concentration.

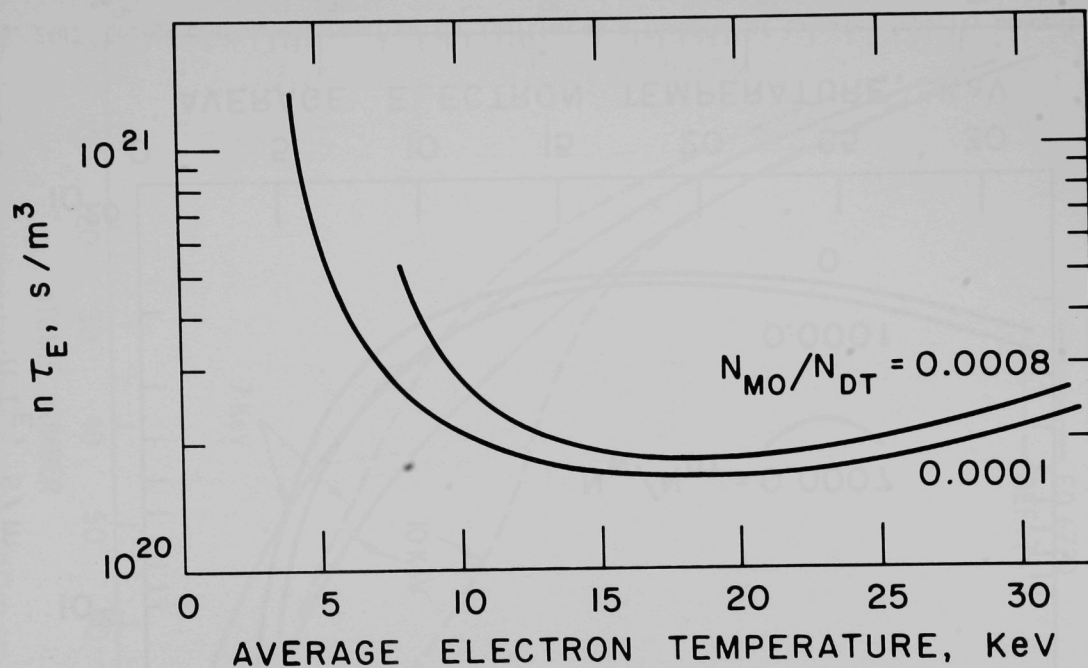


Fig. 24c. Energy confinement required for ignition as a function of molybdenum impurity concentration.

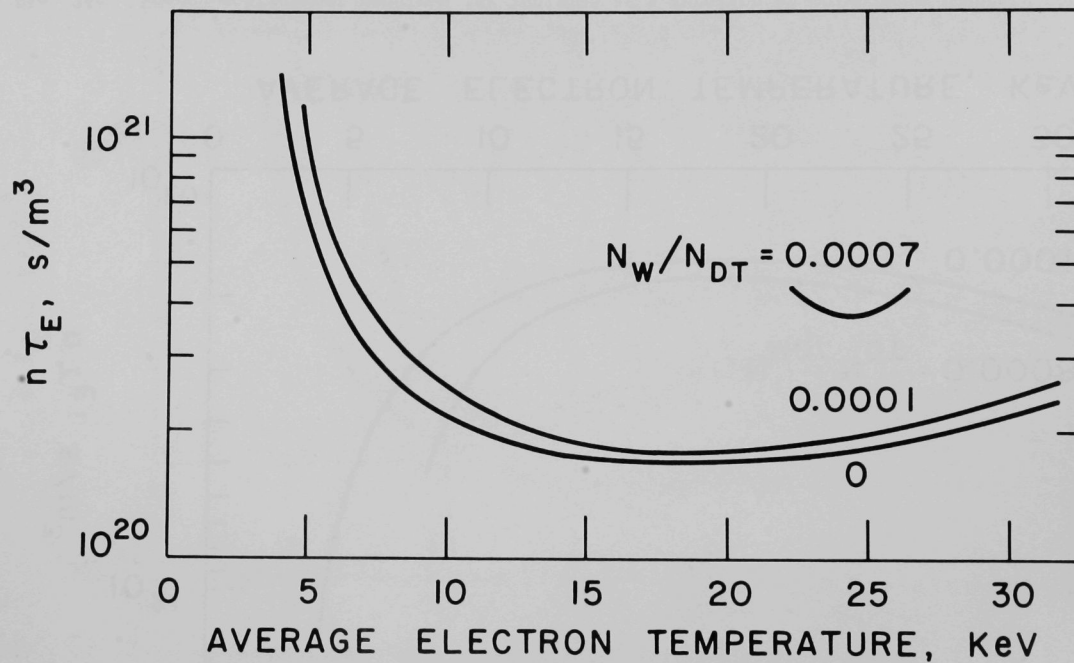


Fig. 24d. Energy confinement required for ignition as a function of tungsten impurity concentration.

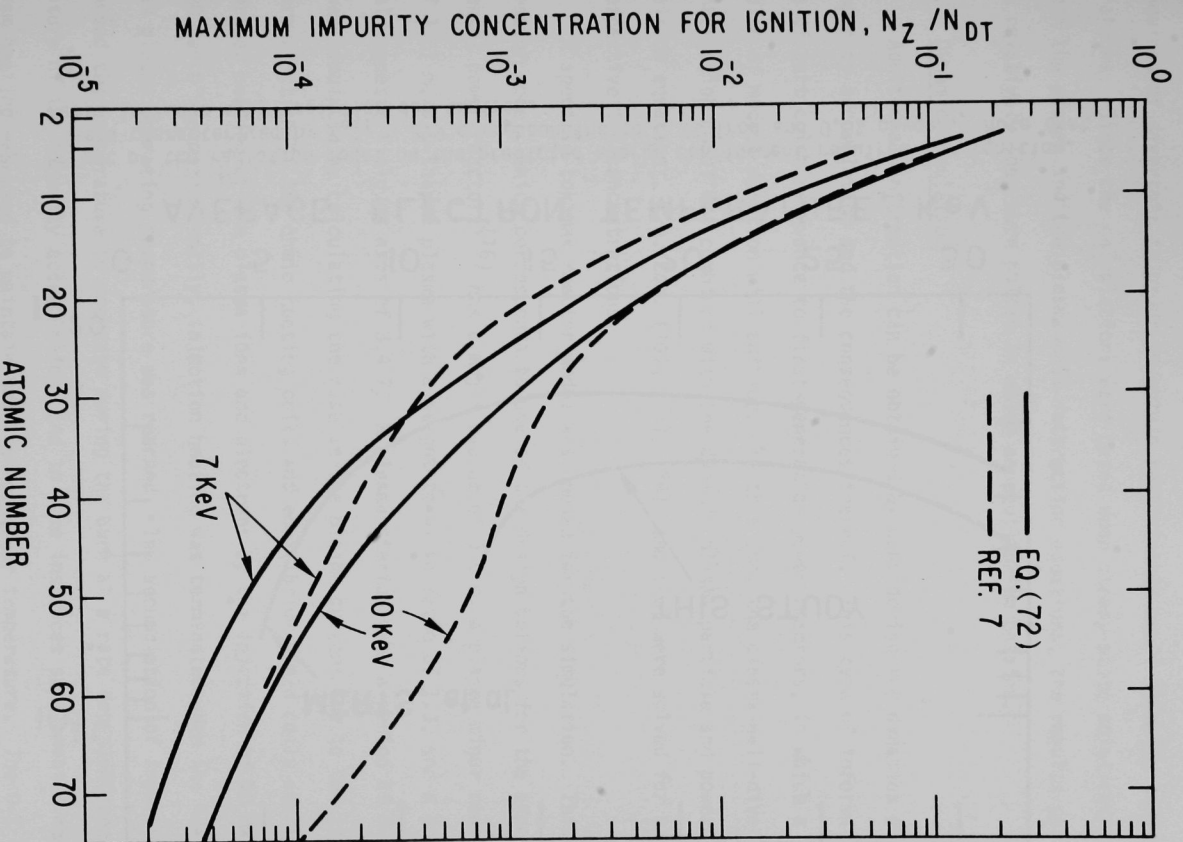


Fig. 25. Maximum impurity concentration for which ignition can be achieved.

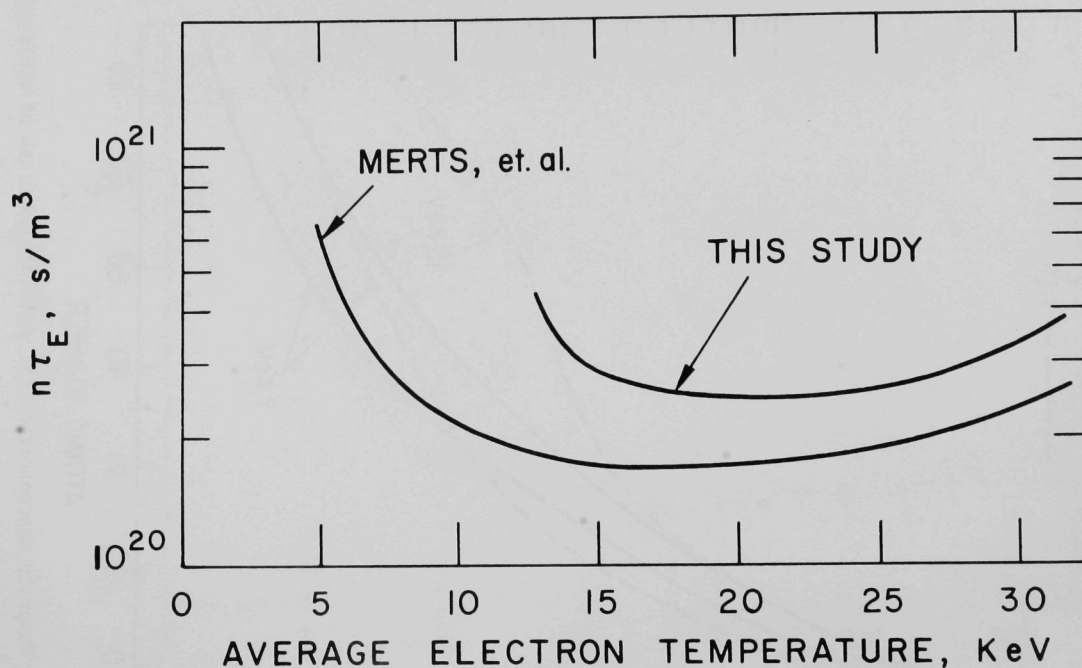


Fig. 26. Effect of the radiation model on the predicted energy confinement required for ignition. Plasma characterized by $Z_{eff} \sim 2.9$ corresponding to 0.3% iron and 0.5% oxygen. Note that Merts includes only radiation due to iron.

required of divertors in order to obtain sufficiently small impurity concentrations. Since the calculations were based upon steady-state solutions of both the plasma and the plasma-wall interaction equations, the results pertain to relatively long burn pulses in which an equilibrium obtains.

B. Dynamic Simulation

Additional information can be obtained by considering the dynamics of impurity accumulation and the consequences thereof. This type of information is of particular relevance to first-generation power reactors, in which a burn pulse of modest duration will suffice. To this end, the plasma-wall-divertor interaction model was combined with the dynamic plasma particle and power balance equations, i.e. Eqs. (10), (15), (24), and (26) were solved for the respective ion concentrations.

A specific tokamak reactor model was chosen for the simulation. This reactor model, which corresponds to one of the design options for the experimental power reactor,⁽¹⁶⁾ has a major radius of 5.0 m, a plasma minor radius of 1.67 m, a D-shaped plasma with a height-to-width ratio of 1.3, and a toroidal magnetic field on axis of 3.4 T. A plasma startup over a period of 6-8 s was simulated by calculating the rise in the plasma current due to the transformer action of the ohmic heating coils and equilibrium field coils and the further heating of the plasma ions and electrons by the injection of 40 MW of 180 keV D⁺ beams. Normally, injection heating was terminated when the ~8-10 keV plasma operating temperature was reached. The accumulation of impurities caused the temperature to decrease during the burn at a rate dependent upon the nature of the impurity accumulation, and in some instances supplemental neutral beam heating was used to maintain the thermonuclear temperature. The D-T ion density was limited by the constraint $\beta_t \leq 8\%$ and generally decreased somewhat during the burn pulse as alpha particles and impurities accumulated in the plasma.

External refueling was postulated to supplement the recycling in maintaining the D-T ion density at the β_t -limit. Particle-and-energy loss rates from the plasma were computed from a multi-regime (pseudo-classical electrons/neoclassical ions at large collision frequencies and trapped-particle mode at lower collision frequencies) confinement model. The full plasma current in each case was 6.75 MA.

The results of these dynamic simulations are presented in terms of the net electrical power produced in the burn pulse and the length of the burn pulse. The net electrical power computation accounts for the conversion of fusion energy to electricity with a 25% efficiency and for the electrical energy required to operate the neutral injection, poloidal coil, cryogenics, vacuum, coolant pumping, and other reactor and plant systems. The maximum length of the burn pulse is set by impurity accumulation extinguishing the plasma.

1. First-Wall Modification

A series of calculations was performed for a reactor operating without a divertor in order to evaluate the potential of first-wall modifications for impurity control. The sputtering data of Table IV were used. With a bare stainless steel (represented by iron) first-wall, the plasma could not be heated above 2 keV because of the very high impurity radiation. The net electrical power was several hundred megawatts negative and the required power injection rapidly exceeded 100 MW. The situation was even less favorable when the wall (or limiter) material was tungsten.

One possible solution to the impurity problem is to make the first surface facing the plasma of a low atomic number (low-Z) material. This could be accomplished by coating the structural first-wall to a thickness of 60-200

microns or by inserting a more substantial amount of low-Z material between the plasma and the structural first-wall either in bulk form or as stand-off liners or curtains. The variety of such concepts and their technological feasibility are discussed elsewhere.⁽⁶⁾

Calculations for various first-surface materials are summarized in Figs. 27-29. By comparison to the case which would obtain if sputtering were completely suppressed, it is apparent that burn pulses with somewhat diminished but still acceptable performance and with lengths of ~ 1 -2 min can be obtained in this reactor model by using a low-Z first-surface material such as carbon, beryllium, B_4C , or beryllium oxide. Less favorable performance was obtained with a SiC first-surface, in which case it was necessary to use increasing amounts of supplemental beam heating up to 100 MW injected power to maintain the burn pulse for 30 s. As discussed in Section II-C, chemical sputter yields are substantially greater than physical sputter yields for carbon when bombarded by hydrogenous ions at surface temperatures of 400-800°C. The plasma performance for the case of a carbon first-surface is shown in Fig. 28 for conditions where chemical sputtering predominates. The performance is severely degraded from that obtained with physical sputtering only, and a supplemental beam heating up to 100 MW is required to maintain a 25-s burn pulse. Although the chemical sputter data for carbon indicate low yields at wall temperatures of 800-1200°C, the practical aspects of heating and maintaining the wall at these temperatures must be considered when assessing the capability of impurity control with a carbon or graphite liner. Chemical sputtering is less well understood for other wall materials, however, the importance of this phenomenon may also be important, particularly for candidate carbide wall materials.

The sensitivity of the net electrical power production and the maximum burn pulse length to the plasma-edge temperature are illustrated in Fig. 28.

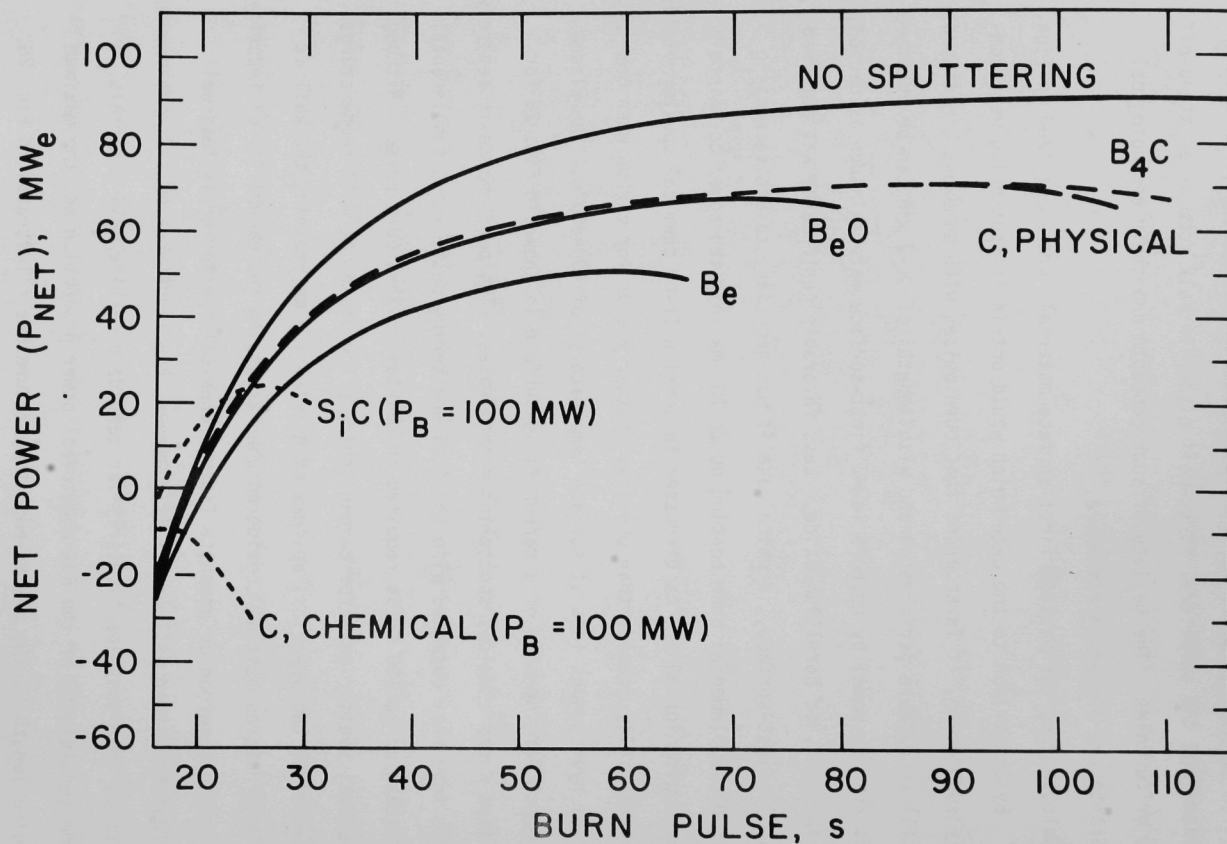


Fig. 27. Reactor power output as a function of first-surface material ($T_{edge} = 200$ eV).

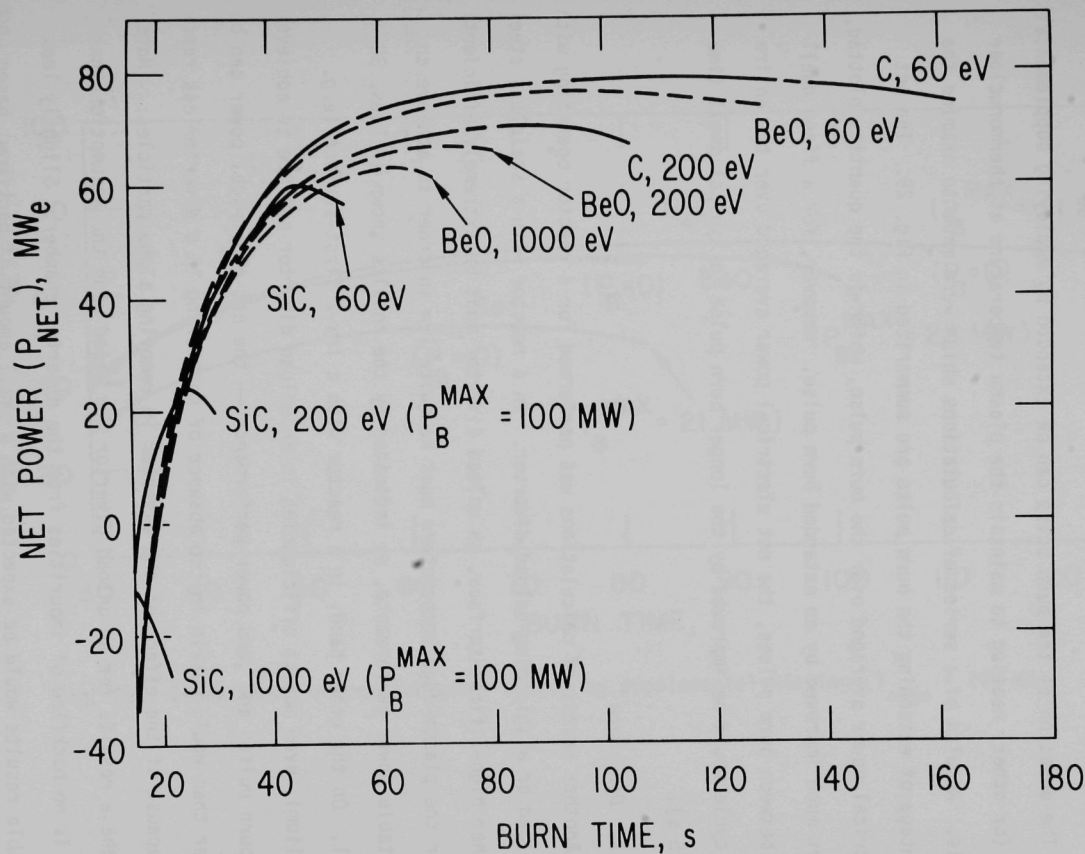


Fig. 28. Reactor power output as a function of first-surface material and plasma-edge temperature.

These results follow directly from the incident particle energy dependence of the sputtering yields and from the energy dependence of the charge-exchange probability.

The duration of the burn pulse can be extended by employing supplemental beam (or other) heating to maintain the plasma temperature at thermonuclear levels. Results of a series of calculations which were made to examine the advantage of extending the burn pulse are summarized in Fig. 29. The net electrical power averaged over the burn pulse, which is the quantity plotted, is not much improved by an extended burn pulse. However, for a fixed dwell time between burn pulses, the net electrical power averaged over the entire burn cycle would be improved by the longer burn pulse (a typical dwell time is ~ 15 s).

2. Divertors

Another series of calculations was performed for a reactor operating with an unload or a shielding-unload divertor. In a reactor with a stainless steel or other high-Z first-surface, an unload divertor must be extremely efficient and/or the plasma-edge temperature must be quite low in order to achieve an acceptable power performance, as indicated by the results shown in Figs. 30 and 31. On the other hand, in a reactor with a low-Z first-surface (e.g. beryllium), even modest efficiencies in an unload divertor suffice to achieve long burn pulses and good power performance — the net electrical power can be greater than would obtain in the absence of sputtering in a divertorless reactor because of the effect of the divertor in removing alpha particles. (Note that these results for an unload divertor are based upon the assumption that there is no backflow of impurities from the divertor chamber. Slightly less favorable results would be expected with a small amount of backflow, based upon the results shown in Fig. 22.

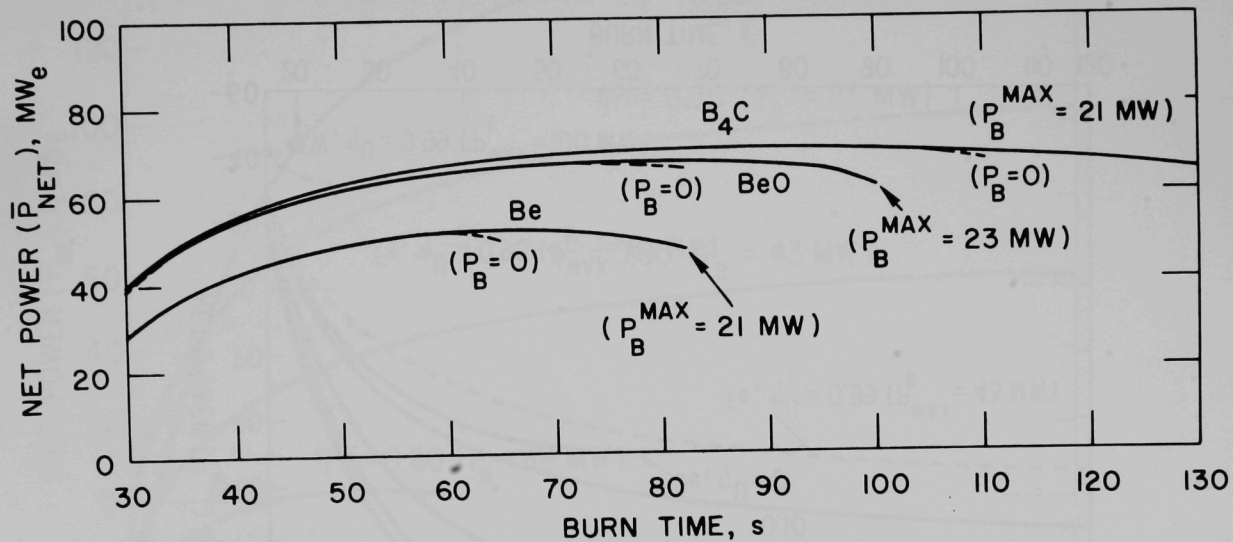


Fig. 29. Enhancement of reactor power output by supplemental heating ($T_{edge} = 200$ eV).

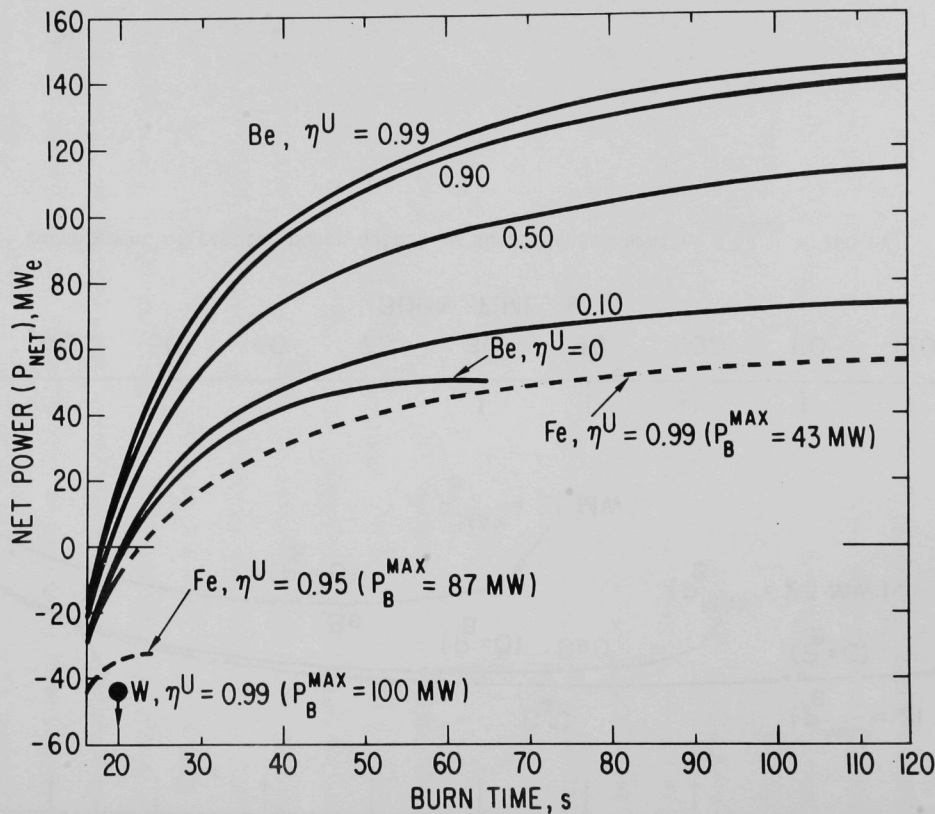


Fig. 30. Reactor power output as a function of unload divertor efficiency and first-surface material. ($\eta^S = 0.05$, $R_{DT}^W = R_\alpha^W = 0.95$, $R_z^W = R_c^W = 0.05$, $R_{DT}^d = R_\alpha^d = 0.1$, $R_z^d = R_c^d = 0.0$, $\gamma_c = 0.05$, $T_{edge} = 200 \text{ eV}$, $T_c = T_{ns} = 1/2 T_{edge}$, $T_{np} = 2 T_{edge}$.)

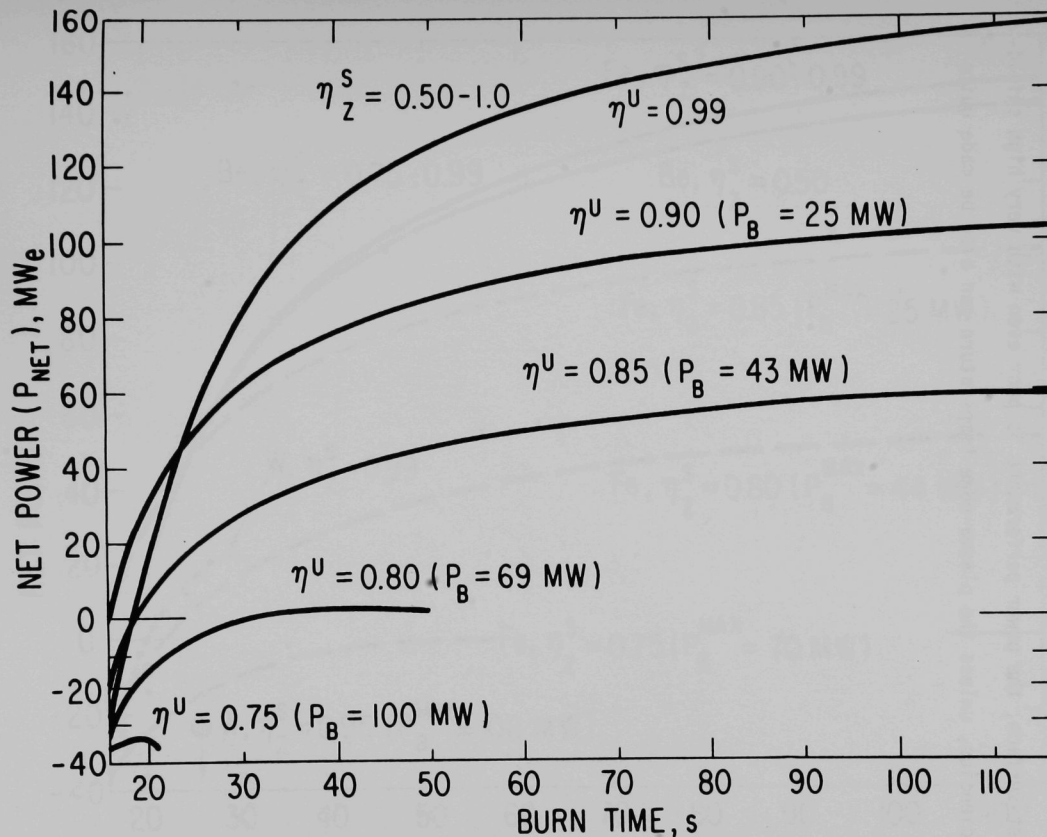


Fig. 31. Reactor power output as a function of unload divertor efficiency with a steel first-surface and $T_{edge} = 60$ eV. ($\eta_z^S = 0.05$, $R_{DT}^W = R_{\alpha}^W = 0.95$, $R_z^W = R_c^W = 0.05$, $R_{DT}^d = R_{\alpha}^d = 0.1$, $R_z^d = R_c^d = 0.0$, $\gamma_c = 0.05$, $T_c = T_{ns} = 1/2 T_{edge}$, $T_{np} = 2 T_{edge}$.)

A shielding-unload divertor should yield quite satisfactory performance for this reactor with a stainless steel first-surface if shielding efficiencies $\geq 85\%$ can be achieved, as shown in Fig. 32. With a low-Z first-surface (e.g. beryllium), shielding efficiencies $\geq 50\%$ should suffice. However, with a tungsten first-surface, the power performance is poor even with very high shielding efficiencies, unless the plasma-edge temperature can also be made quite low.

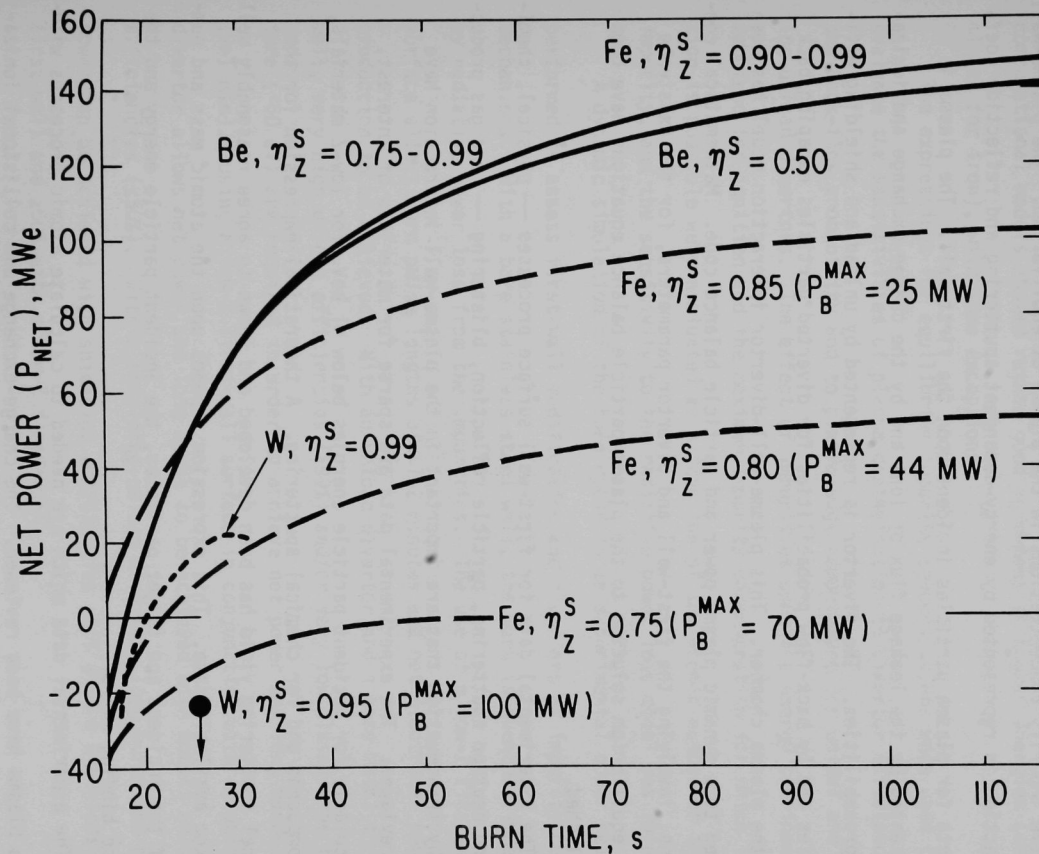


Fig. 32. Reactor power output as a function of shielding diverter efficiency and first-surface material. ($\eta^U = 0.85$, $R_{DT}^W = R_\alpha^W = 0.95$, $R_z^W = R_c^W = 0.05$, $R_{DT}^d = R_\alpha^d = 0.2$, $R_z^d = R_c^d = 0.05$, $\gamma_c = 0.1$, $T_{edge} = 500$ eV, $T_{ns} = 1/2 T_{edge}$, $T_c = 1/10 T_{edge}$, $T_{np} = 2 T_{edge}$.)

V. SUMMARY AND CONCLUSIONS

A mathematical model has been developed for particle fluxes to the first-wall and into the divertor chamber, for impurity sources to the plasma and for relative impurity concentrations in the plasma at equilibrium. The plasma-wall interaction is represented by energy-dependent sputtering and reflection coefficients for plasma particles incident upon the first-wall. The plasma is represented by the leakage flux of ions and by the charge-exchange and ionization probabilities. The divertor is represented by unload and shielding efficiencies and by back-flow probabilities for diverted particles escaping back into the plasma chamber. This plasma-wall-divertor interaction model has been coupled to a dynamic plasma power and particle balance code. Mathematical conditions, involving the first-wall and divertor parameters, for the existence of an equilibrium solution to the plasma particle balance equations have been established.

The experimental data for first-wall surface processes — physical, chemical and neutron sputtering, particle reflection, blistering — and gas production by transmutation that are important in the plasma-wall interaction have been reviewed. The experimental data are sparse for materials of interest, particularly for incident particle energies below ~ 1 keV, for low-Z materials, for compounds and for chemical sputtering. A theoretical expression for the physical sputtering yield has been developed and shown to agree reasonably well with the available data. This expression depends upon the atomic mass and number of the incident and target particles, the incident particle energy and the surface binding energy.

The experimental data which are needed to calculate atomic processes within the plasma have been reviewed. The charge-exchange and collisional ionization rates needed to compute charge-exchange probabilities are reasonably well

known. The data for the electron-collisional excitation and ionization rates and the radiative recombination rates are adequate only for low-Z ions. Neither theory nor experiment has yet provided adequate data for the intermediate-to-high Z ions. Predictions of radiative power loss based upon several different computational models showed rather good agreement at higher energies (above ~ 1 keV for iron), with some exceptions.

The expressions for equilibrium impurity concentrations were used to evaluate the sensitivities of plasma contamination to divertor efficiencies and back-flow probability and to plasma-edge temperature for unload and shielding-unload divertors. The effect of impurities upon the energy confinement required for ignition and the maximum impurity concentration for which ignition is possible were evaluated as a function of the atomic number of the impurity, and the sensitivity to the radiative power loss model was investigated.

A dynamic simulation of the burn cycle in an experimental power reactor was performed to assess first-wall modification and divertors as impurity control mechanisms. With a bare stainless steel wall, the burn is quenched immediately by radiative power loss from the impurities. The use of a low-Z first-wall surface allows burn pulse lengths of ~ 1 -2 minutes and net electrical power production to be achieved. With an unload divertor and a bare metal first-wall, very high unload efficiencies ($\geq 99\%$) and/or very low plasma-edge temperature (< 60 eV) are required in order to achieve net power and long burns (> 1 min). Using a low-Z first-wall surface in conjunction with an unload divertor allows net power and long burns to be achieved with modest unload efficiencies ($\leq 50\%$). With a shielding-unload divertor, long burns and net power can be achieved with shielding efficiencies $\geq 85\%$ with a stainless steel first-wall and $\geq 50\%$ with a low-Z first-wall.

REFERENCES

- ¹R. BEHRISCH and B. B. KADOMTSEV, "Plasma Impurities and Their Significance in Fusion Reactors," *Proc. Fifth Conf. on Plasma Physics and Controlled Nuclear Fusion Research*, IAEA-CN-33, Tokyo (1974), p. 229.
- ²R. BEHRISCH, "Plasma-Wall-Interactions," Lecture at School on Tokamak Reactors for Breakeven, Erice (1976).
- ³D. M. MEADE, "Effect of High-Z Impurities on the Ignition and Lawson Conditions for a Thermonuclear Reactor," *Nucl. Fusion*, 14, 289 (1974).
- ⁴R. W. CONN and J. KESNER, "The Potential of Driven Tokamaks as Thermonuclear Reactors," *Nucl. Fusion*, 15, 775 (1975).
- ⁵W. M. STACEY, JR., ET AL., "Effect of Plasma Confinement and Impurity Level Upon the Performance of a D-T Burning Tokamak Experimental Power Reactor," *Nucl. Fusion* 16, 211 (1976).
- ⁶W. M. STACEY, JR., ET AL., "Impurity Control in Near-Term Tokamak Reactors," *Proc. ANS Top. Mtg. on Technology of Controlled Nuclear Fusion*, USERDA CONF-760935 (1976), p. 315; also, *Proc. Symp. on Plasma-Wall Interaction*, Jülich, Germany (1976).
- ⁷R. V. JENSEN, ET AL., "Critical Impurity Concentrations for Power Multiplication in Beam-Heated Toroidal Fusion Reactors," PPPL-1350, Princeton Plasma Physics Laboratory (1977).
- ⁸L. SPITZER, JR., "The Stellarator Concept," USAEC Rep. No. NYO-993 (PM-S-1) (1951); also, *Phys. Fluids*, 1, 253 (1958).
- ⁹D. M. MEADE, ET AL., "The Effects of Impurities and Magnetic Divertors on High-Temperature Tokamaks," *Proc. Fifth Conf. on Plasma Physics and Controlled Nuclear Fusion Research*, IAEA-CN-33, Tokyo (1974), p. 605.
- ¹⁰M. KEILHACKER, "Magnetic Divertors," Lecture at School on Tokamak Reactors for Breakeven, Erice (1976).
- ¹¹P. E. STOTT, ET AL., "A Review of Work on Plasma-Wall Interactions and Divertor Experiments on DITE," Culham Rep. CLM-P473 (1977).
- ¹²B. LEHNERT, "Screening of a High-Density Plasma from Neutral Gas Penetration," *Nucl. Fusion*, 8, 173 (1968).
- ¹³T. OHKAWA, *Kakuyugo Kenkyu*, 32, 67 (1974).
- ¹⁴W. M. STACEY, JR., ET AL., "Tokamak Experimental Power Reactor Conceptual Design," ANL/CTR/76-3, Argonne National Laboratory (1976).
- ¹⁵R. V. JENSEN, ET AL., "Calculations of Impurity Radiation and Its Effects on Tokamak Experiments," PPPL1334, Princeton Plasma Physics Laboratory (1977).

- 16 W. M. STACEY, JR., ET AL., "EPR-77: A Revised Design for the Tokamak Experimental Power Reactor," ANL/FPP/TM-77, Argonne National Laboratory (1977).
- 17 P. SIGMUND, "Theory of Sputtering. I. Sputtering Yield of Amorphous and Polycrystalline Targets," *Phys. Rev.*, 184, 383 (1969).
- 18 R. WEISMANN and P. SIGMUND, "Sputtering and Backscattering of keV Light Ions Bombarding Random Targets," *Rad. Effects*, 19, 7 (1973).
- 19 S. DANYLUK and P. BRATT, "Studies of CTR First-Wall Erosion by Physical Sputtering," ANL/CTR/TM-60, Argonne National Laboratory (1976).
- 20 H. F. WINTERS, "Physical Sputtering by Light Ions: Theory and Experiment," *Proc. Institute Curriculum Development in Fusion*, Argonne, Ill. (1976).
- 21 M. I. GUSEVA and Y. V. MARTYNYENKO, "Sputtering of Materials by H^+ , D^+ , T^+ , and He^+ Ions," *J. Nucl. Mater.*, 63, 241 (1976).
- 22 D. P. JACKSON, "Binding Energies in Cubic Metal Surfaces," *Rad. Effects*, 18, 1 (1973).
- 23 R. KELLY and N. Q. LAM, "The Sputtering of Oxides. Part I: A Survey of Experimental Results," *Rad. Effects*, 19, 37 (1973).
- 24 R. KELLY, "Sputtering Effects with Nuclear and Thermonuclear Materials," in *Physical Metallurgy of Reactor Fuel Elements* (The Metals Society, London, 1974), p. 275.
- 25 N. BOHR, "The Penetration of Atomic Particles Through Matter," *K. Danske Vidensk. Selsk. Mat.-Fys. Medd.*, 18 (8), 1 (1948).
- 26 G. S. KINCHIN and R. S. PEASE, "The Displacement of Atoms in Solids by Radiation," *Rep. Prog. Phys.*, 18, 1 (1955).
- 27 J. LINDHARD, V. NIELSON and M. SCHARFF, "Approximation Method in Classical Scattering by Screened Coulomb Fields," *K. Danske Vidensk. Selsk. Mat.-Fys. Medd.*, 36 (10), 1 (1968).
- 28 E. HOTSTON, "Threshold Energies for Sputtering," *Nucl. Fusion*, 15, 544 (1975).
- 29 D. ROSENBERG and G. K. WEHNER, "Sputtering Yields for Low Energy He^{+-} , Kr^{+-} , and Xe^{+-} Ion Bombardment," *J. Appl. Phys.*, 33, 1842 (1962).
- 30 C. E. KENKNIGHT and G. K. WEHNER, "Sputtering of Metals by Hydrogen Ions," *J. Appl. Phys.*, 35, 322 (1964).
- 31 J. BONDANSKY, J. ROTH and M. K. SINHA, "Erosion of Different First Wall and Limiter Materials by Low Energy Hydrogen Ions," *Proc. 9th Symp. on Fusion Technology*, Garmish (1976).
- 32 N. LAGREID and G. K. WEHNER, "Sputtering Yields of Metals for Ar^+ and Ne^+ Ions with Energies from 500 to 600 eV," *J. Appl. Phys.*, 32, 365 (1961).

- ³³H. VON SEEFELD, H. SCHMIDL, R. BEHRISCH and B. M. U. SCHERZER, "Sputtering Yields of 1 to 20 keV Light Ions on Stainless Steel," *J. Nucl. Mater.*, 63, 215 (1976).
- ³⁴A. L. SOUTHERN, W. R. WILLIS and M. T. ROBINSON, "Sputtering Experiments with 1- to 5- keV Ar⁺ Ions," *J. Appl. Phys.*, 34, 153 (1963).
- ³⁵H. OECHSNER, Thesis, Univ. Wurzburg, Germany (1963).
- ³⁶R. BEHRISCH, ET AL., "Measurements of the Erosion of Stainless Steel, Carbon, and SiC by Hydrogen Bombardment in the Energy Range of 0.5-7.5 keV," *J. Nucl. Mater.*, 60, 321 (1976).
- ³⁷W. ECKSTEIN, B. M. V. SCHERZER and H. VERBECK, "Sputtering Yields of Niobium by Deuterium in the keV Range," *Rad. Effects*, 18, 135 (1973).
- ³⁸A. J. SUMMERS, N. J. FREEMAN and N. R. DALY, "Sputtering of Niobium by Niobium, Hydrogen, Deuterium, and Helium Ions in the 10- to 80-keV Energy Range," *J. Appl. Phys.*, 42, 4774 (1971).
- ³⁹O. C. YONTS, C. E. NORMAND and D. E. HARRISON, "High Energy Sputtering," *J. Appl. Phys.*, 31, 477 (1960).
- ⁴⁰J. P. BIRSACK, "High-Dose He⁺ Bombardment of Niobium at 800 to 1400°C," *J. Nucl. Mater.*, 63, 253 (1976).
- ⁴¹J. N. SMITH, C. H. MEYER and J. K. LAYTON, "Sputtering Measurements on Controlled Thermonuclear Reactor Materials Using Auger Electron Spectroscopy," *Nucl. Technol.*, 29, 318 (1976).
- ⁴²C. R. FINFELD, "Proton Sputtering," ORO-3557-15, Roanoke College, Salem, Va. (1975).
- ⁴³B. M. SCHERZER, R. BEHRISCH and J. ROTH, "Wall Erosion by Physical and Chemical Sputtering and Blistering," *Proc. Intern. Symp. on Plasma Wall-Interactions*, Jülich, Germany (1976).
- ⁴⁴J. ROTH, ET AL., "Physical and Chemical Sputtering of Graphite and SiC by Hydrogen and Helium in the Energy Range 600 to 7500 eV," *J. Nucl. Mater.*, 63, 222 (1976).
- ⁴⁵D. M. GRUEN, "Chemical Effects of Plasma Interactions with Thermonuclear Reactor Surfaces," in *The Chemistry of Fusion Technology*, D. M. Gruen (Ed.) (Plenum Press, New York, 1972), p. 215.
- ⁴⁶O. K. HARLING, ET AL., "Recent Neutron Sputtering Results and the Status of Neutron-Sputtering," *J. Nucl. Mater.*, 63, 422 (1976).
- ⁴⁷M. KAMINSKY and S. K. DAS, "14.1 MeV Neutron Sputtering of Polycrystalline and Monocrystalline Niobium with Different Surface Microstructures," *J. Nucl. Mater.*, 60, 111 (1976).
- ⁴⁸M. KAMINSKY and S. K. DAS, "Particle Emission from Solids Under 14-MeV Neutron Impact," *J. Nucl. Mater.*, 53, 162 (1974).

- 49 R. G. MEISENHEIMER, "Some 14 MeV Neutron Sputtering Characteristics of a Polycrystalline Nb Sample," *J. Nucl. Mater.*, 63, 429 (1976).
- 50 L. H. JENKINS, ET AL., "Neutron Sputtering Yields from Nb, Au, and Co," *J. Nucl. Mater.*, 63, 438 (1976).
- 51 J. P. BIRSACK, ET AL., "Simulation Experiments for the Sputtering of Niobium by 14 MeV Neutrons," *J. Nucl. Mater.*, 63, 443 (1976).
- 52 R. BEHRISCH, R. GAHLER, and J. KALUS, "Sputtering Yields of Au by 14 MeV Neutrons and Emissions of Recoils from (n,2n) Reactions in Au and Nb," *J. Nucl. Mater.*, 53, 183 (1974).
- 53 M. A. KIRK, ET AL., "Neutron Sputtering of Gold," *J. Nucl. Mater.*, 53, 179 (1974).
- 54 M. T. ROBINSON, "Remarks on the Theory of Fast Neutron Sputtering," *J. Nucl. Mater.*, 53, 201 (1974).
- 55 S. VEPREK, M. R. HAQUE, and H. R. OSWALD, "On the Chemical Erosion of Some Low-Z Materials by Hydrogen Plasma and on the Possibility of Regeneration of the First Wall by Low Pressure Plasma CVD," *J. Nucl. Mater.*, 63, 405 (1976).
- 56 N. P. BUSHAROV, ET AL., "Chemical Sputtering of Graphite by H^+ Ions," *J. Nucl. Mater.*, 63, 230 (1976).
- 57 B. FEINBERG and R. S. POST, "Graphite Surface Erosion and Blistering," *J. Vac. Sci. Techn.*, 13, 443 (1976).
- 58 M. BALOOCH and D. R. OLANDER, "Reactions of Modulated Molecular Beams with Pyrolytic Graphite-III Hydrogen," *J. Chem. Phys.*, 63, 4772 (1975).
- 59 S. K. ERENTS, C. M. BRAGANZA and G. M. McCracken, "Methane Formation During the Interaction of Energetic Protons and Deuterons with Carbon," *J. Nucl. Mater.*, 63, 399 (1976).
- 60 A. R. KRAUSS and D. M. GRUEN, "Determination of Ion Fraction and Energy Analysis of Sputtered Particles from Deuterium Bombarded Surfaces," *J. Nucl. Mater.*, 63, 380 (1976).
- 61 D. M. GRUEN, P. A. FINN and D. L. PAGE, "Vaporization Thermodynamics and Molecular Sputtering of Binary Targets," *Nucl. Techn.*, 29, 309 (1976).
- 62 G. M. McCracken, "Chemical Sputtering of Surfaces by Hydrogen Ions," *Proc. VIII Intern. School on the Physics of Ionized Gases*, August 27, 1976, Dubrovnik, Yugoslavia, p. 409.
- 63 R. B. WRIGHT, R. VARMA and D. M. GRUEN, "Roman Scattering and SEM Studies of Graphite and Silicon Carbide Surfaces Bombarded with Energetic Protons, Deuterons, and Helium," *J. Nucl. Mater.*, 63, 415 (1976).
- 64 C. BRAGANZA, G. M. McCracken and S. K. ERENTS, "Methane Formation During Hydrogen Bombardment of Silicon Carbide," *Proc. Intern. School on Physics of Ionized Gases*, August 27, 1976, Dubrovnik, Yugoslavia.

- ⁶⁵C. BRAGANZA, G. M. McCracken and S. K. ERENTS, "Methane Formation During Hydrogen Ion Irradiations of Silicon and Boron Carbides," to be published.
- ⁶⁶J. N. SMITH, ET AL., "Bombardment of SiC by 10 keV H⁺: Carbon Deposition, Surface Swelling and Changes in Surface Morphology," *J. Nucl. Mater.*, 63, 392 (1976).
- ⁶⁷D. M. GRUEN, "Hydroxyl Formation Accompanying Defect Center Production in Proton and Deuteron Bombarded Aluminum Oxide," *J. Chem. Phys.*, 62, 1192 (1975).
- ⁶⁸G. M. McCracken and J. W. PARTRIDGE, "The Chemical Interaction of Hydrogen Discharges with Nonmetals," *J. Nucl. Mater.*, 63, 373 (1976).
- ⁶⁹D. M. GRUEN, "Chemical Effects of Thermonuclear Plasma Interactions with Insulator and Metal Surfaces," *J. Nucl. Mater.*, 53, 221 (1974).
- ⁷⁰R. WEISMANN and P. SIGMUND, "Sputtering and Backscattering of keV Light Ions Bombarding Random Targets," in *Ion Surface Interaction, Sputtering, and Related Phenomena*, R. Behrisch, Ed. (Gordan and Breach, N. Y., 1973), p. 47.
- ⁷¹P. MEISCHNER and H. VERBEEK, "Energy Distributions of Charged and Neutral Hydrogen Atoms Backscattered from Metal Surfaces Bombarded with 5 to 18 keV Protons," *J. Nucl. Mater.*, 53, 276 (1974).
- ⁷²W. ECKSTEIN, F. E. P. MATSCHKE and H. VERBECK, "Reflection of Hydrogen from Stainless Steel and Nb," *J. Nucl. Mater.*, 63, 199 (1976).
- ⁷³E. W. THOMAS, ET AL., "Scattering of 10-30 keV H⁺, H₂⁺, and H₃⁺ from Surfaces: Excited State Composition and Scattered H⁺ Flux," *J. Nucl. Mater.*, 63, 205 (1976).
- ⁷⁴O. S. OEN and M. T. ROBINSON, "Computer Studies of the Scattering of Low Energy Hydrogen Ions from Polycrystalline Solids," *J. Nucl. Mater.*, 63, 210 (1976).
- ⁷⁵G. CARTER, "Ion Reflection, Penetration and Entrapment in Solids," *J. Vac. Sci. Techn.*, 7, 31 (1970).
- ⁷⁶W. D. WILSON, ET AL., "Particle Re-emission During Irradiation," *J. Nucl. Mater.*, 63, 154 (1976).
- ⁷⁷W. BAUER and G. J. THOMAS, "Helium and Hydrogen Re-emission During Implantation of Molybdenum, Vanadium, and Stainless Steel," *J. Nucl. Mater.*, 53, 127 (1974).
- ⁷⁸K. L. WILSON, G. J. THOMAS and W. BAUER, "Low-Energy Proton Implantation of Stainless Steel," *Nucl. Techn.*, 29, 322 (1976).
- ⁷⁹K. ERENTS and G. M. McCracken, "Trapping and Re-emission of Fast Deuterium Ions from Nickel," *Br. J. Appl. Phys.*, 2, 1397 (1969).

80. D. J. REED, ET AL., "Thermal Evolution Spectrometry of Low Energy Helium Ions Injected Into Stainless Steel and Nickel Targets," *Vacuum*, 24, 179 (1974).
81. M. I. GUSEVA, ET AL., "Radiation Blistering of Nb Implanted Sequentially with Helium Ions of Different Energies (3-500 keV)," *J. Nucl. Mater.*, 63, 245 (1976).
82. J. P. BIRSACK, "High Dose He⁺ Bombardment of Niobium at 800-1400°C," *J. Nucl. Mater.*, 63, 253 (1976).
83. R. G. ST-JACQUES, ET AL., "Dose Rate and Temperature Effects on Blistering Phenomena in Helium Bombarded Niobium," *J. Nucl. Mater.*, 63, 262 (1976).
84. K. L. WILSON and G. J. THOMAS, "Low-Energy Helium Implantation of Aluminum," *J. Nucl. Mater.*, 63, 266 (1976).
85. R. G. ST-JACQUES, ET AL., "Correlation Between Blister Skin Thickness, the Maximum in the Damage-Energy Distribution, and Projected Ranges of Helium Ions in Nb for the Energy Range 10-1500 keV," *J. Nucl. Mater.*, 63, 273 (1976).
86. G. J. THOMAS and W. BAUER, "In-Situ Observations for Ion Implanted Surfaces," *J. Nucl. Mater.*, 63, 280 (1976).
87. J. H. EVANS, "Surface Roughness as a Means of Suppressing Helium Ion Induced Blister Formation in Metals," *J. Nucl. Mater.*, 61, 117 (1976).
88. S. K. DAS and M. KAMINSKY, "Radiation Blistering of Structural Materials for Fusion Devices and Reactors," *J. Nucl. Mater.*, 53, 115 (1976).
89. S. K. DAS, M. KAMINSKY and T. D. ROSSING, "Reduction of Surface Erosion Caused by Helium Blistering: Microstructural Effects," *Appl. Phys. Lett.*, 27, 197 (1975).
90. S. K. DAS and M. KAMINSKY, "Reduction of Surface Erosion Caused by Helium Blistering: Comparison Between Vacuum-Cast and Sintered Beryllium," *Proc. Sixth Symp. Engineering Problems of Fusion Research*, November 18-21, 1975, San Diego, Calif., p. 1151.
91. M. KAMINSKY and S. K. DAS, "Erosion of Silicon Carbide Surfaces Under Helium Ion and 14-MeV Neutron Irradiations," *Proc. First Topical Mtg. on the Technology of Controlled Nuclear Fusion*, April 16-18, 1974, San Diego, Calif., USAEC Rep. CONF-740402 (1974), p. 508.
92. M. KAMINSKY, S. K. DAS and R. EKERN, "Helium Blistering of Ceramic Coatings on Hastelloy X and Nb-1% Zr," *Nucl. Techn.*, 29, 303 (1976).
93. R. EKERN, S. K. DAS and M. KAMINSKY, "Irradiation of Graphite Cloth at Various Temperatures with Deuterons and Helium Ions," *Proc. Sixth Symp. Engineering Problems of Fusion Research*, November 18-21, 1975, San Diego, Calif., p. 1146.

- 94 K. TAKAYANAGI and H. SUZUKI, "Collection of Cross Section Data for Atomic Processes," IPPJ-DT-48, Nagoya, Japan (1975).
- 95 C. F. BARNETT, ET AL., "Atomic Data for Controlled Fusion Research," ORNL-5206 and 5207, Oak Ridge National Laboratory (1977).
- 96 R. L. FREEMAN and E. M. JONES, "Atomic Collision Processes in Plasma Physics Experiments," CLM-R-137, Culham Laboratory (1974).
- 97 W. LOTZ, "Electron-Impact Ionization Cross Sections and Ionization Rates for Atoms and Ions," *Astrophys. J. Suppl.*, 14, 207 (1966-67); also "Electron-Impact Ionization Cross Sections and Ionization Rate Coefficients for Atoms and Ions from Hydrogen to Calcium," *Z. Physik.*, 216, 241 (1968).
- 98 H. J. KUNZE, "Measurements of Collisional Rate Coefficients in Laboratory Plasmas," *Space Science Reviews*, 13, 565 (1972).
- 99 M. F. A. HARRISON, ET AL., "Crossed Beams Measurements of Electron Impact Ionization Cross Sections of Impurity Atoms," *Proc. Conf. on Atomic Processes in High Temperature Plasmas*, February 16-18, 1977, Knoxville, Tennessee, Paper C-6.
- 100 R. E. OLSON, ET AL., "Charge Transfer Cross Sections for B^{+3} , C^{+4} + H Collisions," *Ibid.*, Paper H-11; also, R. E. OLSON and A. SALOP, "Charge Transfer and Impact Ionization Cross Sections for Various A^{+q} + H Systems," *Ibid.*, Paper H-12.
- 101 F. W. MEYER and R. A. PHANEUF, "Charge Transfer Collisions of Multi-charged Carbon, Nitrogen, and Oxygen Ions with Atomic and Molecular Hydrogen," *Ibid.*, Paper H-14.
- 102 G. J. LOCKWOOD, ET AL., "Charge Transfer Measurements for He^{2+} in H and H_2 ," *Ibid.*, Paper H-6.
- 103 H. R. GRIEM, "Atomic Rate Coefficients for Tokamak Plasmas," *Proc. Symp. on Plasma-Wall Interaction*, Jülich, West Germany (1976).
- 104 D. DÜCHS, ET AL., "Radiation Losses from Non-Stationary Plasmas Due to Oxygen Impurities," *Nucl. Fusion*, 14, 73 (1974).
- 105 C. BRETON, ET AL., "Radiation Losses from Oxygen and Iron Impurities in a High Temperature Plasma," *Nucl. Fusion*, 16, 891 (1976).
- 106 E. HINNOV, "Multiple Ionization in High-Temperature Plasmas," MATT-777, Princeton Plasma Physics Laboratory (1970).
- 107 A. L. MERTS, ET AL., "The Calculated Power Output from a Thin Iron-Seeded Plasma," LA-6220-MS, Los Alamos Scientific Laboratory (1976).
- 108 G. R. HOPKINS, "Estimation of Impurity Radiation Losses from Fusion Reactor Plasmas," *Proc. Symp. on Technology of Controlled Thermonuclear Fusion Experiments and the Engineering Aspects of Fusion Reactors*, USAEC Rep. CONF-721111 (1976), p. 795.

- 109 G. R. HOPKINS, "Impurity Radiation Losses from Oxygen in a Plasma," *Trans. Am. Nucl. Soc.*, 23, 46 (1976).
- 110 G. R. HOPKINS and JOHN M. RAWLS, "Impurity Radiation from Medium Density Plasmas," GA-A14241, General Atomic (1976).
- 111 I. GALUSKIN, ET AL., "Radiation Losses in Certain Thermonuclear Systems," *Proc. Plasma Physics and Controlled Nuclear Fusion Research*, June 17-23, 1971, Madison, Wisc., Vol. III, p. 407; also, V. I. KOGAN, "Radiation Losses in Dense High-Temperature Hydrogen Plasma Containing Impurities," *Nucl. Fusion*, 11, 597 (1971).
- 112 J. W. ALLEN and A. K. DUPREE, "Calculations of Ionization Equilibria for Oxygen, Neon, Silicon and Iron," *Astrophys. J.*, 155, 27 (1969).
- 113 M. J. SEATON, *Advances in Atomic and Molecular Physics*, (Academic Press, New York, 1975), Vol. II, p. 83.
- 114 N. H. MAGEE, JR., ET AL., "Electron Impact Excitation of Carbon and Oxygen Ions," LA-6691-MS, Los Alamos Scientific Laboratory (1977).
- 115 *Atomic Data for Fusion*, C. F. BARNETT and W. L. WIESE, Eds. (Controlled Fusion Atomic Data Center of Oak Ridge National Laboratory and the National Bureau of Standards, 1977), Supplement 1.
- 116 M. MATTIOLI, "Bibliographic Review of Ionization, Recombination, and Excitation Coefficients of Impurities Present in a Plasma," EUR-CEA-FC-761 (1975).
- 117 E. D. DONETS and V. I. ILYUSHCHENKO, "Sequential Impact Ionization of Positive Ions of Carbon and Nitrogen ($C^{2+} \rightarrow C^{3+} \rightarrow C^{4+} \rightarrow C^{5+} \rightarrow C^{6+}$, $N^{3+} \rightarrow N^{4+} \rightarrow N^{5+} \rightarrow N^{6+} \rightarrow N^{7+}$)," JINR-P7-8310 (1975).
- 118 J. DAVIS, ET AL., "Distorted Wave Calculations for Gaunt Factors, Cross Sections, and Rate Coefficients of Selected Allowed, Forbidden, and Spin Exchange Transitions," NRL-2939 (1974).
- 119 A. SALOP, "Electron Impact Ionization of Multicharged Ions," *Phys. Rev.*, A14, 2095 (1976).
- 120 P. C. KEPPLER, ET AL., "Electron Impact Excitation Rate Coefficients for Ions of Solar Interest," NRL-3171 (1975).
- 121 H. G. P. LIN DE BARROS and H. S. BRANDI, "Electron Excitation of 2^1S , 2^3S , 2^1P , and 2^3P States of Helium," *Can. J. Phys.*, 53, 2289 (1975).
- 122 A. H. MAHAN, ET AL., "Electron Impact Excitation of the $3S$, $3P$, and $3D$ States of H," *Phys. Rev.*, A13, 156 (1976).
- 123 E. R. SMITH, "Electron Impact Excitation of Atomic Oxygen," *Phys. Rev.*, A13, 65 (1976).

- 124 A. C. ROY and N. C. SIL, "Excitation of $3p(2p)^2$ State of Helium by Electron Impact," *Phys. Rev.*, A14, 68 (1976).
- 125 B. H. BRANSDEN and C. J. NOBLE, "Electron Impact Excitation of Atomic Hydrogen and Hydrogenic Ions," *J. Phys.*, B9, 1507 (1976).
- 126 E. BROOK and M. F. A. HARRISON, *Atomic Data for Fusion*, 2, No. 5, 17 (1976).
- 127 L. P. PRESNYAKOV and A. M. URNOV, "Excitation of Multiple-Charged Ions by Electron Impact," *Sov. Phys.-JETP*, 41, 31 (1976).
- 128 S. M. VALDROVANDI and D. PÉGUIGNOT, "Radiative and Dielectronic Recombination Coefficients for Complex Ions," *Astron. Astrophys.*, 47, 321 (1976).
- 129 W. D. BARFIELD, "Photonization Cross Sections and Radiative Recombination Rate Coefficients for Fe XV-XXV," *Nucl. Fusion*, 15, 1192 (1975).
- 130 A. BURGESS and H. P. SUMMERS, "The Recombination and Level Populations of Ions-I," *Mon. Not. R. Astr. Soc.*, 174, 345 (1976).
- 131 A. JAIN and M. K. SRIVASTAVA, "Atomic Hydrogen Ionization by Electron Impact in the Glaube Approximation," *J. Phys.*, B9, 1103 (1976).
- 132 A. E. KINGSTON, ET AL., "The 1s-2s and 1s-2p Excitation of Atomic Hydrogen by Electron Impact," *J. Phys.*, B9, 605 (1976).
- 133 A. BURGESS and A. S. TWOROWSKI, "Dielectronic Recombination to Form Helium-Like Ions," *Astrophys. J.* 205, L105 (1976).
- 134 A. A. HAASZ, "Effective Cross Sections for Excitation of Atomic Oxygen by Electron Impact," *J. Chem. Phys.*, 65, 1642 (1976).
- 135 C. M. LEE and R. H. PRATT, "Radiative Capture of Electrons by Mo Ions," *Phys. Rev.*, A14, 990 (1976).
- 136 R. J. W. HENRY and J. J. MATESE, "Excitation of He^+ by Electron Impact," *Phys. Rev.*, A14, 1368 (1976).
- 137 T. SCOTT and M. R. C. McDOWELL, "Electron Impact Excitation of the n^{1p} ($n = 2-5$) and 2^3P States of Helium at Intermediate Energies," *J. Phys.*, B9, 2235 (1976).
- 138 D. H. CRANDALL, *Atomic Data for Fusion*, 2, No. 6, 14 (1976).
- 139 J. DAVIS, ET AL., "Electron Impact Excitation Coefficients for Laboratory and Astrophysical Plasmas," *J. Quant. Spectrosc. Radiat. Transfer*, 16, 1043 (1976).
- 140 T. R. DONALDSON, "Dielectronic Recombination in Laser-Generated Plasmas," *CLM-R153* (1976).

¹⁴¹V. L. JACOBS, ET AL., "The Influence of Autoionization Accompanied by Excitation on Dielectronic Recombination and Ionization Equilibrium," *Astrophys. J.*, 211, 605 (1977).

¹⁴²T. P. DONALDSON and N. J. PEACOCK, "Tables for the Computation of Dielectronic Recombination Coefficients," *J. Quant. Spectrosc. Radiat. Transfer*, 16, 599 (1976).



7

